

UNIVERSITY OF THESSALY
SCHOOL OF ENGINEERING
DEPARTMENT OF ELECTRICAL AND COMPUTER ENGINEERING

Advanced Electromigration Analysis Methods for Long - Term Reliability and Hardware Security in Complex VLSI Interconnects

A dissertation submitted in partial fulfillment of the requirements for the degree of Doctor of Philosophy

Pavlos Stoikos

October 2025



UNIVERSITY OF THESSALY
SCHOOL OF ENGINEERING
DEPARTMENT OF ELECTRICAL AND COMPUTER ENGINEERING

Advanced Electromigration Analysis Methods for Long - Term Reliability and Hardware Security in Complex VLSI Interconnects

A dissertation submitted in partial fulfillment of the requirements
for the degree of Doctor of Philosophy

Pavlos Stoikos

October 2025

ΠΑΝΕΠΙΣΤΗΜΙΟ ΘΕΣΣΑΛΙΑΣ
ΠΟΛΥΤΕΧΝΙΚΗ ΣΧΟΛΗ
ΤΜΗΜΑ ΗΛΕΚΤΡΟΛΟΓΩΝ ΜΗΧΑΝΙΚΩΝ ΚΑΙ ΜΗΧΑΝΙΚΩΝ ΥΠΟΛΟΓΙΣΤΩΝ

Προηγμένες Μέθοδοι Ανάλυσης Ηλεκτρομετανάστευσης για Μακροχρόνια Αξιοπιστία και Ασφάλεια Υλικού σε Πολύπλοκες Διασυνδέσεις Ολοκληρωμένων Κυκλωμάτων

Διατριβή η οποία υποβλήθηκε για τη μερική εκπλήρωση
των υποχρεώσεων απόκτησης του Διδακτορικού Διπλώματος

Παύλος Στόικος

Οκτώβριος 2025



UNIVERSITY OF THESSALY
SCHOOL OF ENGINEERING
DEPARTMENT OF ELECTRICAL AND COMPUTER ENGINEERING

Advanced Electromigration Analysis Methods for Long - Term Reliability and Hardware Security in Complex VLSI Interconnects

PhD Dissertation

Pavlos Stoikos

Advisory committee

Nestor Evmorfopoulos, Professor, University of Thessaly (Supervisor)

George Stamoulis, Professor, University of Thessaly

Konstantinos Kolomvatsos, Associate Professor, University of Thessaly

Examination committee

Nestor Evmorfopoulos, Professor, University of Thessaly (Supervisor)

George Stamoulis, Professor, University of Thessaly

Konstantinos Kolomvatsos, Associate Professor, University of Thessaly

Antonis Dadaliaris, Assistant Professor, University of Thessaly

Georgios Panagopoulos, Assistant Professor, National Technical University of Athens

Georgios Karakonstantis, Associate Professor, University of Thessaly

Andreas Tsormpatzoglou, Assistant Professor, University of Ioannina

October 2025

DISCLAIMER ON ACADEMIC ETHICS AND INTELLECTUAL PROPERTY RIGHTS

Being fully aware of the implications of copyright laws, I expressly state that this PH.D. dissertation, as well as the electronic files and source codes developed or modified in the course of this thesis, are solely the product of my personal work and do not infringe any rights of intellectual property, personality and personal data of third parties, do not contain work / contributions of third parties for which the permission of the authors / beneficiaries is required and are not a product of partial or complete plagiarism, while the sources used are limited to the bibliographic references only and meet the rules of scientific citing. The points where I have used ideas, text, files and / or sources of other authors are clearly mentioned in the text with the appropriate citation and the relevant complete reference is included in the bibliographic references section. I also declare that the results of the work have not been used to obtain another degree. I fully, individually and personally undertake all legal and administrative consequences that may arise in the event that it is proven, in the course of time, that this thesis or part of it does not belong to me because it is a product of plagiarism.

The declarant

Pavlos Stoikos

Acknowledgements

As I approach the end of this long and demanding journey, I would like to express my sincere gratitude to all those who have guided, supported, and believed in me. Without their help, I would not have been able to reach this point and complete my Ph.D. studies.

First and foremost, I am deeply grateful to my advisor, Professor Nestor Evmorfopoulos, for his invaluable guidance and for the confidence he placed in me throughout this journey. I am also thankful to the members of my dissertation committee, Professor George Stamoulis and Professor Konstantinos Kolomvatsos, for their constructive feedback and their valuable suggestions that helped shape the direction of my research.

My sincere appreciation goes to my colleagues and friends from the Electronics Research Lab for the countless late nights we spent working long hours, as well as for the laughter and stimulating conversations we shared along the way. In particular, I am deeply grateful to Dr. George Floros and Dr. Dimitrios Garyfalou, who believed in me and gave me the opportunity to embark on this journey. I sincerely thank them for their support and for the excellent collaboration we had throughout my Ph.D. studies.

Last but not least, I would like to express my deepest gratitude to my parents for their endless support, understanding, and sacrifices throughout this journey. I wholeheartedly thank them for always standing by my side and making this achievement possible.



I would like to acknowledge that this research work has been supported by the Hellenic Foundation for Research and Innovation (HFRI) under the 4th Call for HFRI PhD Fellowships (Fellowship number: 11244).

PhD Dissertation

Advanced Electromigration Analysis Methods for Long - Term Reliability and Hardware Security in Complex VLSI Interconnects

Pavlos Stoikos

Abstract

The continuous scaling of integrated circuits (ICs) has introduced significant reliability and security concerns, especially in dense VLSI power grid interconnects. Among these concerns, electromigration (EM) has emerged as a dominant failure mechanism, capable of degrading the performance and lifetime of modern chips. It is a physics-driven effect, where momentum transfer from conducting electrons to metal atoms induces atomic migration along interconnect wires. This process causes gradual material displacement under high current densities, resulting in void or hillock formation that may eventually lead to open or short circuits. As technology nodes shrink and current densities rise, EM analysis becomes increasingly critical to ensuring long-term IC reliability.

In practice, conventional EM assessment methods are primarily empirical and fail to capture the complex spatiotemporal behavior of EM in modern multi-segment interconnect structures. While recent physics-based models offer greater accuracy, most implementations are limited to either the pre-void phase or rely on steady-state assumptions that become invalid under realistic operating conditions. Moreover, emerging hardware threats have revealed that EM behavior can be maliciously manipulated to introduce undetectable hardware Trojans, exposing a security blind spot in traditional reliability methodologies.

To overcome these limitations, this dissertation introduces scalable, physics-based methods for EM analysis, with attention to both reliability and security aspects in VLSI interconnects. It first proposes a complete and scalable EM analysis framework that captures both the pre- and post-void phases by employing matrix exponential formulation combined with Krylov-based techniques. Then, a moment matching (MM) approach using asymmetric Krylov projections is introduced to accelerate EM simulations on large-scale interconnect structures. Finally, the work presents a security-aware EM modeling strategy that intro-

duces design-level countermeasures to safeguard power grids and detects malicious structural changes based on deviations in stress evolution.

Keywords

Electromigration; VLSI reliability; Matrix exponential; Krylov subspace; Korhonen's Equation; Finite Difference Modeling; Interconnect trees; Hardware Security; Time-to-Failure; Hardware Trojans

Διδακτορική Διατριβή

Προηγμένες Μέθοδοι Ανάλυσης Ηλεκτρομετανάστευσης για Μακροχρόνια Αξιοπιστία και Ασφάλεια Υλικού σε Πολύπλοκες Διασυνδέσεις Ολοκληρωμένων Κυκλωμάτων

Παύλος Στόικος

Abstract

Η συνεχής σμίκρυνση των ολοκληρωμένων κυκλωμάτων (integrated circuits – ICs) έχει επιφέρει σημαντικές προκλήσεις ως προς την αξιοπιστία και την ασφάλεια, ιδιαίτερα στα πυκνά διασυνδεδεμένα δίκτυα τροφοδοσίας ισχύος των κυκλωμάτων VLSI. Μεταξύ αυτών των προκλήσεων, η ηλεκτρομετανάστευση (electromigration - EM) έχει αναδειχθεί σε κυρίαρχο μηχανισμό αστοχίας, ικανό να υποβαθμίσει την απόδοση και τη διάρκεια ζωής των σύγχρονων μικροκυκλωμάτων. Πρόκειται για ένα φυσικό φαινόμενο, κατά το οποίο η μεταφορά ορμής από τα ηλεκτρόνια προς τα μεταλλικά άτομα προκαλεί τη σταδιακή μετακίνησή τους κατά μήκος των γραμμών διασύνδεσης. Αυτή η διαδικασία οδηγεί σε βαθμιαία μετατόπιση υλικού υπό συνθήκες υψηλής πυκνότητας ρεύματος, δημιουργώντας κενά (voids) ή περιοχές μεταλλικής συσσώρευσης (hillocks), τα οποία ενδέχεται τελικά να προκαλέσουν διακοπή κυκλώματος ή βραχυκύκλωμα. Καθώς η τεχνολογία προχωρά σε μικρότερους κόμβους και οι πυκνότητες ρεύματος αυξάνονται, η ανάλυση του φαινομένου EM καθίσταται ολοένα και πιο κρίσιμη για τη διασφάλιση της μακροχρόνιας αξιοπιστίας των ICs.

Στην πράξη, οι συμβατικές μέθοδοι εκτίμησης του EM είναι κατά κύριο λόγο εμπειρικές και αδυνατούν να αποτυπώσουν την πολύπλοκη χωροχρονική συμπεριφορά του σε σύγχρονες, πολυτμηματικές γραμμές διασύνδεσης. Αν και πρόσφατα μοντέλα βασισμένα στην φυσική προσφέρουν μεγαλύτερη ακρίβεια, οι περισσότερες υλοποιήσεις περιορίζονται είτε μόνο στη φάση πριν την εμφάνιση κενού (pre-void), είτε βασίζονται σε περιπτώσεις σταθερής κατάστασης, οι οποίες καθίστανται ανεπαρκείς υπό ρεαλιστικές συνθήκες λειτουργίας. Επιπλέον, πρόσφατες απειλές στο υλικού έχουν δείξει ότι η συμπεριφορά του EM μπορεί να παραποιηθεί εσκεμμένα, οδηγώντας σε μη ανιχνεύσιμες επιθέσεις hardware Trojan, αποκαλύπτοντας ένα σημαντικό κενό ασφαλείας στις παραδοσιακές μεθόδους αξιοπιστίας.

Για να αντιμετωπιστούν αυτοί οι περιορισμοί, η παρούσα διατριβή εισάγει επεκτάσιμες μεθόδους βασισμένες σε φυσικά μοντέλα για την ανάλυση του ΕΜ, λαμβάνοντας υπόψη τόσο την αξιοπιστία όσο και τις παραμέτρους ασφάλειας των διασυνδέσεων VLSI. Αρχικά, προτείνεται ένα πλήρες και επεκτάσιμο υπολογιστικό πλαίσιο που καλύπτει τόσο τη φάση πριν όσο και μετά την εμφάνιση κενών, βασισμένο στη χρήση εκθετικής πινάκων (matrix exponential) σε συνδυασμό με τεχνικές Krylov. Στη συνέχεια, αναπτύσσεται μία προσέγγιση τεχνικής ταιριάσματος ροπών (moment matching – MM) με χρήση ασύμμετρων προβολών Krylov, για την επιτάχυνση των προσομοιώσεων του ΕΜ σε διατάξεις διασύνδεσης μεγάλης κλίμακας. Τέλος, παρουσιάζεται μια στρατηγική μοντελοποίησης του ΕΜ με γνώμονα την ασφάλεια, η οποία προτείνει αντιμετωπίσιμα μέτρα σχεδιασμού για την ενίσχυση της προστασίας των δικτύων τροφοδοσίας και εντοπίζει κακόβουλες δομικές μεταβολές βάσει αποκλίσεων στην εξέλιξη της υδροστατικής τάσης.

Λέξεις Κλειδιά

Ηλεκτρομετανάστευση; Αξιοπιστία Ολοκληρωμένων Κυκλωμάτων; Εκθετικό Πίνακα; Υπόχωρος Krylov; Εξίσωση Korhonen; Μοντέλο Πεπερασμένων Διαφορών; Αγωγοί Διασυνδέσεων; Ασφάλεια Υλικού; Χρόνος Αστοχίας; Κακόβουλα κυκλώματα

Contents

Abstract **xiii**

Abstract in Greek **xv**

Contents **xvii**

List of Figures **xxi**

List of Tables **xxv**

Abbreviations **xxvii**

1 Introduction **1**

1.1 Motivation 1

1.2 Thesis contribution 4

1.3 Thesis organization 5

2 Background **7**

2.1 Electromigration basics 7

2.2 Korhonen's model 8

2.3 Post-void stress mechanics 9

3 Pre- and post-void EM analysis based on matrix exponential **11**

3.1 Introduction 11

3.2 Problem formulation 14

3.3 Handling void formation 16

3.4 Proposed EM stress analysis 17

3.4.1 Analytical solution 17

3.4.2 Singularity elimination for the LTI system . . . 18
3.4.3 Krylov subspace-based EM stress analysis . . . 19
3.4.4 Rational Krylov subspace for the matrix exponential . . . 22
3.4.5 Nucleation time estimation . . . 25
3.5 Experimental results . . . 26
3.5.1 Results on an eight-segment tree . . . 29
3.5.2 Scalability analysis . . . 33
3.5.3 Analysis on OpenROAD power grid designs . . . 35
3.5.4 Evaluation of the RKS-based method . . . 39
3.6 Summary . . . 41

4 EM analysis via asymmetric Krylov-based model reduction 43
4.1 Introduction . . . 43
4.2 Background of MOR by MM . . . 45
4.3 Specification of EKS and its application to MM . . . 47
4.4 Proposed asymmetric Krylov-based method . . . 48
4.5 Efficient computation of the reduced-order response and transfer function . 51
4.6 Experimental results . . . 52
4.6.1 Accuracy and performance evaluation of ROMs . . . 53
4.6.2 EM stress evaluation on a seven-segment tree . . . 57
4.6.3 Transient EM analysis on IBM power grid benchmarks . . . 58
4.7 Summary . . . 61

5 Security closure approach for EM-based attacks 63
5.1 Introduction . . . 63
5.2 Review of EM-based trojan attacks . . . 65
5.2.1 Reservoir removal in interconnect lines . . . 66
5.2.2 Sink insertion in interconnect trees . . . 67
5.3 Proposed security closure framework . . . 68
5.3.1 Methodology for reservoir-based attack mitigation . . . 68
5.3.2 Methodology for sink-based attack mitigation . . . 71
5.4 Experimental results . . . 73
5.4.1 Evaluation on IBM power grid lines . . . 74

5.4.2 Evaluation on OpenROAD interconnect trees 76
5.5 Summary 79

6 Conclusions and future directions **81**
6.1 Conclusions 81
6.2 Future directions 82

Publications **85**

Bibliography **87**

APPENDICES **95**

A Matrix exponential solution **97**

List of Figures

1.1 Representative EM-induced microstructural failures in metal interconnects. 2

2.1 Cross section of a Cu wire indicating the two forces [1]. 8

2.2 An m-segment interconnect tree. 8

3.1 Each discretized point may be located at (a) the left boundary segment, (b) the middle of a segment, (c) an intermediate junction, (d) a via junction, and (e) the right boundary segment.The red box around each discretized point represents the corresponding area of Eq. (3.4). 16

3.2 Tree splitting at a via junction due to void nucleation, resulting in independent subtrees for post-void analysis. 17

3.3 Tolerance selection for optimal trade-off 28

3.4 (a): Comparison of EM stress at $\boldsymbol{t = 20}$ years, with stress values at each node presented as tuples, where the proposed solution is shown in black and the COMSOL solution in blue text. (b): The relative error between our proposed solution and the COMSOL solution at $\boldsymbol{t = 20}$ years. 30

3.4 (c): Nucleation phase validation on the horizontal segments of the tree at $\boldsymbol{t = 5}$, $\boldsymbol{t = 10}$, and $\boldsymbol{t = 20}$ years. 31

3.5 (a): Comparison of the post-void stress at $\boldsymbol{t = 0.7}$ years, with stress values at each node presented as tuples, where the proposed solution is shown in black and the COMSOL solution in blue text.(b): The relative error between our proposed solution and the COMSOL solution at $\boldsymbol{t = 0.7}$ years. (c) Growth phase validation on the horizontal segments of the right subtree at $\boldsymbol{t = 0.1}$, $\boldsymbol{t = 0.4}$, and $\boldsymbol{t = 0.7}$ years. 32

3.6 An interconnect with $\mathbf{n}$ successive $\mathbf{T}$ juntions. 33

3.7 Speedup comparison of the proposed method over COMSOL, Higham [2], and Expokit [3] across different numbers of T-junctions. 34

3.8 (a) Selected region of the 12 nm aes design with a cutline crossing all segments. (b) Comparison of stress profiles along the cutline during the nucleation phase, for $t = 0.8$, 6.5, and 8.6 years. 37

3.9 (a) Selected region of the 12 nm aes design after tree splitting at the void location, showing both resulting subtrees. (b) Comparison of stress profiles along the cutline during the growth phase at $t = 0.4$, 1.5, and 1.7 years. . . 39

3.10 Accuracy of our RKS-based method in computing the EM stress at t = 20 years for a multi-segment tree of a 28 nm aes design. 41

4.1 Visual representation of (a) the EKS sequence, (b) the AEKS sequence. Blue and purple blocks correspond to powers of matrices $\mathbf{A}_E$ and $\mathbf{A}_E^{-1}$, respectively. 49

4.2 Modulo m parameter selection for optimal trade-off across four industrial benchmarks with varying sparsity ratios γ. 53

4.3 Comparison of transfer functions of ROMs obtained by EKS-MM, AEKS-MM, and MM in the frequency range $[10^0, 10^{12}]$ for ibmpg1 and ibmpg4 benchmarks at ports (5,5) and (10,10), respectively. 55

4.4 Comparison of transfer functions and absolute error magnitudes of ROMs obtained by EKS-MM, AEKS-MM, and MM in the frequency range $[10^0, 10^{12}]$ for ibmpg7 at port (15,15). 56

4.5 (a)-(c): Comparison of EM stress at $\boldsymbol{t = 5}$, $\boldsymbol{t = 10}$, and $\boldsymbol{t = 20}$ years, respectively. The stress at each node is shown as a tuple, with our AEKS-MM solution in black and the COMSOL solution in blue text. (d): The relative error between our proposed solution and the COMSOL solution at $\boldsymbol{t = 20}$ years. 57

4.6 Stress profile comparison along the first 27 segments of the selected line from ibmpg1 benchmark at $t = 20$ years. 60

4.7 Transient EM stress response at the left boundary node under a periodic current density input, comparing AEKS-MM and COMSOL results over a 20-year simulation. 60

5.1 Overview of the IC design and fabrication process, showing potential attack and detection points. 66
5.2 EM-based Trojan for reservoir removal attacks. 67
5.3 EM-based Trojan for sink insertion attacks. 67
5.4 EM stress build-up at t = 20 years a 57-segment line from the ibmpg6 benchmark. 75
5.5 Transient simulation of the attack point for a 57-segment line from the ibmpg6 benchmark. 76
5.6 EM stress build-up at t = 20 years across an artificial 22-segment tree. . . . 78
5.7 Transient simulation of the attack point from an artificial 22-segment tree. . 78

List of Tables

3.1 Cu DD interconnect characteristics for EM analysis 27

3.2 Runtime comparison of the proposed method and COMSOL for increasing number of T junctions 34

3.3 Runtime and accuracy comparison between the proposed method and COMSOL, as well as Newton-Raphson convergence results, are presented for large-scale OpenROAD power grids during the nucleation phase. 36

3.4 Runtime and accuracy comparison of the proposed method against COMSOL and Higham [2] on large-scale OpenROAD power grids during the growth phase. 38

3.5 Runtime and accuracy comparison of the proposed EKS- and RKS-based methods against COMSOL on large-scale OpenROAD power grids. 40

4.1 Results of EKS-MM and AEKS-MM vs MM for industrial IBM power grids 54

4.2 Results between the AEKS-MM method and COMSOL for large-scale IBM power grids 59

5.1 Experimental results of our security closure methodology for large-scale IBMPG benchmarks 75

5.2 Experimental results of our security closure approach on the large-scale OpenROAD interconnect trees 77

Abbreviations

AI	Artificial Intelligence
BC	Boundary Condition
BE	Backward Euler
CuDD	Copper Dual-Damascene
EKS	Extended Krylov Subspace
EM	Electromigration
FDM	Finite Difference Method
FEM	Finite Element Method
GNN	Graph Neural Network
HTs	Hardware Trojans
ICs	Integrated Circuits
LTI	Linear Time-invariant
ML	Machine Learning
MM	Moment Matching
MOR	Model Order Reduction
ODE	Ordinary Differential Equation
PDE	Partial Differential Equation
PINN	Physics-Informed Neural Network
RKS	Rational Krylov Subspace
ROM	Reduced Order Model
TTF	Time-to-Failure

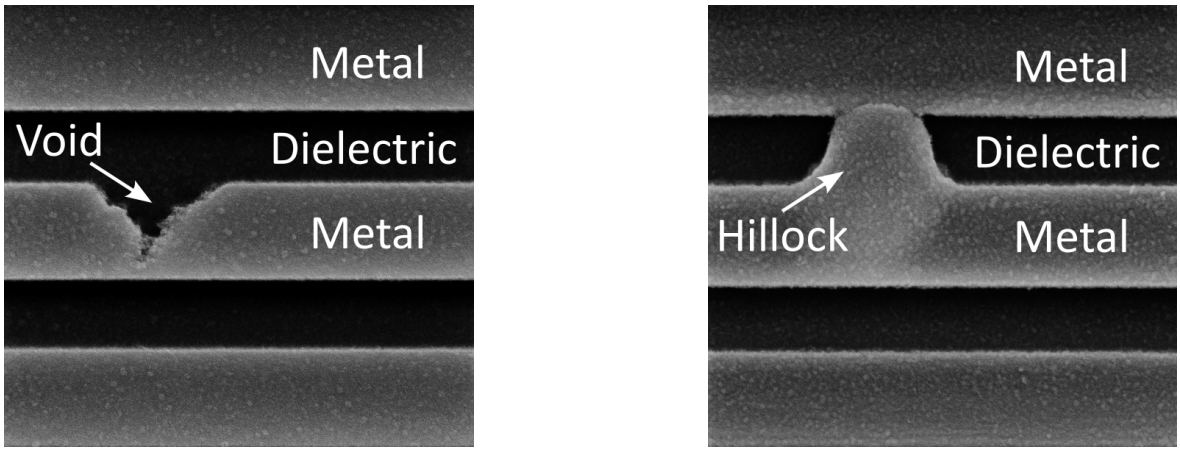
Chapter 1

Introduction

1.1 Motivation

The continued scaling of integrated circuits (ICs) has brought tremendous performance benefits, yet it has also introduced significant reliability and security challenges. These challenges become even more pronounced as CMOS scaling progresses beyond the 10nm node, where increased integration density and new device architectures such as FinFETs push interconnect reliability to its limits. This trend, in turn, intensifies long-term reliability concerns, particularly in power delivery networks and interconnects, where electromigration (EM) emerges as a key failure mechanism. Recognized as one of the most critical degradation phenomena, EM causes gradual material displacement under high current densities, compromising the structural integrity of metal wires over time. This migration process can lead to the formation of voids and hillocks, as illustrated in Fig. 1.1, potentially resulting in open- or short-circuit failures in on-chip interconnects [4]. As a result, EM has become a dominant reliability limiter in today's nanoscale interconnects, and has been established as an integral part of modern VLSI design flows [5].

In the past, several empirical methods for EM analysis have been developed, such as the application of the Blech criterion [6] followed by the Black's equation [7]. However, besides the heuristic nature of these approaches, they suffer from fundamental limitations that lead to overdesign, increased power consumption, and inefficient area utilization, particularly in advanced technology nodes [8]. The Blech criterion evaluates whether a wire is "immortal" by computing the product of current density j and wire length l, and comparing it to a technology-specific threshold. If product $j \times l$ is below this threshold, the wire is consid-



(a) Void formation due to atomic depletion under sustained current stress.

(b) Hillock formation caused by localized atomic accumulation.

Figure 1.1: Representative EM-induced microstructural failures in metal interconnects.

ered "immortal" to EM-induced failure. However, this method only applies to single-segment wires, and fails to capture the complex behavior of multi-segment or mesh-based interconnects, which are common in modern power grids. On the other hand, Black's equation estimates the time-to-failure (TTF) through empirical curve fitting based on temperature and current density. Although useful for early-stage reliability projections, it assumes uniform geometry and constant stress conditions, making it unsuitable for realistic circuits. Specifically, it often results in inaccurate EM lifetime estimates under real operating conditions [9], and does not account for material flow between interconnected branches, which plays a crucial role in stress redistribution within dense interconnect networks [10].

In contrast to previous empirical approaches, Korhonen et al. [11] proposed a physics-based model for EM, formulated as a diffusion-like partial differential equation (PDE). This model accurately captures the fundamental EM mechanism by coupling atomic flux with the gradient of hydrostatic stress across interconnect segments. Building upon this foundation, various methods have been developed to compute the evolution of EM-induced stress in single-segment wires, and were later extended to support multi-segment interconnects [12]. However, applying these techniques to complex interconnect topologies, such as power grid trees, requires efficient and scalable computational strategies. Some existing approaches [13, 14, 15] attempt to characterize wire segments as "mortal" or "immortal" based on their steady-state stress profiles. While such simplifications can reduce computational cost, they inherently overlook the dynamic nature of the EM process. In fact, the time required to reach

steady-state stress often surpasses the expected lifetime of the IC, making such assumptions not only inaccurate but also fundamentally unsuitable for capturing the dynamic behavior of EM in real-world VLSI designs.

In response to these challenges, several models have been developed that perform time-dependent (transient) analysis, aiming for more accurate and efficient characterization of EM behavior over time. These models provide deeper insight into the underlying physics of EM by capturing both the spatial and temporal evolution of stress. In general, these approaches can be categorized as analytical, numerical, or semi-analytical. Analytical models offer closed-form solutions with low computational cost but are often constrained by oversimplified assumptions and limited applicability to realistic interconnect structures. Numerical methods, on the other hand, provide greater modeling flexibility and accuracy but tend to be computationally intensive. To address these trade-offs, semi-analytical techniques have been developed to combine the strengths of both, achieving a balance between precision and efficiency. Despite these advancements, most existing methodologies focus primarily on the nucleation phase of EM-induced failure, without addressing the growth phase, which is critical for a complete and accurate characterization of EM vulnerability in interconnect structures.

Adding to the complexity of EM modeling is the growing intersection between reliability and hardware security. Recent research has revealed that EM stress evolution can be intentionally influenced to induce premature failure, introducing a class of EM-based Trojans. Such attacks may be realized by stealthily modifying interconnect structures to accelerate localized stress accumulation and void formation. These malicious modifications are particularly insidious as they exploit the physical properties of the EM process itself and remain undetectable to conventional EM analysis during chip design. As a result, they expose a critical vulnerability in current reliability-security design methodologies, demanding new analysis frameworks that integrate both physical stress modeling and security threat detection.

This dissertation is driven by the need to introduce EM analysis methodologies that combine physical accuracy with computational efficiency, enabling a deeper understanding of stress evolution over time. While the limitations of recent EM assessment approaches have been analyzed in detail earlier, this work builds upon that foundation to propose a more complete modeling framework that also considers emerging hardware-level threats exploiting EM behavior. By addressing both reliability challenges and security concerns, this dissertation contributes to the development of robust and trustworthy ICs for advanced technologies.

1.2 Thesis contribution

In order to address the limitations of existing EM assessment techniques, this dissertation introduces a set of advanced methodologies that enable accurate, scalable, and security-aware EM stress analysis for complex VLSI interconnects. The main contributions of this dissertation are summarized as follows:

- A complete and scalable EM analysis framework covering both pre- and post-void phases. This work introduces a time-continuous EM stress analysis methodology that captures the full degradation process, including both pre-void stress evolution and post-void topological changes. The framework is based on a semi-analytical formulation of Korhonen's physics-based model and leverages the matrix exponential solution of the EM system. To enable scalability for large VLSI power grids, the approach integrates Krylov subspace techniques, allowing efficient and accurate computation of stress in large-scale industrial designs under realistic operating conditions.

- A reduced-order modeling approach for EM stress evaluation using asymmetric Krylov projections. To enhance the scalability of transient EM analysis, an efficient model order reduction (MOR) technique was developed based on asymmetric projections within the extended Krylov subspace (EKS). By exploiting the sparsity and structural properties of the EM system, the proposed method produces compact models that maintain high accuracy, while significantly reducing the computational cost of transient simulations in large-scale power grids.

- A security-aware EM modeling and mitigation strategy. The dissertation investigates the use of EM as a potential hardware Trojan vector and proposes a security closure framework. This method detects malicious structural modifications, such as reservoir removals and the insertion of current sinks, by analyzing the stress signatures of EM. In addition to detection, the method introduces targeted design-level countermeasures that enhance the reliability and security of power grid interconnects against EM-induced failures and stealthy hardware-level manipulation.

1.3 Thesis organization

The next chapters of this dissertation are organized as follows. Firstly, Chapter 2 provides the necessary background on EM, including the fundamental physics and mathematical formulations, with emphasis on Korhonen's equation. Then, Chapter 3 introduces a scalable transient EM framework that captures both pre- and post-void phases using the matrix exponential formulation combined with Krylov-based techniques. Chapter 4 describes a reduced-order modeling technique based on asymmetric Krylov projections. Chapter 5 explores EM as a hardware security threat and proposes a detection and mitigation framework based on deviations in stress behavior. Finally, Chapter 6 concludes the dissertation and outlines future directions.

Chapter 2

Background

2.1 Electromigration basics

As shown in Fig. 2.1, which is the cross section of a Cu Dual Damascene (DD) wire, the movement of metal atoms is mainly determined by the resultant of two opposing forces. The first one, the $F_{\text{electron-wind}}$ is generated by the momentum transfer between electrons and metal atoms, and is the primary cause of EM. The second force, known as $F_{\text{back-stress}}$, results from the uneven concentration of atoms that gives rise to a diffusion-type force opposite to the electron flow. As EM progresses, the interaction between these two forces drives the movement of metal atoms in the direction of the current flow, from the cathode (–) to the anode (+). Over time, the disparity in the concentration of metal atoms between the anode and the cathode creates a compressive stress in the former and a tensile stress in the latter. This causes a hillock formation near the anode and a void formation at the cathode, leading to open circuits and the end of the wire's lifetime.

It is well known that the movement of metal atoms in a Cu DD interconnect technology is limited to one layer due to the diffusion barriers, preventing the mass transport to adjacent layers [16]. Consequently, EM analysis of a large interconnect structure, such as a power grid, can be performed layer by layer. More specifically, each layer has a generic orthogonal mesh structure that can be divided into a group of multi-segment interconnect trees [17]. Based on this, an analysis of every multi-segment interconnect tree is carried out, which is the main focus of this chapter. Generally, in a multi-segment structure, a set of wire segments and vias are interconnected with junctions, where each wire segment carries a certain current density. Fig. 2.2 depicts an example of a multi-segment interconnect tree.

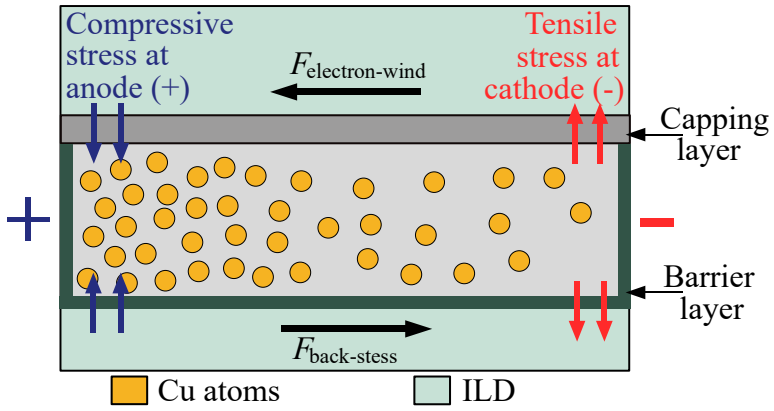


Figure 2.1: Cross section of a Cu wire indicating the two forces [1].

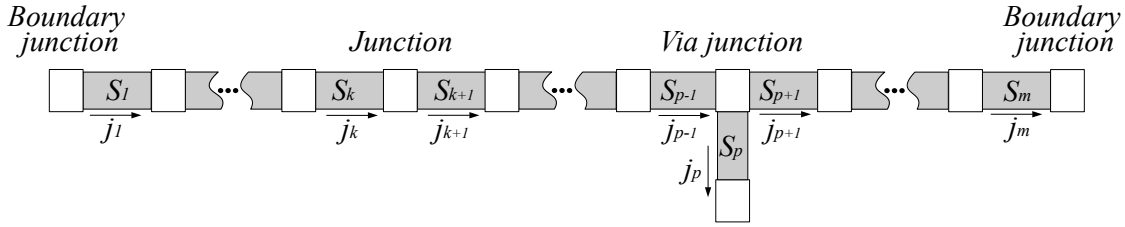


Figure 2.2: An m-segment interconnect tree.

2.2 Korhonen's model

According to the EM analysis of a multi-segment interconnect tree, the stress evolution $\sigma(x,t)$ of each segment can be described by the diffusion Korhonen's PDE [11], which relates the stress σ to the distance from the cathode x. Their relation is expressed as:

$$\frac{\partial \sigma}{\partial t} = \frac{\partial}{\partial x}\left[\kappa\left(\frac{\partial \sigma}{\partial x} + \beta j\right)\right] \tag{2.1}$$

, where $\beta = (Z^* e\rho)/\Omega$ is the EM driving force and $\kappa = D_a \mathcal{B}\Omega/(k_B T)$ is the diffusivity of stress with $D_a = D_0 e^{-E_a/k_B T}$ being the diffusion coefficient. Here, E_a is the activation energy, D_0 is the diffusivity constant, j is the current density through the segment of the wire, Z^* is the effective charge number, e is the electron charge, ρ is the resistivity, Ω is the atomic volume for the metal, $\mathcal{B}$ is the bulk modulus of the material, k_B is Boltzmann's constant, T is the temperature, x is the coordinate along the wire, and t is time. In addition, the stress gradient $\partial\sigma/\partial x$ accounts the flux related to $F_{\text{back-stress}}$, the term βj represents atomic flux attributable to $F_{\text{electron-wind}}$, while the sum of these two $\left(\partial\sigma/\partial x + \beta j\right)$ is related to the net atomic flux.

The described Eq. (2.1) is supplemented by a set of boundary conditions that relate the

stress at any point x_i, along with a temporal boundary condition that initializes the stress values at $t = 0$ [18]. For an intermediate point x_i of the structure with degree d_i, the set of incident segments is denoted as $S_i = \{s_1, s_2, \ldots, s_{d_i}\}$. Therefore, the spatial boundary conditions are as follows:

$(\mathbf{1})$ **Continuity constraints**: At any intermediate point x_i of the multi-segment tree, the stress must be continuous:

$$\sigma_{s_k}(x = x_i, t) = \sigma_{s_{k+1}}(x = x_i, t), \quad k = 1, \ldots, d_i - 1 \tag{2.2}$$

$(\mathbf{2})$ **Flux constraints**: The total atomic flux entering each point x_i must be equal to zero:

$$\sum_{s_k \in S_i} w_{s_k} \kappa_{s_k} \left(\frac{\partial \sigma_{s_k}}{\partial x}\bigg|_{x=x_i} + \beta j_{s_k} \right) = 0 \tag{2.3}$$

, where κ_{s_k} is the diffusivity of segment s_k, j_{s_k} is the current density of segment s_k, which is positive when directed away from x_i and negative when directed into x_i, and w_{s_k} is the segment width. A special case is that the boundary conditions at any end-point (i.e., point with degree 1) require zero flux across the blocking boundary, i.e.,

$$\frac{\partial \sigma_{s_k}}{\partial x}\bigg|_{x=x_i} + \beta j_{s_k} = 0 \tag{2.4}$$

, where j_{s_k} is the current density of segment s_k that is incident on end-point x_i.

2.3 Post-void stress mechanics

Once a void is formed, it typically appears near terminal nodes or vias, where the local mechanical stress drops close to zero. This is mainly caused by the accumulation of vacancies generated by EM, especially near the cathode. If the local vacancy concentration exceeds a critical threshold σ_{crit}, vacancy supersaturation occurs, leading to the coalescence of vacancies and ultimately to void nucleation. At that point, a large stress gradient is generated between the void and the adjacent material, since the surrounding area retains stress levels similar to those before void nucleation. The distance over the stress gradient is defined as effective thickness of the void interface δ [19], which is typically very small compared to the total interconnect length. As a result, the boundary condition at nucleation point x_{nuc} on segment s_k can be described as follows:

$$\frac{\partial \sigma_{s_k}}{\partial x}\bigg|_{x=x_{\text{nuc}}} = \frac{\sigma_{s_k}(x_{\text{nuc}}, t)}{\delta}, \quad \text{for } t_{\text{nuc}} < t < \infty \tag{2.5}$$

with $\sigma_{s_k}(\delta, t) \approx \sigma_{s_k}(x_{\text{nuc}}, t)$, since δ is very small. During this phase, the boundary conditions Eq. (2.2), (2.3), and (2.4) continue to hold with the initial stress distribution inherited from the end of the nucleation phase.

Physically, the stress gradient across the void induces a back-stress force $F_{\text{back-stress}}$ that drives atoms to diffuse from regions of high mechanical stress to those of lower stress. This phenomenon is known as stress migration (SM), and it generally acts as a balancing mechanism to counter the effects of EM by redistributing material. However, since a void has already nucleated, the action of SM may worsen the situation by driving more atoms away from the void, accelerating material degradation and increasing the risk of an open-circuit failure.

Chapter 3

Pre- and post-void EM analysis based on matrix exponential

3.1 Introduction

Given the challenges associated with traditional EM models discussed in Chapter 1, efforts have been made to develop more robust modeling techniques. In this context, Korhonen et al. [11] implemented an exact physics-based model as PDEs. Building on this work, several methodologies have been developed for computing the EM stress in segment lines. More specifically, these methods can be divided into three main categories. First, numerical methods, such as [20, 21], are well-established due to their simplicity and have already been integrated into commercial tools such as COMSOL [22]. These methods perform discretization of space and time, and are in principle applicable to a wide spectrum of geometries due to the spatial discretization. However, they do not scale well and are computationally prohibitive for large-scale interconnects.

As a result, the emphasis has been placed to analytical methods for the solutions of Korhonen's equations, which keep both space and time continuous, and can be effectively applied to large-scale systems. Previous analytical approaches [23] calculate infinite series solutions and can be applied in general multi-segment interconnects. Moreover, in [1], the concept of stress reflections was introduced, which can also be applied to general multi-segment lines of arbitrary number of segments. However, the majority of these methods involve approximation of infinite series with a finite number of terms, which can become expensive since the number is dependent on both line length and time and cannot be known beforehand.

Semi-analytical methods bridge the gap between fully analytical and numerical approaches, enabling faster solutions without significant loss of accuracy, even for complex interconnect topologies. One such method is proposed in [24], which relies on the discrete cosine transform (DCT) to model the stress evolution in multi-segment lines. However, applying the DCT to large-scale systems can require substantial memory resources, as it involves computing all eigenvalues of the system. Another method is presented in [25], but it requires finite-term approximation of infinite series and accurate computation of eigenvalues to enforce continuity of stress and mass flux at junctions. These steps can be particularly computationally intensive, especially for complex interconnect geometries.

Beyond physics-based methods, recent advances in machine learning have introduced deep learning techniques for fast and scalable EM prediction. For instance, graph neural network (GNN)-based methods [26], [27] leverage structural and physical features of interconnect networks to efficiently predict EM stress in multi-segment interconnects. Additionally, [28] introduces a hierarchical physics-informed neural network (PINN) framework, aiming to provide both accurate and efficient EM analysis across multi-segment interconnect structures. Although offering scalability, their accuracy depends on the quality and diversity of the training data, limiting generalization to unseen or complex multi-segment interconnects.

While most existing methods focus on pre-void analysis, accurately modeling the growth phase is equally important for assessing long-term interconnect reliability. This phase remains less explored due to the structural discontinuities it introduces. An analytical method in [19] addresses this phase but is limited to simple interconnect lines. In the same work, a finite-element approach [29] has been proposed, which becomes computationally expensive due to the complex meshing required for large-scale interconnects. Additionally, a PINN-based method [30] has been introduced, yet its performance is highly dependent on diverse and comprehensive training datasets.

In this chapter, we present a fast semi-analytical approach for solving Korhonen's equation across both the pre-void and post-void phases in general interconnect trees. The main contributions of this work are summarized as follows:

- Our method accurately computes EM stress at any input time during both the void nucleation and void growth phases by directly evaluating the matrix exponential solution. Unlike traditional numerical methods, our approach discretizes only the spatial domain, enabling

time-continuous evaluation without iterative time stepping.

- We propose an optimized application of the extended Krylov subspace (EKS) method to efficiently approximate the matrix exponential, which can significantly reduce the complexity of the proposed methodology. Exploiting the assumption that each interconnect segment maintains a constant current density [18], the EKS construction becomes a one-time cost.

- As an alternative to EKS, we propose a parameter-free approach based on the rational Krylov subspace (RKS), which adaptively computes a set of optimal shifts by capturing the important eigenvalues of the system. This approach enables accurate and compact matrix exponential approximations without requiring manual selection of shift parameters.

- We develop a Newton-Raphson algorithm to estimate the void nucleation time and location, directly leveraging the EKS representation for fast and accurate convergence.

- We incorporate a tree-splitting mechanism that models the post-void phase by dynamically restructuring the interconnect tree into multiple subtrees, allowing for independent analysis after void formation.

Finally, the proposed method has been extensively validated on large-scale OpenROAD benchmarks and several artificial interconnect structures, demonstrating great speedups over COMSOL with near-perfect agreement. Moreover, it achieves a 27× average speedup over the state-of-the-art exponential method Higham [2], with only minor accuracy degradation, while it outperforms other exponential solver Expokit [3] by achieving a 5× faster runtime.

The rest of this chapter is organized as follows. Section 2.1 provides basic background on EM analysis of interconnect trees. Section 3.2 demonstrates the problem formulation of EM analysis. Section 3.3 addresses the modeling of void formation and the corresponding tree restructuring for post-void analysis. Then, Section 3.4 details our main contributions, including the matrix exponential formulation, singularity elimination, the application of the EKS and RKS methods, and the void nucleation estimation algorithm. Section 3.5 demonstrates an extensive experimental evaluation of our method on available OpenROAD benchmarks and several artificial interconnect trees, followed by the conclusions in Section 3.6.

3.2 Problem formulation

In EM analysis, each segment of the interconnect tree is considered to carry a constant current density j [18]. As a result, the Korhonen's Eq. (2.1) for each segment takes the following form:

$$\frac{\partial \sigma}{\partial t} = \kappa \frac{\partial^2 \sigma}{\partial x^2} \tag{3.1}$$

This equation can be uniformly discretized by dividing each segment of the interconnect tree into points of equal length Δx, using the Finite Difference Method (FDM). By applying a finite difference approximation of the spatial derivative in Eq. (3.1), for each discretized point i of the interconnect tree, we get:

$$\frac{d\sigma_i}{dt} = \kappa \frac{(\frac{\sigma_{i+1}-\sigma_i}{\Delta x}) - (\frac{\sigma_i-\sigma_{i-1}}{\Delta x})}{\Delta x} \tag{3.2}$$

i.e.,

$$(w \cdot \Delta x)\frac{d\sigma_i}{dt} = \kappa \left(\frac{\sigma_{i+1} - \sigma_i}{\Delta x / w} \right) - \kappa \left(\frac{\sigma_i - \sigma_{i-1}}{\Delta x / w} \right) \tag{3.3}$$

, where w is the width of the wire segment that point i belongs to and $a_i = w \cdot \Delta x$ is the total area of the segments connected to the point i (see Fig. 3.1). The formula of a_i is described as:

$$a_i = \frac{1}{2} \sum_{s_k \in S_i} w_{s_k} \cdot \Delta x \tag{3.4}$$

For simplicity of visualization and discretization, we assume the thickness to be negligible compared to the other two dimensions, effectively treating the interconnect structure as two-dimensional. However, the same methodology remains applicable in three-dimensional settings by incorporating the thickness into the local volume term.

After applying FDM on the m-segment interconnect tree of Fig.2.2, the resulting n discretized points may be located at five different locations, as shown in Fig. 3.1. Considering the boundary conditions of Eq. (2.2), (2.3), and (2.4), we can rewrite Eq. (3.3) for the n discretized points into the Ordinary Differential Equation (ODE) system of Eq. (3.5). More specifically, Eq. (3.5) depicts the stamps of the two boundary points x_1 and x_n, any point x_i at the middle of a segment, any intermediate junction point x_i, and any via junction point x_j, with $1 < i < j < n$. As a result, we can write the ODE system for EM stress evolution as the following Linear time-invariant (LTI) system:

$$\mathbf{C}\dot{\sigma}(t) = \mathbf{G}\sigma(t) + \mathbf{B}\mathbf{j}(t) \tag{3.6}$$

$$
\begin{bmatrix}
a_1 & \cdots & 0 & \cdots & 0 & \cdots & 0 \\
\vdots & \ddots & \vdots & \ddots & \vdots & \ddots & \vdots \\
0 & \cdots & a_i & \cdots & 0 & \cdots & 0 \\
\vdots & \ddots & \vdots & \ddots & \vdots & \ddots & \vdots \\
0 & \cdots & 0 & \cdots & a_j & \cdots & 0 \\
\vdots & \ddots & \vdots & \ddots & \vdots & \ddots & \vdots \\
0 & \cdots & 0 & \cdots & 0 & \cdots & a_n
\end{bmatrix}
\begin{bmatrix}
\dot{\sigma_1} \\ \vdots \\ \dot{\sigma_i} \\ \vdots \\ \dot{\sigma_j} \\ \vdots \\ \dot{\sigma_n}
\end{bmatrix} =
$$

$$
\frac{\kappa}{(\Delta x)}
\begin{bmatrix}
-w_{s_1} & w_{s_1} & 0 & \cdots & \cdots & \cdots & \cdots & 0 \\
\vdots & \ddots & \ddots & \ddots & \ddots & \ddots & \ddots & \vdots \\
0 & \cdots & w_{s_k} & -(w_{s_k} + w_{s_{k+1}}) & w_{s_{k+1}} & \cdots & \cdots & 0 \\
\vdots & \ddots & \ddots & \ddots & \ddots & \ddots & \ddots & \vdots \\
0 & \cdots & w_{s_{p-1}} & -(w_{s_{p-1}} + w_{s_p} + w_{s_{p+1}}) & w_{s_p} & w_{s_{p+1}} & \cdots & 0 \\
\vdots & \ddots & \ddots & \ddots & \ddots & \ddots & \ddots & \vdots \\
0 & \cdots & \cdots & \cdots & \cdots & 0 & w_{s_m} & -w_{s_m}
\end{bmatrix}
\begin{bmatrix}
\sigma_1 \\ \sigma_2 \\ \vdots \\ \sigma_{i-1} \\ \sigma_i \\ \sigma_{i+1} \\ \vdots \\ \sigma_{j-1} \\ \sigma_j \\ \sigma_{j+1} \\ \sigma_{j+2} \\ \vdots \\ \sigma_{n-1} \\ \sigma_n
\end{bmatrix} +
\tag{3.5}
$$

$$
\kappa\beta
\begin{bmatrix}
w_{s_1} & 0 & \cdots & \cdots & \cdots & \cdots & 0 \\
\vdots & \ddots & \ddots & \ddots & \ddots & \ddots & \vdots \\
0 & \cdots & w_{s_k} & -w_{s_{k+1}} & \cdots & \cdots & 0 \\
\vdots & \ddots & \ddots & \ddots & \ddots & \ddots & \vdots \\
0 & \cdots & -w_{s_{p-1}} & w_{s_p} & w_{s_{p+1}} & \cdots & 0 \\
\vdots & \ddots & \ddots & \ddots & \ddots & \ddots & \vdots \\
0 & \cdots & \cdots & \cdots & \cdots & 0 & -w_{s_m}
\end{bmatrix}
\begin{bmatrix}
j_1 \\ \vdots \\ j_k \\ j_{k+1} \\ \vdots \\ j_{p-1} \\ j_p \\ j_{p+1} \\ \vdots \\ j_m
\end{bmatrix}
$$

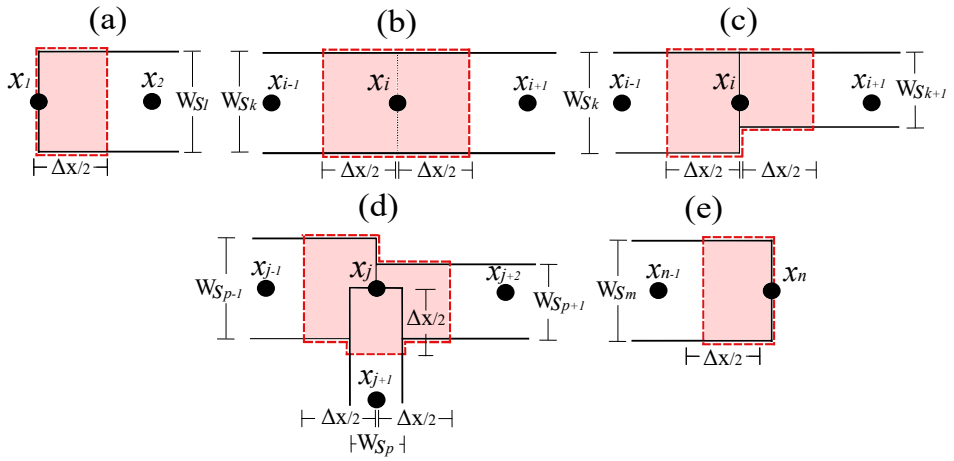


Figure 3.1: Each discretized point may be located at (a) the left boundary segment, (b) the middle of a segment, (c) an intermediate junction, (d) a via junction, and (e) the right boundary segment.The red box around each discretized point represents the corresponding area of Eq. (3.4).

3.3 Handling void formation

In the case of void formation, FDM must account for boundary condition of Eq. (2.5) at the void location. Typically, voids appear at end-points, i.e., terminal nodes of the interconnect tree. However, in more complex cases, voids may form at junction or via junction points inside an interconnect tree. In such scenarios, the tree must be restructured into subtrees, effectively ”splitting” the original tree at the void location, as illustrated in Fig. 3.2. Each subtree is then treated as an independent system, with the void location becoming a new terminal node for each of them [31]. This restructuring allows for post-void analysis to be performed individually on each subtree.

At the void location, boundary conditions of Eq. (2.2), (2.3), (2.4) and (2.5) are applied. The discretized form of the stress evolution equation at this point depends on the direction of the subtree.

1. For left and down subtrees (assuming the void is the last node of the subtree), the equation takes the form:

$$\frac{1}{2}\dot{\sigma}_n = \frac{\kappa}{\Delta x}\begin{bmatrix} \cdots & 1 & -\left(\frac{\Delta x}{\delta}+1\right) \end{bmatrix}\begin{bmatrix} \vdots \\ \sigma_{n-1} \\ \sigma_n \end{bmatrix} + \kappa\beta\begin{bmatrix} \vdots \\ j_m \end{bmatrix} \tag{3.7}$$

2. For right and up subtrees (assuming the void is the first node of the subtree), the equation becomes:

$$\frac{1}{2}\dot{\sigma}_1 = \frac{\kappa}{\Delta x}\begin{bmatrix} -\left(\frac{\Delta x}{\delta}+1\right) & 1 & \cdots \end{bmatrix}\begin{bmatrix} \sigma_1 \\ \sigma_2 \\ \vdots \end{bmatrix} + \kappa\beta\begin{bmatrix} j_1 \\ \vdots \end{bmatrix} \tag{3.8}$$

In both cases, the segment widths w_{S_1} and w_{S_m} are omitted from the above equations, since the void point is no longer considered an internal node, but instead acts as a terminal node. The remaining nodes within each subtree are governed by the standard discretized form of the ODE system, as defined in Eq. (3.5).

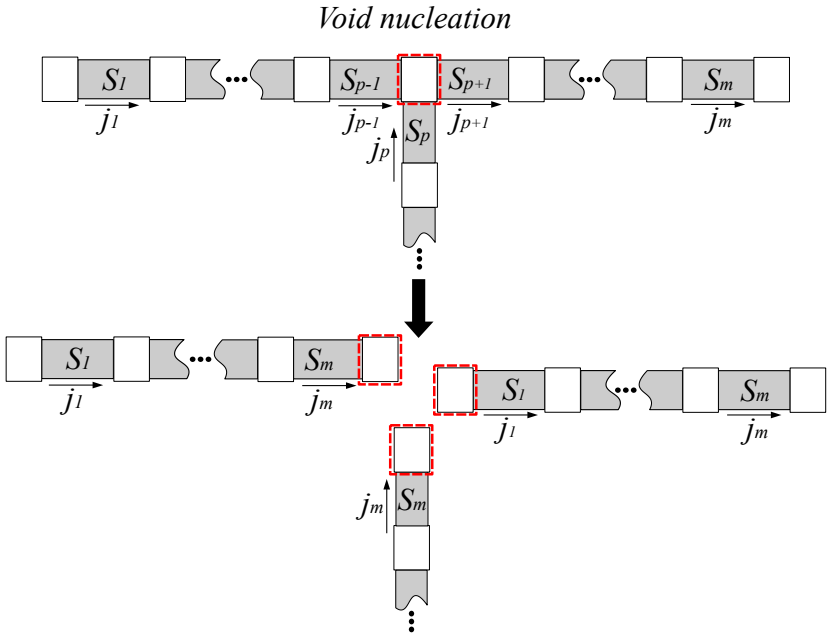


Figure 3.2: Tree splitting at a via junction due to void nucleation, resulting in independent subtrees for post-void analysis.

3.4 Proposed EM stress analysis

3.4.1 Analytical solution

Initially, we elaborate on the matrix exponential time integration that describes the EM stress evolution. The solution of Eq. (3.6) can be obtained analytically [32]. First, Eq. (3.6) can be written as:

$$\dot{\sigma}(t) = \mathbf{A}\sigma(t) + \mathbf{b}(t) \tag{3.9}$$

with

$$\mathbf{A} = \mathbf{C}^{-1}\mathbf{G}, \quad \mathbf{b}(t) = \mathbf{C}^{-1}\mathbf{B}\mathbf{j}(t) \tag{3.10}$$

Given that the stress values for all points at $t = 0$ are known [18], the solution at t can be obtained by:

$$\sigma(t) = e^{t\mathbf{A}}\sigma(0) + \int_0^t e^{(t-\tau)\mathbf{A}}\mathbf{b}(\tau)\, d\tau \tag{3.11}$$

Since the input vector $\mathbf{j}(t)$ is constant, as described in Section 3.2, we can integrate the last term of Eq. (3.11) analytically, transforming the solution to:

$$\sigma(t) = e^{t\mathbf{A}}\left(\sigma(0) + \mathbf{F}(t)\right) - \mathbf{F}(t) \tag{3.12}$$

with

$$\mathbf{F}(t) = \mathbf{A}^{-1}\mathbf{b}(t) \tag{3.13}$$

For a detailed derivation of this closed-form solution using the matrix exponential, see Appendix A.

While calculating the analytical solution, two major drawbacks arise. The first is the singularity of the ODE LTI system. More specifically, matrix $\mathbf{G}$ is non-invertible, rendering the calculation of the term $\mathbf{F}(t)$ impossible. This occurs due to the fact that the stress equations for discretized points are not independent, as there is no ”ground” stress node. The second drawback is the significant computational and memory cost of the matrix exponential operator, which arises from the increased order n of the LTI system for finer discretizations or larger trees.

3.4.2 Singularity elimination for the LTI system

To resolve the singularity of the LTI system, we need to apply an additional independent equation. According to Korhonen’s equations, the incoming and outcoming mass transport rates balance out for every discretized point. As a result, the LTI sytem can be extended with the following independent equation:

$$\sum_{1}^{n} a_i\sigma_i = 0 \tag{3.14}$$

, where a_i can be calculated using Eq. (3.4). This equation describes the mass conservation in the stress kinetics and can be used to substitute a dependent row of matrix $\mathbf{G}$. The singularity

elimination process is presented in Algorithm 1. As can be seen, the substitution of any k-th row of matrix $\mathbf{G}$ using Eq. (3.14) is performed in step 1, while the k-th row of matrix $\mathbf{G}$ is eliminated in steps 2-11.

Algorithm 1: Singularity elimination for the LTI system

Input: singular matrix $\mathbf{G}$, equation $\mathbf{Eq}_{\text{mass}}$ of Eq. (3.14), original order $\mathbf{n}$, point x_k, set $\mathbf{N}_k$ of points incident on x_k

Output: nonsingular matrix $\mathbf{G}$

1 $\mathbf{G}(k,:) = \mathbf{Eq}_{\text{mass}}$
2 **foreach** *point* $\upsilon \in N_k$ **do**
3 **for** $j = 1, \ldots, n$ **do**
4 **if** $j \neq k$ **then**
5 $\mathbf{w} = \mathbf{G}(\upsilon, k)\mathbf{G}^{-1}(k,k)\mathbf{G}(\upsilon, j)$
6 $\mathbf{G}(\upsilon, j) = \mathbf{G}(\upsilon, j) - \mathbf{w}$
7 **end**
8 **end**
9 **end**
10 $\mathbf{G}^{'} = [\mathbf{G}(1:k-1,:), \mathbf{G}(k+1:N,:)]$
11 $\mathbf{G} = [\mathbf{G}^{'}(:, 1:k-1), \mathbf{G}^{'}(:, k+1:N)]$

3.4.3 Krylov subspace-based EM stress analysis

As mentioned before, stress evolution is governed by a large system of ODEs, where direct computation of the matrix exponential is computationally infeasible due to the high dimensionality. A well-established strategy for overcoming this bottleneck is to approximate the action of the matrix exponential on a vector through Krylov subspace projection methods. For efficiently computing the matrix exponential, which plays a central role in solving LTI system, we present a model order reduction approach based on the Arnoldi procedure that estimates the stress values of a multi-segment interconnect tree for every given time t. On one hand, the Arnoldi process generates an orthonormal basis for the Krylov subspace and yields a low-dimensional Hessenberg matrix $\mathbf{H}_m$ ($m \ll n$), which approximates the behavior of the original large matrix $\mathbf{A}$. However, standard Krylov subspaces tend to favor the approximation of large-magnitude eigenvalues, which dominate short-term dynamics. On the other hand, EM is an inherently slow process, where long-term behavior is mainly dominated by the

smallest-magnitude eigenvalues of $\mathbf{A}$. Therefore, the main idea is to apply the EKS [33], in order to get the reduced order model approximating both the largest and the smallest eigenvalues of the original LTI system. The EKS is effectively the combination of the standard Krylov subspace $\mathcal{K}_{m/2}(\mathbf{A}_E, \mathbf{B}_E)$ and the inverted subspace $\mathcal{K}_{m/2}(\mathbf{A}_E^{-1}, \mathbf{B}_E)$, i.e.,

$$\begin{aligned}\mathcal{K}_m^E(\mathbf{A}_E, \mathbf{B}_E) = \mathcal{K}_{m/2}(\mathbf{A}_E, \mathbf{B}_E) + \mathcal{K}_{m/2}(\mathbf{A}_E^{-1}, \mathbf{B}_E) = \\ span\{\mathbf{B}_E, \mathbf{A}_E^{-1}\mathbf{B}_E, \mathbf{A}_E\mathbf{B}_E, \mathbf{A}_E^{-2}\mathbf{B}_E, \mathbf{A}_E^2\mathbf{B}_E, \mathbf{B}_E, \ldots, \\ \mathbf{A}_E^{(m/2)-1}\mathbf{B}_E, \mathbf{A}_E^{-m/2}\mathbf{B}_E\}\end{aligned} \tag{3.15}$$

, where:

$$\mathbf{A}_E \equiv \mathbf{C}^{-1}\mathbf{G}, \quad \mathbf{B}_E \equiv \sigma(0) + \mathbf{F}(t) \tag{3.16}$$

Note that, if the desired order is an odd number, the EKS subspace would be similar to Eq. (3.15) without the last column $\mathbf{A}_E^{-m/2}\mathbf{B}_E$. The orthogonal basis of the EKS span is stored as the columns of a projection matrix $\mathbf{V}_m = [\boldsymbol{\upsilon}_1, \ldots, \boldsymbol{\upsilon}_m] \in \mathbb{R}^{n\times m}$, which satisfies the so-called Arnoldi decomposition:

$$\mathbf{A}\mathbf{V}_m = \mathbf{V}_{m+1}\mathbf{H}_{m+1} = \mathbf{V}_m\mathbf{H}_m + \mathbf{h}_{m+1,m}\boldsymbol{\upsilon}_{m+1}\mathbf{e}_m^\intercal \tag{3.17}$$

, where $\mathbf{H}_m \in \mathbb{R}^{m\times m}$ is the upper Hessenberg matrix, which is the matrix $\mathbf{H}_{m+1}$ without the last row $(0, \ldots, 0, \mathbf{h}_{m+1,m})$, and $\mathbf{e}_m^\intercal = [0, \ldots, 0, 1]^\intercal \in \mathbb{R}^m$ is the last canonical basis vector in $\mathbb{R}^m$. Once $\mathbf{V}_m$ and $\mathbf{H}_m$ are generated, an approximation $\boldsymbol{\phi}_m(t)$ to the matrix exponential $\boldsymbol{\phi}(t) = e^{t\mathbf{A}}\mathbf{v}$ is usually computed as:

$$\boldsymbol{\phi}_m(t) = \beta\mathbf{V}_m\mathbf{H}_m e^{t\mathbf{H}_m}\mathbf{e}_1 \tag{3.18}$$

, where $\mathbf{e}_1^\intercal = [1, 0, \ldots, 0]^\intercal \in \mathbb{R}^m$ and $\beta = \left\|\sigma(0) + \mathbf{F}(t)\right\|_2$. The residual of the approximation $\boldsymbol{\phi}_m(\tau)$ with respect to the ODE system $\dot{\boldsymbol{\phi}}(t) = \mathbf{A}\boldsymbol{\phi}(t)$ is defined as:

$$\mathbf{r}(m, t) = \mathbf{A}\boldsymbol{\phi}_m(t) - \dot{\boldsymbol{\phi}}_m(t) \tag{3.19}$$

By replacing Eq. (3.17) into Eq. (3.19), the residual norm relative to the norm β is formed as:

$$\left\|\mathbf{r}(m, t)\right\| = |\beta\mathbf{h}_{m+1,m}\boldsymbol{\upsilon}_{m+1}\mathbf{e}_m^\intercal e^{t\mathbf{H}_m}\mathbf{e}_1| \tag{3.20}$$

Algorithm 2: Proposed EKS-based EM stress analysis

Input: matrix $\mathbf{A}_E \equiv \mathbf{C}^{-1}\mathbf{G}$, initial vector $\sigma(0)$, term $\mathbf{F}(t)$, desired order m, time t, budget error ϵ

Output: vector of EM stress σ at time t

1 $\mathbf{B}_E = \sigma(0) + \mathbf{F}(t)$

2 $\mathbf{V} = \mathrm{qr}([\mathbf{B}_E, \mathbf{A}_E^{-1}\mathbf{B}_E])$ `// Perform QR on initial block`

3 $\mathbf{H} \leftarrow$ zero matrix of size $m \times m$

4 $numBlocks \leftarrow m/2$ `// Since block size is 2`

5 **for** $j \leftarrow 1$ **to** $numBlocks$ **do**

6 $\quad c_j \leftarrow [2j-1, 2j]$ `// Indices for current block`

7 $\quad \boldsymbol{\upsilon}_{2j-1} \leftarrow \mathbf{V}(:, c_j[0])$ `// Second-to-last vector of` $\mathbf{V}$

8 $\quad \boldsymbol{\upsilon}_{2j} \leftarrow \mathbf{V}(:, c_j[1])$ `// Last vector of` $\mathbf{V}$

9 $\quad \mathbf{w} \leftarrow [\mathbf{A}_E \cdot \boldsymbol{\upsilon}_{2j-1}, \mathbf{A}_E^{-1} \cdot \boldsymbol{\upsilon}_{2j}]$ `// Compute new block vectors`

$\quad$ `/* Modified Gram-Schmidt orthogonalization against existing basis */`

10 $\quad$ **for** $i \leftarrow 1$ **to** j **do**

11 $\quad\quad r_i \leftarrow [2i-1, 2i]$

12 $\quad\quad \mathbf{h} \leftarrow \mathbf{V}(:, r_i)^T \cdot \mathbf{w}$

13 $\quad\quad \mathbf{w} \leftarrow \mathbf{w} - \mathbf{V}(:, r_i) \cdot \mathbf{h}$

14 $\quad\quad \mathbf{H}(r_i, c_j) \leftarrow \mathbf{H}(r_i, c_j) + \mathbf{h}$

15 $\quad [\upsilon_{new}, \mathbf{h}] \leftarrow \mathrm{qr}(\mathbf{w}, 0)$ `// Orthonormalize new block`

16 $\quad \mathbf{V} \leftarrow [\mathbf{V}, \upsilon_{\text{new}}]$ `// Append to Krylov basis`

17 $\quad r_{j+1} \leftarrow [2j+1, 2j+2]$ `// Row indices for new part of` $\mathbf{H}$

18 $\quad \mathbf{H}(r_{j+1}, c_j) \leftarrow \mathbf{h}$

$\quad$ `/* Early termination check (residual norm) */`

19 $\quad$ **if** $\left\|\mathbf{r}(m,t)\right\| < \epsilon$ **then**

20 $\quad\quad m = j$ `// Truncate basis`

21 $\quad\quad$ break

22 $\mathbf{H}_m = \mathbf{H}(1:m, :),\ \mathbf{V}_m = \mathbf{V}(:, 1:m)$

23 $\sigma(t) = \beta \mathbf{V}_m e^{t\mathbf{H}_m} \mathbf{e}_1 - \mathbf{F}(t)$

The proposed EKS-based stress analysis is outlined in Algorithm 2. In particular, the EKS is constructed in a block-wise manner, where two basis vectors are generated per iteration by alternately applying the system matrix $\mathbf{A}_E$ and its inverse, as shown in step 9. This dual ex-

pansion strategy allows the resulting subspace to capture both the high- and low-frequency eigenvalues of the system, which are essential for accurately modeling the slow dynamics of EM stress evolution. Each newly generated pair of vectors is orthogonalized against the existing basis using a modified Gram-Schmidt process (steps 10–14) and appended to the basis matrix $\mathbf{V}$. In parallel, matrix $\mathbf{H}$ is also constructed incrementally on a block-by-block basis (steps 10–14,18), with new rows and columns added corresponding to each new pair of vectors. This block-based strategy not only enhances numerical stability but also accelerates the construction of the EKS by reducing the number of required iterations. The algorithm continues for m iterations until the residual error of Eq. (3.20) becomes smaller than a tolerance error ϵ, ensuring convergence of the method. Once the reduced basis $\mathbf{V}$ is computed in step 23, it is truncated and used to estimate the stress vector at time t via projection of the matrix exponential. In particular, the EKS needs to be generated only once during the transient analysis, after which it can be efficiently reused to evaluate stress at any desired time point.

3.4.4 Rational Krylov subspace for the matrix exponential

Although the EKS method effectively captures both extremal eigenvalues of the system matrix $\mathbf{A}$, its convergence may still be slow when higher accuracy is required. To further improve convergence, we propose the use of the RKS, which has been widely recognized as a powerful alternative for improving convergence rates. Krylov subspace methods in general approximate the action of large-scale matrix functions on a vector by projecting the problem onto a lower-dimensional subspace. Although the projection process is usually performed by an Arnoldi procedure that is independent of the subspace selection, the selected subspace can critically affect the iterations required to converge to the final solution. Rational Krylov subspaces, in particular, can provide significantly faster convergence by incorporating shifted inverse operations into the basis construction. However, a critical challenge in rational Krylov methods lies in selecting appropriate shift parameters. Poor shift choices can severely degrade the quality of the subspace [34]. To address this issue, we propose an adaptive parameter-free procedure, which is able to autogenerate the required shifts, for computing the rational Krylov subspace. As a result, our method can accurately approximate the matrix exponential operator by capturing the important eigenvalues, and efficiently estimate the stress values of a multi-segment interconnect tree at any time t. Given a sequence of shifts $s = \{s_1, s_2, \ldots, s_m\}$, the rational Krylov subspace is defined as:

$$\mathcal{K}_m^R(\mathbf{A}_E, \mathbf{B}_E, s) = span\{\mathbf{B}_E, (\mathbf{A}_E - s_1\mathbf{I})^{-1}\mathbf{B}_E, \ldots, \prod_{j=1}^{m-1}(\mathbf{A}_E - s_j\mathbf{I})^{-1}\mathbf{B}_E\} \tag{3.21}$$

where

$$\mathbf{A}_E \equiv \mathbf{G}^{-1}\mathbf{E}, \quad \mathbf{B}_E \equiv \sigma(0) + \mathbf{A}^{-1}\mathbf{b} \tag{3.22}$$

The orthogonal basis of the rational subspace is stored as the columns of a projection matrix $\mathbf{V}_m = [\boldsymbol{\upsilon}_1, \ldots, \boldsymbol{\upsilon}_m] \in \mathbb{R}^{n\times m}$, which satisfies the Arnoldi decomposition:

$$(\mathbf{A}_E - s_m\mathbf{I})^{-1}\mathbf{V}_m = \mathbf{V}_m\mathbf{H}_m + \mathbf{h}_{m+1,m}\boldsymbol{\upsilon}_{m+1}\mathbf{e}_m^\intercal \tag{3.23}$$

where $\mathbf{H}_m \in \mathbb{R}^{m\times m}$ is the upper Hessenberg matrix, and $\mathbf{e}_m^\intercal = [0, \ldots, 0, 1]^\intercal \in \mathbb{R}^m$ is the last canonical basis in $\mathbb{R}^m$. Once $\mathbf{V}_m$ and $\mathbf{H}_m$ are computed, an approximation $\boldsymbol{\phi}_m(t)$ to the matrix exponential $\boldsymbol{\phi}(t) = e^{t\mathbf{A}_E}\mathbf{v}$ can be calculated by:

$$\boldsymbol{\phi}_m(t) = \beta\mathbf{V}_m e^{t\tilde{\mathbf{H}}_m}\mathbf{e}_1 \tag{3.24}$$

where $\tilde{\mathbf{H}}_m = ({\mathbf{H}_m}^{-1} - \mathbf{I})/s_m$, $\mathbf{e}_1^\intercal = [1, 0, \ldots, 0]^\intercal \in \mathbb{R}^m$, and $\beta = \left\|\sigma(0) + \mathbf{A}^{-1}\mathbf{b}\right\|_2$. The residual of the approximation $\boldsymbol{\phi}_m(\tau)$ with respect to the ODE system $\dot{\boldsymbol{\phi}}(t) = \mathbf{A}_E\boldsymbol{\phi}(t)$ is defined as:

$$\mathbf{r}(m, t) = \mathbf{A}_E\boldsymbol{\phi}_m(t) - \dot{\boldsymbol{\phi}}_m(t) \tag{3.25}$$

By substituting Eq. (3.23) into Eq. (3.25), the residual norm relative to $|\beta|$ is formulated as:

$$\left\|\mathbf{r}(m, t)\right\| = \left|\beta\mathbf{h}_{m+1,m}\boldsymbol{\upsilon}_{m+1}\frac{\mathbf{A}_E - s_m\mathbf{I}}{s_m}\mathbf{e}_m^\intercal\mathbf{H}_m^{-1}e^{t\tilde{\mathbf{H}}_m}\mathbf{e}_1\right| \tag{3.26}$$

The proposed RKS-based stress analysis procedure is summarized in Algorithm 3. The goal of the algorithm is to construct the RKS that accurately approximates the action of the matrix exponential, while minimizing the residual norm defined in Eq. (3.26). The subspace is iteratively generated in steps 7–16, where each iteration enriches the basis using a newly selected shift parameter. The process begins with an initial shift value s_1, typically chosen near an eigenvalue of system matrix $\mathbf{A}$ that significantly influences the system's dynamics. At each iteration, the current basis vector is transformed using a shifted inverse operator, and then orthogonalized against the existing basis vectors. The reduced matrix $\mathbf{T} = \mathbf{V}^\top\mathbf{A}\mathbf{V}$ is then updated, and its eigenvalues are used to determine the next optimal shift. To adaptively guide the subspace construction, Algorithm 4 is employed to select the next shift s_{m+2}, based on rational approximation theory. This adaptive selection process allows the method to focus on the spectral components that are most critical in accurately approximating the matrix

exponential. Once the residual norm falls below a user-defined tolerance ϵ (step 13), the iterative process terminates. In step 17, the final stress vector $\boldsymbol{\sigma}(t)$ is computed by projecting the matrix exponential onto the RKS. Importantly, the generated rational Krylov subspace can be reused to calculate the stress values across multiple time points during the transient analysis.

Algorithm 3: Rational Krylov-based EM stress analysis

Input: $\mathbf{A}_E \equiv \mathbf{G}^{-1}\mathbf{E}$, $\sigma(0)$, $\mathbf{f} \equiv \mathbf{A}^{-1}\mathbf{b}$, desired size $m_{\max}$, time t, threshold ϵ, init. shift s_1

Output: Stress σ at time t

1 Compute $\mathbf{B}_E = \sigma(0) + \mathbf{f}$

2 Compute initial vector $\tilde{\boldsymbol{\upsilon}}_1 = (\mathbf{A}_E - s_1\mathbf{I})^{-1}\mathbf{B}_E$

3 Normalize vector $\boldsymbol{\upsilon}_1 = \tilde{\boldsymbol{\upsilon}}_1 / \|\tilde{\boldsymbol{\upsilon}}_1\|$, $\mathbf{V} = \boldsymbol{\upsilon}_1$

4 Compute $\boldsymbol{\tau} = \boldsymbol{\upsilon}_1{}^T \mathbf{A}_E \boldsymbol{\upsilon}_1$

5 Set $s_2 = \texttt{newshift}(\boldsymbol{\tau}, s_1, \{s_1, \boldsymbol{\tau}\})$

6 **for** $m = 1, \ldots, m_{max}$ **do**

7 $\quad \tilde{\boldsymbol{\upsilon}}_{m+1} = (\mathbf{A}_E - s_{m+1}\mathbf{I})^{-1}\boldsymbol{\upsilon}_m$

8 $\quad$ Orthogonalize $\tilde{\boldsymbol{\upsilon}}_{m+1}$ with respect to $\boldsymbol{\upsilon}_1, \ldots, \boldsymbol{\upsilon}_m$

9 $\quad$ Obtain the coefficients of $\mathbf{H}_{m+1,m}$

10 $\quad$ Scale $\boldsymbol{\upsilon}_{m+1} = \tilde{\boldsymbol{\upsilon}}_{m+1} / \|\tilde{\boldsymbol{\upsilon}}_{m+1}\|$, $\mathbf{V} = [\mathbf{V}, \boldsymbol{\upsilon}_{m+1}]$

11 $\quad$ Compute $\mathbf{T} = \mathbf{V}^T \mathbf{A}_E \mathbf{V}$

12 $\quad$ Compute eigenvalues $\{\lambda_1, \ldots, \lambda_m\}$ of $\mathbf{T}$

13 $\quad$ Set $s_{m+2} = \texttt{newshift}(\{\lambda_k\}_{k=1:m}, \{s_k\}_{k=1:m}, \{s_k\}_{k=1:m+1})$

14 $\quad$ **if** $\left\|\mathbf{r}(m,t)\right\| < \epsilon$, **then** exit the loop

15 **end**

16 Truncate basis to order m, $\mathbf{H}_m = \mathbf{H}(1:m,:)$, $\mathbf{V}_m = \mathbf{V}(:,1:m)$

17 Compute the stress solution $\sigma(t) = \beta \mathbf{V}_m e^{t\tilde{\mathbf{H}}_m}\mathbf{e}_1 - \mathbf{f}$

Algorithm 4: Selection of a new shift parameter

Input: $\{\lambda_k\}_{k=1:m}, \{s_k\}_{k=1:m}, \{\eta_k\}_{k=1:l}$

Output: new shift s_{new}

1 **for** $j = 1, \ldots, l-1$ **do**

2 $\quad \sigma_j = \texttt{argmax}_{\sigma \in [\eta_j, \eta_{j+1}]}\left(\frac{1}{|q_m(\sigma)|}\right)$, $q_m(z) = \Pi_{i=1}^{m} \frac{z-\lambda_k}{z-s_k}$

3 **end**

4 $s_{\text{new}} = \texttt{argmax}\left(\frac{1}{|q_m(\sigma_1,\ldots,\sigma_{l-1})|}\right)$

3.4.5 Nucleation time estimation

To estimate the nucleation time t_{nuc}, we propose a robust root-finding framework based on the Newton-Raphson method. Importantly, this method reuses the EKS produced by Algorithm 2, enabling fast and direct evaluation of stress values at arbitrary times. The complete procedure is summarized in Algorithm 5.

Algorithm 5: Nucleation time estimation via Newton-Raphson

Input: $\mathbf{A}$, $\mathbf{H}_m$,$\mathbf{V}_m$, threshold ϵ, critical stress σ_{crit}, step size factor α, iterations max_iter, maximum year $t_{\max}$

Output: Time to nucleation t_{nuc}, nucleation point x_{nuc}

1 Define uniform time grid $\{\boldsymbol{\tau}_k\}_{k=1}^{N} \subseteq [0, t_{\max}]$

2 Compute stress matrix $\boldsymbol{\Sigma}_{i,k} \leftarrow [\beta \mathbf{V}_m e^{t\mathbf{H}_m}\mathbf{e}_1 - \mathbf{F}(\tau_k)]_{\text{i}}$ where $\boldsymbol{\Sigma} \in \mathbb{R}^{n\times N}$

3 $\boldsymbol{\sigma}_k^{\max} \leftarrow \max_i \boldsymbol{\Sigma}_{i,k}$

4 **if** $\boldsymbol{\sigma}_k^{max} < \sigma_{crit}$ *for all* k **then**

5 **return** *Tree is 'Immortal'*

6 $k_{\min} \leftarrow \min\{k : \boldsymbol{\sigma}_k^{\max} \geq \sigma_{\text{crit}}\}$

7 $t \leftarrow \boldsymbol{\tau}_{k=k_{\min}}$ // Initial time guess

8 $t_{\text{backup}} \leftarrow t + (\boldsymbol{\tau}_{k+1} - \boldsymbol{\tau}_k)$ // Backup time in case of fail

9 $\mathbf{x}_k \leftarrow \arg\max_i \boldsymbol{\Sigma}_{i,k}$

10 $x_{\text{nuc}} \leftarrow \mathbf{x}_{k=k_{\min}}$ // Location of nucleation point

11 **for** $i \leftarrow 1$ **to** max_iter **do**

12 **if** $|f(t)| < \epsilon$ **then** break

13 $t_{\text{new}} \leftarrow t - \alpha \cdot \frac{f(t)}{f'(t)}$

14 **while** $t_{new} < 0$ **do**

15 $\alpha \leftarrow \alpha/2$

16 $t_{\text{new}} \leftarrow t - \alpha \cdot \frac{f(t)}{f'(t)}$

17 $t \leftarrow t_{\text{new}}$

18 **if** $t > t_{max}$ or divergence **then** $t \leftarrow t_{\text{backup}}$

19 **return** $t_{nuc} = t,\ x_{nuc},$ *Tree is 'Susceptible'*

20 **Def** $f(t) = [\beta \mathbf{V}_m e^{t\mathbf{H}_m}\mathbf{e}_1 - \mathbf{F}(t)]_{x_{\text{nuc}}} - \sigma_{\text{crit}}$

21 **Def** $f'(t) = [\mathbf{A}\beta \mathbf{V}_m e^{t\mathbf{H}_m}\mathbf{e}_1]_{x_{\text{nuc}}}$

It begins with a fully physics-informed vectorized initialization. In steps 1–3, the algorithm constructs a uniform time grid $\{\tau_k\}_{k=1}^{N} \subseteq [0, t_{\max}]$, evaluates the stress field at each time

step, and extracts the maximum stress value $\boldsymbol{\sigma}_k^{\max}$ from the resulting stress matrix $\boldsymbol{\Sigma} \in \mathbb{R}^{n \times N}$. If no value of $\boldsymbol{\sigma}_k^{\max}$ exceeds the critical threshold σ_{crit}, the interconnect tree is classified as *Immortal* and the algorithm is terminated. Otherwise, in steps 6–10, the method identifies the first time t_k at which the threshold is crossed and sets this as the initial guess time t_{guess}. The corresponding location x_{nuc} is tracked as the likely void nucleation site, and a backup estimate time t_{backup} is defined to enhance convergence reliability. Once a valid initial guess time is determined, in steps 6–18, we perform a Newton-Raphson iteration to refine the nucleation time by solving $f(t) = [\sigma(t)]_{x_{\text{nuc}}} - \sigma_{\text{crit}} = 0$ at nucleation point x_{nuc}. To compute the $f'(t)$, we differentiate the stress function of Eq. (3.13) with respect to time t, assuming term $\mathbf{F}(t)$ is constant. This operation leads to $\frac{d\sigma(t)}{dt} = Ae^{tA}\left(\sigma(0) + \mathbf{F}(t)\right)$. By applying the Krylov-based matrix exponential approximation of Eq. (3.18), we obtain $f'(t) = [A\beta \mathbf{V}_m e^{t\mathbf{H}_m}\mathbf{e}_1]_{x_{\text{nuc}}}$, which is the final form used for the Newton-Raphson update step. To ensure that the updated time remains within physical bounds (i.e., $t > 0$), the Newton-Raphson step is scaled by a damping factor α, which is adaptively reduced. This backtracking mechanism improves convergence stability, especially near sharp gradients or boundaries. In cases where divergence or stagnation is detected (i.e., $t > t_{\max}$), the algorithm triggers fail-safe switching to the backup guess time t_{backup}. Finally, the method returns the refined nucleation time t_{nuc} and location x_{nuc}, along with a classification label based on stress evolution and convergence outcome.

3.5 Experimental results

In this Section, we present three sets of experimental results to demonstrate the accuracy and scalability of our proposed method for both pre-void and post-void analysis. All three experiments are conducted using the EKS, which serves as the core technique in our framework. Following this, we include a complementary evaluation of the RKS, to explore its accuracy and compare its performance against EKS across large-scale benchmarks. First, in Section 3.5.1, we apply our method to a complex artificial segment tree with varying widths, as part of a proof-of-concept experiment. Next, in Section 3.5.2, we showcase the scalability of our algorithms on interconnect tree with increasing number of via junctions (i.e., T junctions), demonstrating their linear behavior. Then, in Section 3.5.3, to validate its applicability on large-scale power grids, we test our algorithms on OpenROAD benchmarks. Finally, in Section 3.5.4, we evaluate the alternative RKS-based method on an OpenROAD tree structure,

followed by a detailed evaluation in multiple large-scale power grid designs.

Our method was compared against the golden solution provided by COMSOL V6.1, a Finite Element Method (FEM) based tool, across all three parts of the evaluation. Additionally, it was evaluated against other state-of-the-art methods based on the matrix exponential, such as Higham [2] for post-void analysis and scalability, and Expokit [3], which was used exclusively for scalability assessment. In all experiments, the interconnects are assumed to be Cu DD, and since there is no mass transfer through the vias, the EM analysis is conducted independently for each layer and each tree of the power grid. Table 3.1 outlines the interconnect characteristics [35] used in our simulations.

Table 3.1: Cu DD interconnect characteristics for EM analysis

Name	**Description**	**Value**
Z^*	Effective charge number	1
e	Electron charge	$1.6 \times 10^{-19}\ C$
ρ	Resistivity	$2.25 \times 10^{-8}\ \Omega m$
$\mathcal{B}$	Bulk modulus of the material	$28\ GPa$
Ω	Atomic volume for the metal	$1.18 \times 10^{-29}\ m^3$
D_0	Diffusivity constant	$1.3 \times 10^{-9}\ m^2/s$
k_B	Boltzmann's constant	$1.38 \times 10^{-23}\ J/K$
T	Temperature	$378\ K$

The proposed approach was developed in MATLAB R2021a, utilizing its built-in numerical toolset. However, to enhance the computational efficiency of our method, the Intel MKL Pardiso package was used to directly solve large-scale systems with improved performance. For the Newton-Raphson algorithm, the critical stress threshold was defined at 50MPa, while the variable t_{max} was set at 20 years, reflecting a typical design lifespan in processor design. Additional parameters for this algorithm include a convergence tolerance of $\epsilon = 10^{-2}$, a damping factor $\alpha = 10^3$, and a maximum iteration count of $max_iter = 10^3$. To ensure a direct and efficient comparison between the proposed method and COMSOL, we used the LiveLink™ for MATLAB interface. This integration enabled seamless data exchange and ensured an accurate evaluation of the experimental results. Specifically, the function *mphinterp* was employed to interpolate the COMSOL solution onto the discretization points of the proposed method, ensuring consistency in the evaluation metrics. The experiments were ex-

ecuted on a high-performance Windows system with 32 GB of RAM and a 4.7 GHz Intel Core i9-9900k processor with 16 threads, ensuring robust computational capacity.

COMSOL v6.1 was used with the Coefficient Form PDE interface, which allows direct implementation of Korhonen's PDE. The geometry was modeled as a 2D multi-segment geometry, and material parameters were assigned per segment. Boundary conditions were defined using the Flux/Source formulation, enabling accurate specification of both zero-flux (Neumann) and non-zero-flux conditions at segment boundaries. The mesh resolution was selected to match the spatial accuracy of the FDM discretization used in our method. In particular, quad meshing was used as the default strategy to preserve element alignment across wire segments, while triangular meshing was enabled only in the case of quad generation failure. Finally, COMSOL time-domain simulations were performed using an implicit BE solver with absolute and relative tolerances set to 10^{-6} and a fixed time step of $\Delta t = 0.05$ years matching the AEKS-MM simulation grid.

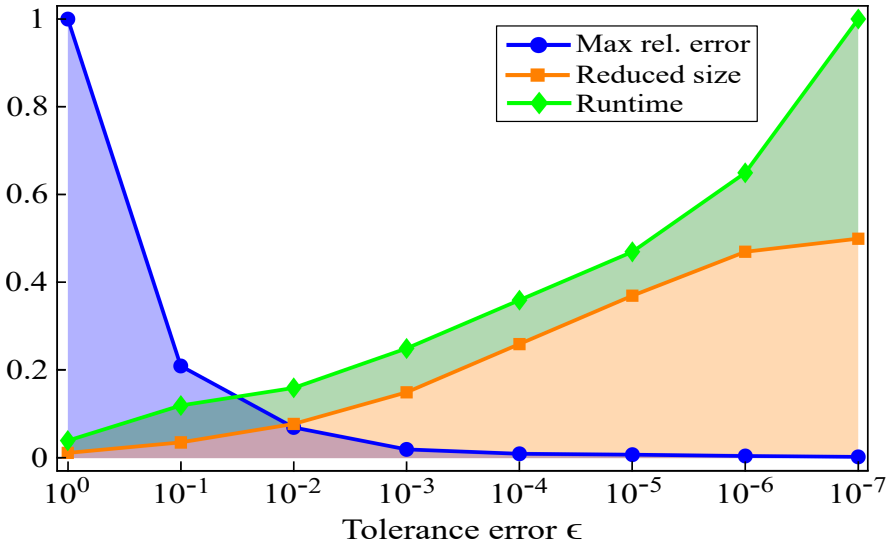


Figure 3.3: Tolerance selection for optimal trade-off

Before proceeding with the experimental evaluation, we determined the optimal error parameter for Algorithm 2 to balance accuracy and performance. To achieve this, we applied our proposed method across various error tolerance levels on an interconnect tree similar to Fig. 3.6, containing 10^3 T junctions. Fig. 3.3 presents the maximum relative error at $t = 10$ years obtained from the proposed method compared to COMSOL, the computational time of Algorithm 2, and the number of columns in the EKS. To ensure a fair comparison and highlight the correlations between these metrics, all variables were normalized in the range

$[0, 1]$. From the results, we observe that a tolerance error in the range of $[10^{-3}, 10^{-2}]$ provides an optimal trade-off. At this range, the maximum relative error is sufficiently reduced, while the reduced order remains within practical limits and the computational time does not escalate significantly. Thus, choosing a tolerance error around 10^{-3} ensures high accuracy without excessive computational cost. This tolerance parameter study was specific to the EKS method and was not required for RKS, as the adaptive shift selection mechanism governs its convergence.

3.5.1 Results on an eight-segment tree

We constructed an eight-segment interconnect tree with four T junctions, where each segment was assigned different width and current density. The segment widths are defined as follows: $w_1 = w_2 = 0.5\ \mu m$, $w_3 = w_4 = w_5 = 0.4\ \mu m$, $w_6 = w_7 = w_8 = 0.25\ \mu m$, while the segment lengths are depicted in Fig. 3.4. The corresponding constant current densities are: $j_1 = -9 \times 10^9\ A/m^2$, $j_2 = 9 \times 10^9\ A/m^2$, $j_3 = -2 \times 10^{10}\ A/m^2$, $j_4 = 5 \times 10^9\ A/m^2$, $j_5 = -1 \times 10^{10}\ A/m^2$, $j_6 = 2.85 \times 10^{10}\ A/m^2$, $j_7 = -5 \times 10^9\ A/m^2$, and $j_8 = 1 \times 1^{10}\ A/m^2$. For this specific example, to align the FEM method with our FDM approach, we set quad meshing in COMSOL with a width equal to our discretization step Dx. This ensures that the number of discretized points in FDM and the number of elements in FEM are exactly the same. As a result, the error introduced by approximating FEM with FDM and simultaneously enhances the correspondence between spatial points and stress values.

Pre-void EM assessment

To assess the stress evolution before void formation, we performed a transient simulation at $t = 20$ years, as illustrated in Fig. 3.4(a). The colorbar depicts the spatial distribution of the stress build-up across the artificial tree. The tuples next to the boundary and junction nodes represent stress values computed by our proposed method and COMSOL, demonstrating close agreement. In Fig. 3.4(b), the relative error computed along the interconnect tree remains well below 0.8%, confirming the reliability of the reduced order $m = 7$, using a discretization step of $Dx = 0.5\ \mu m$. Furthermore, as depicted in Fig. 3.4(c), the pre-void stress evolution in the horizontal segments of the artificial tree was evaluated at $t = 5$, $t = 10$, and $t = 20$ years, demonstrating that the proposed method accurately follows the COMSOL solution with minimal deviation.

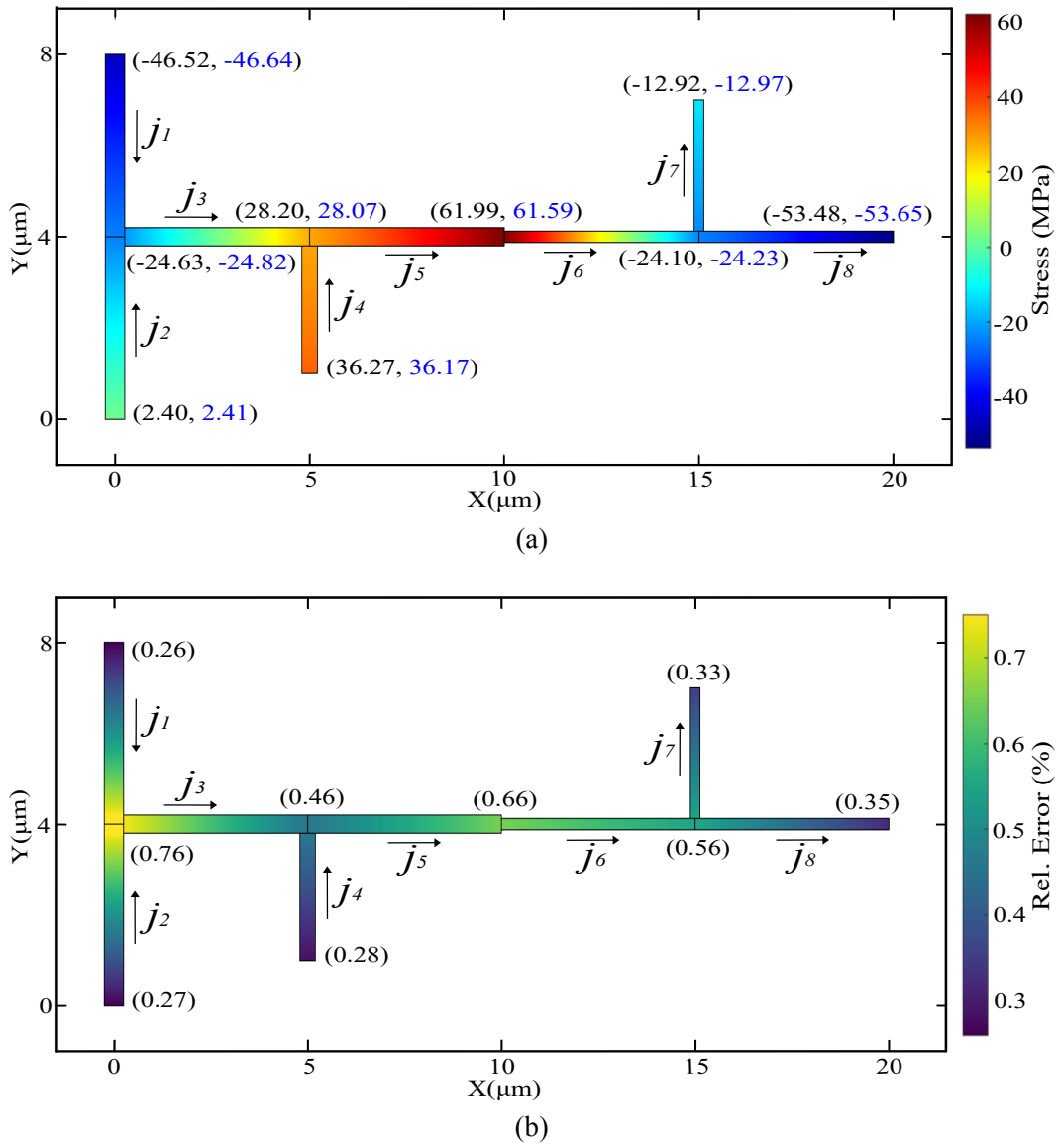
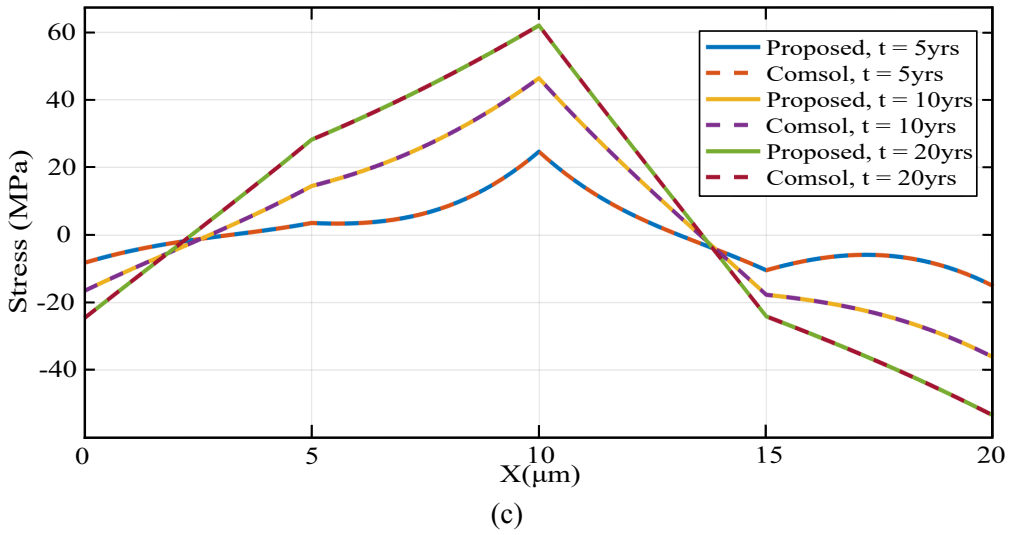


Figure 3.4: (a): Comparison of EM stress at $t = 20$ years, with stress values at each node presented as tuples, where the proposed solution is shown in black and the COMSOL solution in blue text. (b): The relative error between our proposed solution and the COMSOL solution at $t = 20$ years.

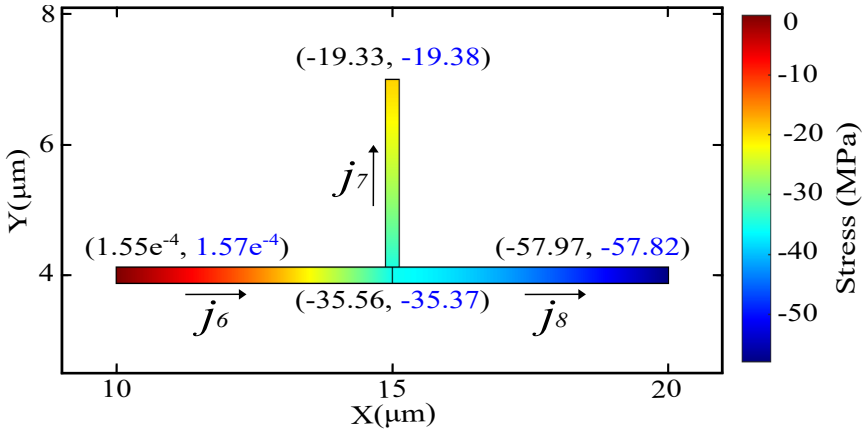


(c)

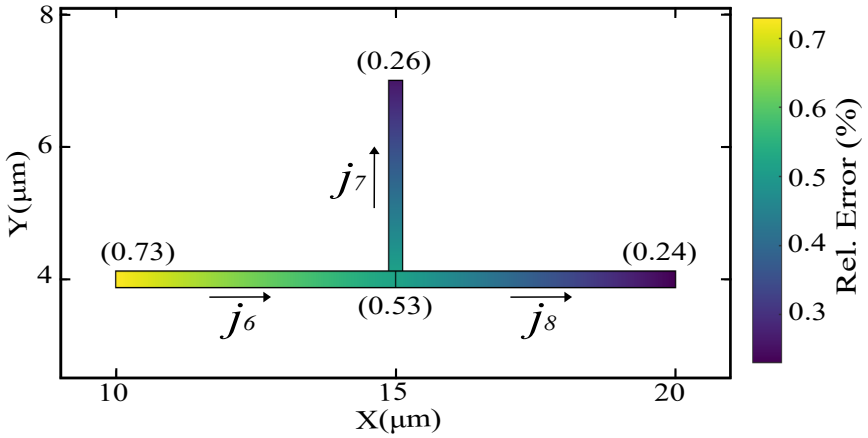
Figure 3.4: (c): Nucleation phase validation on the horizontal segments of the tree at $\boldsymbol{t = 5}$, $\boldsymbol{t = 10}$, and $\boldsymbol{t = 20}$ years.

Void formation and transition to the growth phase

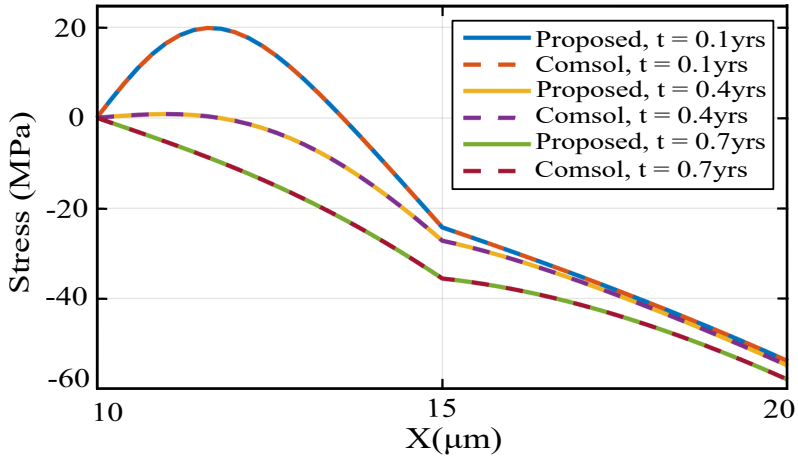
As observed in Fig. 3.4, at $(x, y) = (10, 4)\ \mu m$, the stress exceeds the critical threshold before $t = 20$ years, leading to void nucleation and marking the shift from the pre-void to the growth phase. For the growth phase simulation, we used the pre-void stress profile as the initial condition at the moment when $\sigma(x, y, t) = \sigma_{citical}$ at any point (x, y), while maintaining the same current density distribution. vAs discussed in Section 3.3, the void formation causes the interconnect tree to split into two independent subtrees: the left subtree, consisting of segments (1,2,3,4,5), and the right subtree, comprising segments (6,7,8). For this study, we focused on the right subtree, performing post-void stress simulations while maintaining the same spatial discretization step. In Fig. 3.5(a), we observe that at $t = 0.7$ years after the void nucleation, the stress near the void has reduced to near-zero levels, confirming the expected EM stress relaxation mechanisms. Additionally, Fig. 3.5(b) shows that the relative error remains below 0.8%, further validating the accuracy of our proposed method for the growth phase. Finally, in Fig. 3.5(c), we computed the post-void stress evolution at $t = 0.1$, $t = 0.4$, and $t = 0.7$ years. The stress profiles obtained from the proposed method and COMSOL remain nearly identical across the tree throughout the simulation period, with stress values near the void approaching zero and progressively decreasing.



(a)



(b)



(c)

Figure 3.5: (a): Comparison of the post-void stress at $t = 0.7$ years, with stress values at each node presented as tuples, where the proposed solution is shown in black and the COMSOL solution in blue text.(b): The relative error between our proposed solution and the COMSOL solution at $t = 0.7$ years. (c) Growth phase validation on the horizontal segments of the right subtree at $t = 0.1$, $t = 0.4$, and $t = 0.7$ years.

3.5.2 Scalability analysis

Table 3.2 presents the execution time of the proposed method, along with the exponential methods Higham [2] and Expokitt [3], as well as COMSOL, for an increasing number of successive T junctions as shown in Fig. 3.6. All methods calculate the hydrostatic stress at $t = 10$ years. Note that in an interconnect tree with n T junctions, there are $2n + 1$ segments. For the proposed method, a discretization step was chosen such that each segment corresponds to 20 points with the dimensions of horizontal segments being 10 μm in length and 0.4 μm in height, and the dimensions of vertical segments being 5 μm in length and 0.2 μm in height. In Table 3.2, $t_{\text{exp_init}}$ refers to the execution time for computing $\mathbf{F}(t)$; and $t_{\text{exp_sol}}$ corresponds to the total runtime of Algorithm 2. The problem formulation time was not included to ensure that the pure speedup of our proposed approach against other methods is not affected. Additionally, to ensure a fair comparison of COMSOL's runtime with other methods, only the stress computation time was measured, excluding the FEM discretization process.

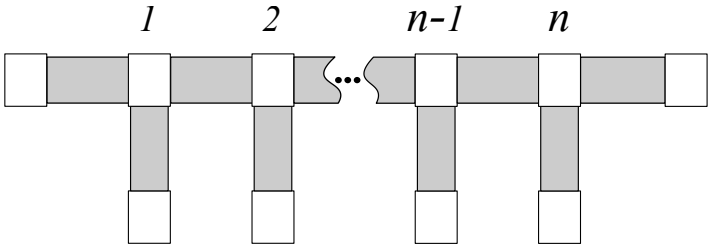


Figure 3.6: An interconnect with $\mathbf{n}$ successive $\mathbf{T}$ juntions.

From Table 3.2, we observe that the proposed approach is significantly faster than the other methods for any number of n T junctions, with the execution time difference increasing as the problem size grows. It is worth noting that the term $\mathbf{F}(t)$, is the most time consuming part of the proposed method. However, this computation is performed only once before the transient analysis. In Fig. 3.7, we present the speedups achieved by the proposed method, which appears to increase linearly compared to the other approaches. As can be seen, our methodology can be three orders of magnitude faster than COMSOL, with a maximum runtime speedup of 416.02×. The significant speedup is due to COMSOL's dependence on numerical analysis, which requires evaluating all previous time-step solutions to compute the current one, leading to increased computational overhead. Furthermore, the proposed method remains more efficient for higher values of n compared to Higham [2] and Expokit [3], achieving an average runtime speedup of 30.7× and 5.31×, respectively. This

performance advantage is primarily due to Higham [2] and Expokit [3] relying on Taylor series expansion, with the former applying it directly and the latter utilizing it through the Krylov subspace, both of which impact their efficiency in large-scale models.

Table 3.2: Runtime comparison of the proposed method and COMSOL for increasing number of T junctions

n	**Proposed method (seconds)**			**Higham (seconds)**	**Expokit (seconds)**	**COMSOL (seconds)**
	$t_{\text{exp_init}}$	$t_{\text{exp_sol}}$	t_{all}			
100	0.015	0.001	0.016	0.31	0.03	3.61
500	0.063	0.002	0.066	1.50	0.25	16.66
1000	0.097	0.005	0.102	2.56	0.51	31.78
2000	0.212	0.008	0.221	5.62	1.14	76.99
10000	1.716	0.030	1.746	57.58	9.76	601.58
20000	2.374	0.058	2.432	106.55	16.81	906.21
50000	4.062	0.143	4.205	195.05	36.35	1749.23

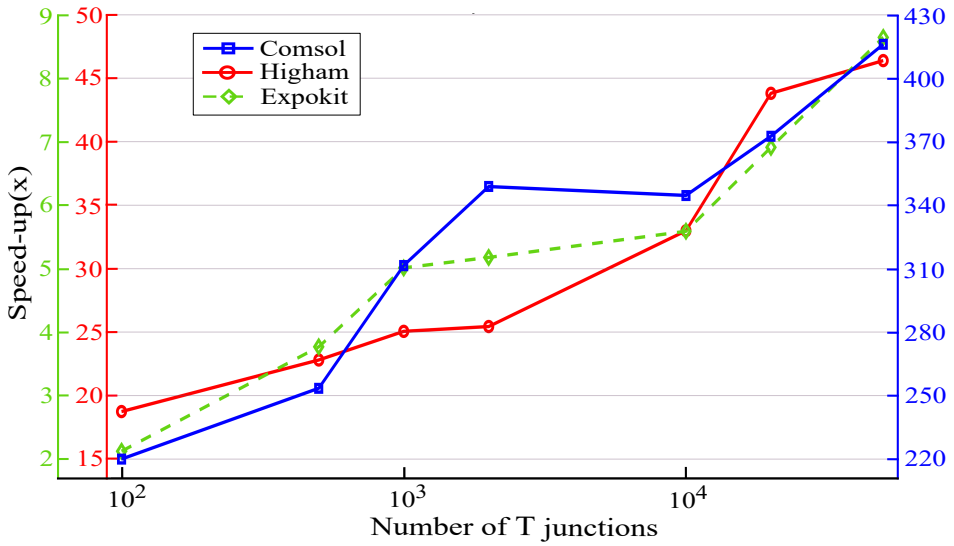


Figure 3.7: Speedup comparison of the proposed method over COMSOL, Higham [2], and Expokit [3] across different numbers of T-junctions.

3.5.3 Analysis on OpenROAD power grid designs

In order to perform analysis for both phases on large-scale power grids, we employed several OpenROAD circuits designed using commercial 12 nm FinFET, commercial 28 nm FD-SOI, and Nangate 45 nm technologies. More specifically, these benchmarks are built as mesh-like orthogonal structures, on which we apply the BFS traversal algorithm to identify the boundary segments and via segments, then decompose the meshes into multi-segment trees. Additionally, these benchmarks are synthesized using the open-source tool OpeNPDN [36], while the IR drop and current densities per segment are computed using PDNSim [37]. Due to COMSOL's inefficiency in handling very large circuits, we chose to analyze only the largest tree from each benchmark, as it indicates the worst-case scenario in terms of runtime and accuracy. The largest trees are defined as those with the longest overall segment length, providing a more geometry-aware measure of interconnect complexity. The analysis of each benchmark was carried out through the following three-step procedure:

1. Apply the Newton-Raphson procedure to determine the nucleation time and location.
2. Split the tree at the nucleation point into two or more subtrees.
3. Select the largest subtree and perform post-void analysis during the growth phase.

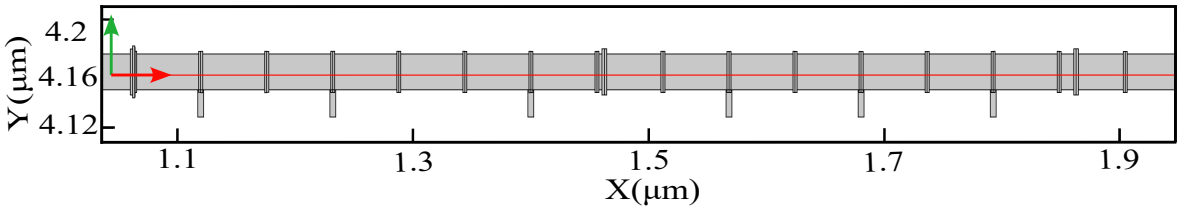
Evaluation of nucleation phase metrics

The results for the largest tree of each OpenROAD benchmark during the nucleation phase are summarized in Table 3.3. Specifically, *#Segments* indicates the total number of horizontal and vertical (via) segments per tree, while *#Discr. step* refers to the discretization step for the spatial coordinate. *#Initial size* represents the total number of points generated by the FDM procedure, and *#Reduced size* denotes the size of the resulting EKS. We also report the execution time and the number of iterations required by the Newton-Raphson algorithm 5. Finally, for a fixed time point $t = 20$ years, we provide the runtime of our proposed methodology (Algorithm 2), the runtime of the process simulation performed using COMSOL, along with the corresponding speedup and accuracy metrics. From Table 3.3, we observe that the Newton-Raphson algorithm demonstrates extremely fast convergence, requiring only a small number of iterations, typically less than 50 for most benchmarks. This confirms its suitability and efficiency for solving the nonlinear equations arising in the nucleation phase. Moreover, our method is up to four orders of magnitude faster than COMSOL, with speedups ranging

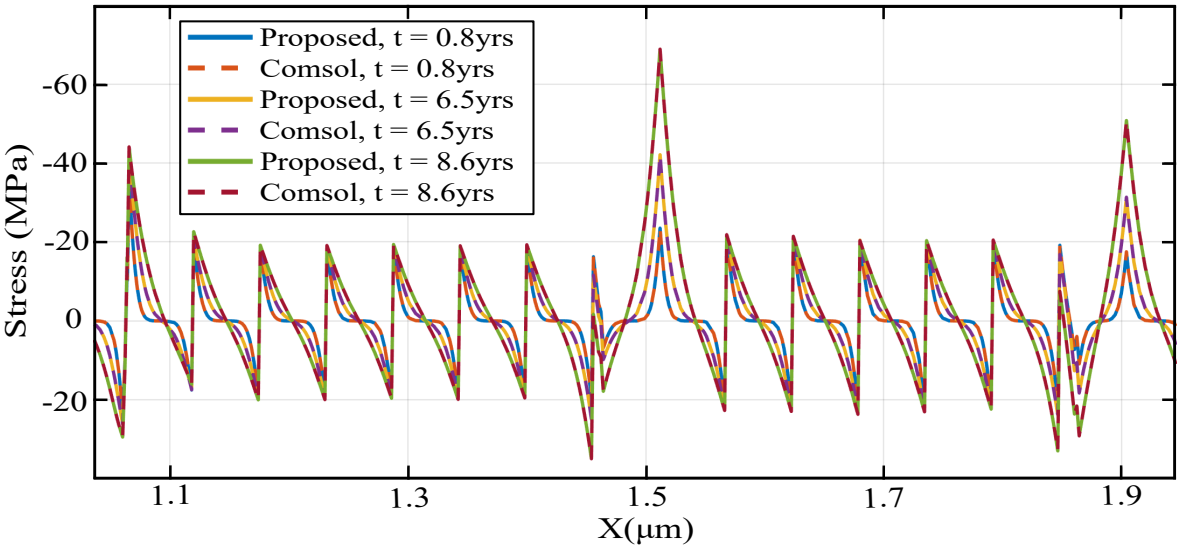
Table 3.3: Runtime and accuracy comparison between the proposed method and COMSOL, as well as Newton-Raphson convergence results, are presented for large-scale OpenROAD power grids during the nucleation phase.

Tech.	Design	Largest tree in length				Newton Rapshon		Runtime			Accuracy
		#Segments	Discr. step (μm)	Initial size	Reduced size	Time (seconds)	#Iter.	Proposed method (seconds)	COMSOL (seconds)	Speed-up	Relative error
45 nm	dynamic	229	6.00	66226	134	1.30	20	0.284	84.11	296.12×	0.027%
	ibex	320	6.00	92787	264	3.88	48	0.371	167.67	452.49×	0.492%
	aes	243	6.00	66224	146	1.52	21	0.322	111.77	347.22×	0.290%
	jpeg	550	6.00	159888	334	3.13	21	0.626	273.87	437.50×	0.470%
	swerv	597	6.00	173401	372	3.64	22	0.683	322.18	471.90×	0.788%
28 nm	gcd	21	0.92	893	28	0.01	6	0.004	2.76	681.75×	0.060%
	aes	611	2.60	248861	530	5.22	20	1.161	69.86	60.19×	0.025%
	jpeg	1228	2.60	519274	1612	10.31	20	2.294	172.21	75.07×	0.067%
12 nm	gcd	220	5.60	28484	58	0.20	6	0.073	79.41	1084.06×	0.161%
	ibex	496	4.00	90769	218	1.81	20	0.375	351.35	936.51×	0.841%
	jpeg	979	4.00	179473	264	1.72	7	0.862	144.74	167.83×	0.806%
	dynamic	1312	0.08	1201251	3612	24.21	19	6.236	207.26	33.24×	0.292%
	aes	1360	0.08	1248726	4090	10.63	6	5.814	258.08	44.39×	1.020%

from 33× to 1084×, depending on the specific benchmark. In most cases, the FDM-based point count is significantly larger than the number of finite elements generated by COMSOL. This variation is primarily due to architectural differences across benchmarks. For instance, in the last two benchmarks (both at 12 nm), COMSOL internally generates a smaller system compared to our method, which explains the relatively lower speedup observed in these cases. Nevertheless, our approach consistently achieves a reduction percentage greater than 99%, maintaining relative error below 1%, even for the largest and most complex trees. Extending this analysis, Fig. 3.8(a) depicts a selected region of the 12 nm aes design, consisting of multiple segments. A highlighted cutline traverses all of these segments, enabling a detailed analysis of stress variation along a continuous path. Fig. 3.8(b) presents the corresponding stress profile along this cutline, comparing the proposed method with COMSOL at three time points: $t = 0.8$, 6.5, and 8.6 years. The results show a strong agreement between the two methods during the pre-void phase, with nearly identical stress values. Notably, void nucleation is observed near $x = 1.51\mu$m, where stress deviations begin to appear at later time steps.



(a)



(b)

Figure 3.8: (a) Selected region of the 12 nm aes design with a cutline crossing all segments. (b) Comparison of stress profiles along the cutline during the nucleation phase, for $t = 0.8$, 6.5, and 8.6 years.

Evaluation of growth phase metrics

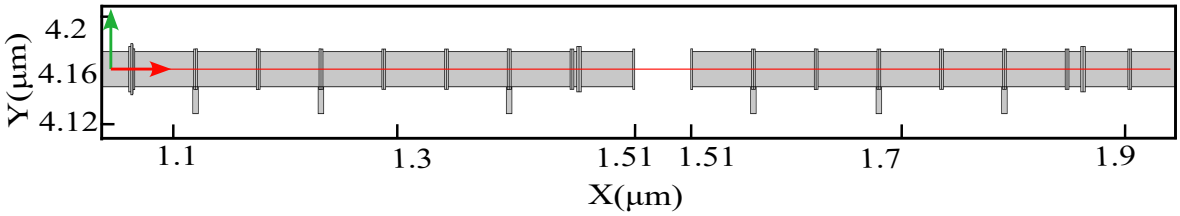
Having completed the experimental evaluation of the nucleation phase, we now turn our attention to the post-void phase. The corresponding results are summarized in Table 3.4. This table reports the number of segments in the largest subtree obtained after tree splitting at the void location, along with the spatial discretization step, the system size, and the size of the EKS. Following the structure of Table 3.3, we also provide the runtime of our proposed methodology and COMSOL at a fixed time point $t = 2$ years after void nucleation, as well as the corresponding speedup and accuracy metrics. Finally, Table 3.4 includes the results of the state-of-the-art exponential method Higham [2], which we compare against our approach. Note that Expokit [3] is omitted from this experiment due to the significantly higher relative error it produced, despite its superior speedup performance compared to Higham [2], as previously discussed. Despite the increased system size in the growth phase, the reduced EKS size remains significantly smaller, achieving over 95% reduction consistently. The runtime

Table 3.4: Runtime and accuracy comparison of the proposed method against COMSOL and Higham [2] on large-scale OpenROAD power grids during the growth phase.

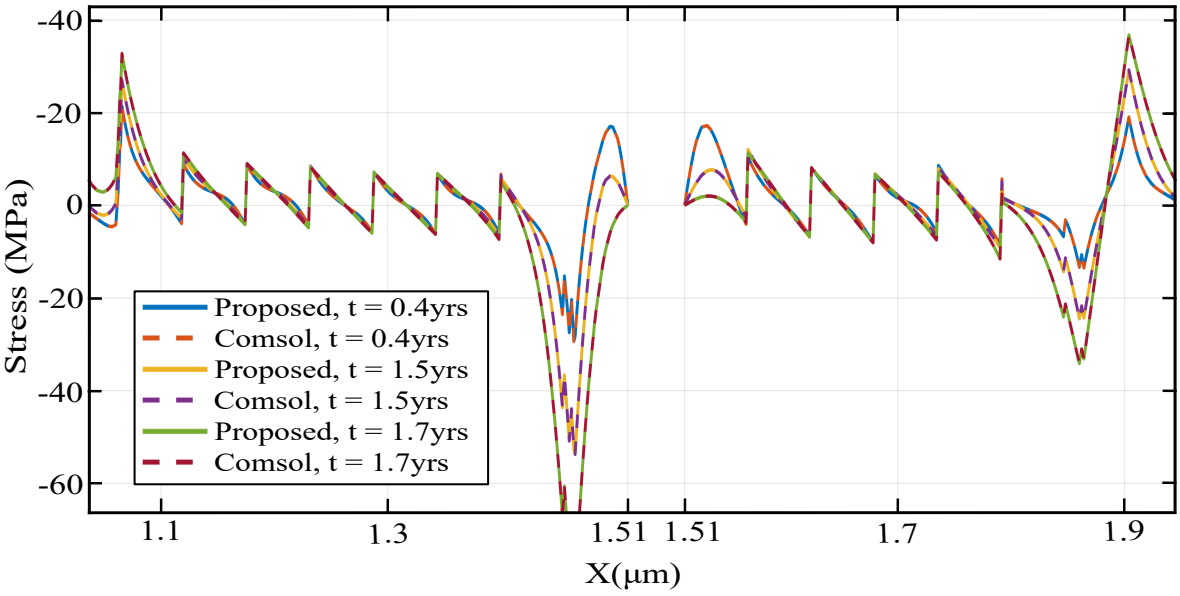
Tech.	Design	Largest tree in length				Runtimes			Speed-up		Accuracy	
		#Segments	Discr. step (μm)	Initial Size	Reduced Size	Proposed (seconds)	Higham (seconds)	Comsol (seconds)	Comsol	Higham	Proposed	Higham
45 nm	dynamic	179	6.00	52219	144	0.265	3.41	23.91	90.33×	12.88×	0.377%	0.352%
	ibex	270	6.00	78780	268	0.277	4.33	104.32	376.29×	15.62×	0.735%	0.461%
	aes	190	6.00	52217	132	0.251	3.23	69.85	278.63×	12.88×	0.667%	0.369%
	jpeg	500	6.00	145881	302	0.336	11.64	44.18	131.34×	34.59×	0.997%	0.208%
	swerv	544	6.00	158490	584	0.671	12.72	50.41	75.12×	18.95×	0.475%	0.305%
28 nm	gcd	10	0.92	467	18	0.004	0.10	2.21	493.29×	21.21×	0.800%	0.325%
	aes	473	2.60	145136	452	0.706	23.44	59.92	84.88×	33.20×	0.693%	0.006%
	jpeg	1113	2.6	451918	1652	2.453	98.57	170.85	69.64×	40.18×	0.960%	0.396%
12 nm	gcd	166	5.60	21621	72	0.067	1.45	47.87	713.37×	21.57×	0.591%	0.330%
	ibex	373	4.00	68324	158	0.348	5.57	43.66	125.44×	15.99×	0.186%	0.032%
	jpeg	824	4.00	150921	270	0.967	17.55	122.94	127.08×	18.14×	0.156%	0.087%
	dynamic	1193	0.08	1091726	3838	5.139	117.21	192.48	37.46×	22.81×	1.026%	0.056%
	aes	1306	0.08	1200496	3242	5.850	129.38	204.20	34.90×	22.12×	0.585%	0.228%

of our method continues to significantly outperform COMSOL, achieving speedups of up to 713×, and remaining at least 34× faster even in the most challenging cases. Moreover, the accuracy with respect to COMSOL remains high, with relative error consistently below 1% across all evaluated designs. Although the proposed method produces a relative error approximately 0.4% higher than that of Higham [2], the relative error remains within acceptable limit. At the same time, it is consistently faster across all benchmarks, with an average speedup of 22×. The inferior runtime performance of Higham [2] is attributed not only to the large number of terms in the Taylor series expansion, but also to the scaling and squaring step (i.e., subdivision of t), which significantly increases the number of matrix-vector multiplications. Continuing the analysis in the growth phase, Fig.3.9(a) depicts the same region of the 12 nm aes design as in Fig.3.8(a), now in the post-void state, showing the two subtrees formed after splitting at the void location near $x = 1.51, \mu$m. The same cutline is applied across both subtrees to enable a direct comparison of stress evolution after void nucleation. Fig. 3.9(b) shows the corresponding stress profiles at three time points: $t = 0.4$, 1.5, and 1.7 years, clearly demonstrating that the proposed method continues to closely match the COMSOL solution during the post-void analysis. As expected from Section 2.3, the hydrostatic

stress at the void location drops sharply toward zero due to the loss of mechanical continuity. At the same time, localized stress peaks appear near the void in both subtrees, resulting from the large stress gradient established near the void - a response accurately captured by the proposed method and validated against COMSOL across all evaluated time points.



(a)



(b)

Figure 3.9: (a) Selected region of the 12 nm aes design after tree splitting at the void location, showing both resulting subtrees. (b) Comparison of stress profiles along the cutline during the growth phase at $t = 0.4$, 1.5, and 1.7 years.

3.5.4 Evaluation of the RKS-based method

To evaluate the applicability and scalability of our RKS-based method on large-scale power grids, we applied it to the OpenROAD power grids previously introduced. Unlike the earlier evaluation in Section 3.5.3, we now focus exclusively on the trees with the largest number of segments and vias, denoted as the ”largest tree” for each benchmark. In this experiment, we performed transient EM stress analysis at $t = 20$ years using both proposed

Table 3.5: Runtime and accuracy comparison of the proposed EKS- and RKS-based methods against COMSOL on large-scale OpenROAD power grids.

Tech.	Design	Largest tree				Reduced size		Runtimes (seconds)			Speed-up (×)		Accuracy (%)	
		#Segments	#T junctions	Discr. step (μm)	Initial size	EKS	RKS	EKS	RKS	COMSOL	EKS	RKS	EKS	RKS
45 nm	dynamic	640	77	0.25	12801	5	3	0.063	0.099	12	190.47×	121.21×	0.14%	0.35%
	ibex	1096	107	0.25	21920	12	10	0.124	0.180	21	169.35×	116.67×	0.15%	0.73%
	aes	1327	82	0.25	26541	11	8	0.162	0.210	26	160.49×	123.81×	0.29%	0.45%
	jpeg	3337	184	0.25	66741	13	12	0.716	0.800	111	155.02×	138.75×	0.51%	0.53%
	swerv	5226	27	0.25	104521	17	11	1.640	1.674	254	154.87×	151.73×	0.59%	0.24%
28 nm	gcd	25	7	1	1001	6	7	0.018	0.061	4	222.22×	65.57×	0.37%	0.51%
	aes	421	159	1	16841	8	4	0.043	0.081	10	232.55×	123.46×	0.55%	0.79%
	jpeg	2285	320	1	91401	14	8	0.377	0.402	56	148.54×	139.3×	0.63%	0.54%
12 nm	gcd	276	73	0.1	5520	4	5	0.034	0.065	8	235.29×	123.08×	0.64%	0.49%
	ibex	1486	165	0.1	29721	9	6	0.184	0.232	44	239.13×	189.66×	0.53%	0.80%
	jpeg	5702	326	0.1	114041	15	11	1.936	2.713	505	260.84×	186.14×	0.54%	0.24%
	dynamic	10304	437	0.1	206081	20	12	5.860	7.430	1712	292.15×	230.42×	0.97%	0.37%
	aes	13148	453	0.1	262961	23	15	10.768	12.500	2874	266.90×	229.92×	0.82%	0.73%

EKS- and RKS—based methods compared with COMSOL as reference. The results for the largest tree of each OpenROAD benchmark are summarized in Table 3.5, where #Segments represents the total number of horizontal and vertical (via) segments per tree and #T junction describes the number of T junctions per tree. It also includes the reduced sizes produced by the EKS and RKS methods, their corresponding runtimes, the speedups achieved over COMSOL, and the relative accuracy of each approach. As shown in the table, the RKS-based method achieves a maximum relative error below 0.8%, while maintaining a reduction ratio above 99.5% and delivering an average speedup of more than 150× compared to COMSOL. This is also visualized in Fig. 3.10, which illustrates the EM stress values at selected nodes of a 28 nm aes tree, with the results from both RKS and COMSOL being nearly indistinguishable. At the same time, the EKS-based approach achieves even lower average relative errors, consistently below 1%, while maintaining an even higher average speedup of up to 252×, and similar reduction percentages above 99.5%. As expected, the RKS method exhibits faster convergence in terms of subspace size, typically requiring fewer basis vectors than EKS to reach a comparable accuracy. However, this gain in reduced size does not directly translate into runtime advantage, as each iteration of the RKS algorithm is more computationally intensive. Overall, both EKS and RKS perform well in terms of scalability and accuracy, but due to its superior

runtime performance and slightly higher robustness, EKS remains the preferred approach in our framework.

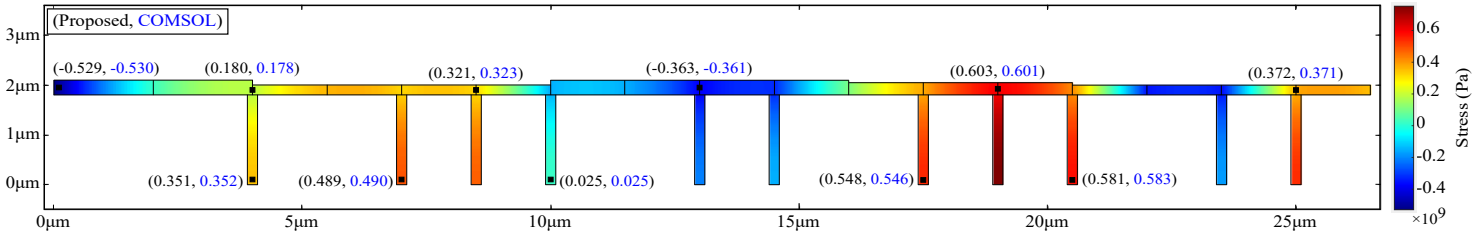


Figure 3.10: Accuracy of our RKS-based method in computing the EM stress at t = 20 years for a multi-segment tree of a 28 nm aes design.

3.6 Summary

In this chapter, we presented a comprehensive and computationally efficient framework for EM analysis, capturing both the pre- and post-void stages of stress evolution in general interconnect trees. Our framework incorporates an efficient semi-analytical solution based on the matrix exponential and provides a robust root-finding algorithm to accurately determine both the time and location of void nucleation. By leveraging the EKS, our approach efficiently approximates the matrix exponential operator, enabling fast simulation of large-scale interconnect trees. This is further enhanced by one-time subspace construction, which allows stress evaluation at arbitrary time points with minimal computational cost. Experimental results on artificial interconnect trees and OpenROAD power grids confirm that our approach is up to 1084× faster than FEM-based solver COMSOL, while retaining high accuracy with average relative error 0.5%. Compared to the state-of-the-art exponential method Higham [2], our approach achieves a speedup of up to 31×, with only a marginal accuracy loss of 0.4%. It also remains consistently faster than Expokit [3], achieving an average runtime improvement of 5× across all evaluated benchmarks. In addition, we explored the use of the RKS as an alternative means of approximating the matrix exponential. Although the RKS often required fewer basis vectors to achieve comparable accuracy, the EKS-based method consistently delivered faster runtimes due to its lower per-iteration cost. Overall, both methods demonstrated strong scalability and accuracy on large-scale power grids, with EKS emerging as the preferred choice for our EM analysis framework.

Chapter 4

EM analysis via asymmetric Krylov-based model reduction

4.1 Introduction

As mentioned in Chapter 3, numerical methods tend to be computationally prohibitive for EM analysis, particularly in large-scale interconnect structures. This is primarily because traditional physics-based EM models, after spatial discretization, lead to large-scale descriptor systems that are computationally costly for transient analysis. As a result, the application of efficient model order reduction (MOR) techniques has become essential for enabling scalable EM analysis. MOR approaches are commonly categorized into two main classes. The first class includes system-theoretic methods such as balanced truncation (BT) [38], which provide reduced-order models (ROMs) with guaranteed approximation error bounds based on Hankel singular values. However, classical BT requires the solution of computationally demanding Lyapunov matrix equations and storing full system operations that are infeasible for dense matrices, especially when preserving sparsity is critical. The second class includes moment-matching (MM) techniques, which have gained popularity due to their high computational efficiency [39]. MM-based ROMs are constructed by matching a set of moments of the original system's transfer function. However, the quality of the reduced model depends entirely on the Krylov subspace used to generate it.

The majority of MM techniques utilize the standard or rational Krylov subspace to estimate the original model. Rational Krylov methods [40, 41] offer improved convergence and preserve matrix sparsity, but they require careful selection of expansion points and do not

provide guaranteed error bounds, which can compromise accuracy or stability. On the other hand, methods [20, 39, 42] based on the standard Krylov subspace are easy to implement and effective in many applications. Nonetheless, they suffer from a high-frequency bias and insufficient resolution of low-frequency behavior, which is especially problematic in EM analysis. Taking these limitations into account, EKS has been proposed (see Chapter 3) to capture both low- and high-frequency dynamics without requiring user-defined expansion points. However, its symmetric structure leads to computational inefficiencies, particularly due to the dense linear system solves and matrix-vector operations required at each iteration, thereby limiting the scalability of this subspace for large-scale EM systems.

In this chapter, we propose a MM numerical method based on the asymmetric extended Krylov subspace (AEKS) for efficient EM stress analysis in general interconnect structures. The main contributions of this chapter are summarized as follows. *Firstly*, our method leverages the AEKS, a sparsity-aware projection strategy that adaptively enriches the subspace in the direction of the sparser matrix. This enables the proposed approach to retain the approximation quality of EKS while significantly reducing the computational overhead, making it an efficient and scalable approach for EM stress evaluation in large-scale models. *Secondly*, we introduce a parallelization strategy for computing the reduced-order response of large-scale EM systems, enabling scalable Krylov subspace construction and transfer function evaluation with reuse of sparse matrix factorizations. Finally, the proposed method has been comprehensively validated across frequency-domain and transient EM simulations using large-scale industrial power grid benchmarks. In frequency-domain evaluations, our method consistently outperforms conventional MM approaches, closely matching the original model across the spectrum. In transient EM analysis, it achieves high accuracy results, maintaining relative errors below 0.5% compared to COMSOL. Moreover, it delivers substantial runtime improvements of up to $15\times$ over original model simulations and $100\times$ over COMSOL, while demonstrating robustness under time-varying current density inputs.

The rest of the chapter is organized as follows. Section 4.2 provides the theoretical background of MOR for EM analysis, focusing on the use of MM techniques to reduce the size of descriptor systems derived from interconnect structures. Section 4.3 analyzes the limitations of standard MM and EKS methods in the context of large-scale EM models. Sections 4.4, 4.5 introduce our main contributions, including the proposed AEKS method, and the parallel Krylov reduction for EM systems. Section 4.6 presents a comprehensive experimental eval-

uation of the proposed method using IBM benchmarks, with final conclusions summarized in Section 4.7.

4.2 Background of MOR by MM

As described in Section 3.2, for a general m multi-segment interconnect tree discretized into n points, the resulting LTI system after applying singularity elimination via Algorithm 1 can be formulated as:

$$\begin{aligned} \mathbf{C}\dot{\sigma}(t) &= \mathbf{G}\sigma(t) + \mathbf{B}\mathbf{j}(t), \\ \mathbf{y}(t) &= \mathbf{L}\sigma(t) \end{aligned} \tag{4.1}$$

where $\mathbf{G} \in \mathbb{R}^{(n-1)\times(n-1)}$ is stress diffusion matrix, $\mathbf{C} \in \mathbb{R}^{(n-1)\times(n-1)}$ is a diagonal matrix, $\boldsymbol{\sigma}(t) \in \mathbb{R}^{n-1}$ denotes the vector of unknown stress values at all discretization points (constituting internal states of the system), $\mathbf{j}(t) \in \mathbb{R}^p$ represents the vector of input excitations from the current densities, $\mathbf{B} \in \mathbb{R}^{(n-1)\times p}$ is the input-to-state connectivity matrix, $\mathbf{L} \in \mathbb{R}^{p\times(n-1)}$ is the state-to-output connectivity matrix, and $\mathbf{y}(t) \in \mathbb{R}^q$ is the output vector representing the observed stress values. Moreover, by denoting the model *order* as $N \equiv n-1$, Eq. (4.1) can be interpreted as a generalized state-space representation, commonly referred to as the *descriptor form*.

The objective of MOR is to produce a reduced order model:

$$\begin{aligned} \tilde{\mathbf{C}}\frac{d\tilde{\sigma}(t)}{dt} &= \tilde{\mathbf{G}}\tilde{\sigma}(t) + \tilde{\mathbf{B}}\mathbf{j}(\mathbf{t}), \\ \tilde{\mathbf{y}}(t) &= \tilde{\mathbf{L}}\tilde{\sigma}(t) \end{aligned} \tag{4.2}$$

with $\tilde{\mathbf{G}}, \tilde{\mathbf{C}} \in \mathbb{R}^{r\times r}$, $\tilde{\mathbf{B}} \in \mathbb{R}^{r\times p}$, $\tilde{\mathbf{L}} \in \mathbb{R}^{q\times r}$, where the order of the reduced model is $r << N$ and the output error $||\tilde{\mathbf{y}}(t) - \mathbf{y}(t)||_2$ is small. An equivalent metric of accuracy in the frequency domain (via Plancherel's theorem [43]) is the distance $||\tilde{\mathbf{H}}(s) - \mathbf{H}(s)||_\infty$, where

$$\begin{aligned} \mathbf{H}(s) &= \mathbf{L}(s\mathbf{C} - \mathbf{G})^{-1}\mathbf{B} \\ \tilde{\mathbf{H}}(s) &= \tilde{\mathbf{L}}(s\tilde{\mathbf{C}} - \tilde{\mathbf{G}})^{-1}\tilde{\mathbf{B}} \end{aligned} \tag{4.3}$$

are the transfer functions of the original and the ROM, and $||.||_\infty$ is the induced $\mathcal{L}_2$ matrix norm (or the $\mathcal{H}_\infty$ norm of a rational transfer function).

The most important and successful MOR methods for linear systems are based on MM. They are very efficient in circuit simulation problems and are formulated in a way that has a direct application to the linear model of (4.1).

By applying the Laplace transform to (4.1), we obtain the s domain equations as:

$$\begin{aligned} s\mathbf{C}\sigma(s) - \mathbf{x}(0) &= \mathbf{G}\sigma(s) + \mathbf{B}\mathbf{u}(s) \\ \mathbf{y}(s) &= \mathbf{L}\sigma(s) \end{aligned} \tag{4.4}$$

Assuming that $\sigma(0) = 0$ and that a unit impulse excitation is applied (i.e., $\mathbf{u}(s) = 1$), the system's impulse response can be extracted. This assumption is standard in moment-matching MOR and serves as a mathematical simplification to derive the moments of the transfer function, rather than a physical input used in simulation. Accordingly, the system can be written as:

$$\begin{aligned} (s\mathbf{C} - \mathbf{G})\sigma(s) &= \mathbf{B} \\ \mathbf{y}(s) &= \mathbf{L}\sigma(s) \end{aligned} \tag{4.5}$$

and by expanding the Taylor series of $\mathbf{x}(s)$ around zero, we derive the following equation:

$$(s\mathbf{C} - \mathbf{G})(\mathbf{x}_0 + \mathbf{x}_1 s + \mathbf{x}_2 s^2 + \dots) = \mathbf{B} \tag{4.6}$$

The transfer function of (4.1) is a function of s, and can be expanded into a moment expansion around $s = 0$ as follows:

$$\mathbf{H}(s) = \mathbf{M}_0 + \mathbf{M}_1 s + \mathbf{M}_2 s^2 + \mathbf{M}_3 s^3 \dots \tag{4.7}$$

where $\mathbf{M}_0$, $\mathbf{M}_1$, $\mathbf{M}_2$, $\mathbf{M}_3$, $\dots$ are the moments of the transfer function. In general, $\mathbf{M}_0$ corresponds to the steady-state (DC) solution of the underlying linear system. It represents the system response under constant input conditions, where all dynamic effects are neglected. Depending on the physical context, this may correspond to the zero-frequency response, the static stress distribution, or the equilibrium state of the system.

Moreover, $\mathbf{M}_1$ represents the first-order dynamic behavior of the system around steady-state conditions. In physical terms, it captures the main time constant controlling how the system responds dynamically to external inputs. In general, $\mathbf{M}_i$ is related to the system matrices as:

$$\mathbf{M}_i = \mathbf{L}(\mathbf{G}^{-1}\mathbf{C})^i \mathbf{G}^{-1}\mathbf{B} \tag{4.8}$$

The goal of MM reduction techniques is the derivation of a ROM where some moments $\tilde{\mathbf{M}}_i$ of the reduced-order transfer function $\tilde{\mathbf{H}}(s)$ match some moments of the original transfer function $\mathbf{H}(s)$.

Let us now denote the two projection matrices onto a lower dimensional subspace as $\mathbf{V}_\ell, \mathbf{V}_r \in \mathbb{R}^{N\times r}$. These matrices can be derived from the associated moments using one or

more expansion points. As a result, if we assume that $s = 0$, then the matrices $\mathbf{V}_\ell$ and $\mathbf{V}_r$ are defined as follows:

$$range(\mathbf{V}_r) = span\{\mathbf{G}^{-1}\mathbf{B}, (\mathbf{G}^{-1}\mathbf{C})\mathbf{G}^{-1}\mathbf{B}, \ldots,$$

$$(\mathbf{G}^{-1}\mathbf{C})^{r-1}\mathbf{G}^{-1}\mathbf{B}\}$$

$$range(\mathbf{V}_\ell) = span\{\mathbf{L}^T, (\mathbf{C}^T\mathbf{G}^{-T})\mathbf{L}^T, \ldots, (\mathbf{C}^T\mathbf{G}^{-T})^{r-1}\mathbf{L}^T\} \tag{4.9}$$

The computed ROM matches the first $2r$ moments and is obtained by the following matrices:

$$\tilde{\mathbf{C}} = \mathbf{V}_\ell^T\mathbf{C}\mathbf{V}_r, \quad \tilde{\mathbf{G}} = \mathbf{V}_\ell^T\mathbf{G}\mathbf{V}_r, \quad \tilde{\mathbf{B}} = \mathbf{V}_\ell^T\mathbf{B}, \quad \tilde{\mathbf{L}} = \mathbf{L}\mathbf{V}_r \tag{4.10}$$

This reduced model provides a good approximation around the DC point. Finally, in case we employ a one-sided Krylov method, which is usually the case, the matrix $\mathbf{V}_\ell$ can be set equal to $\mathbf{V}_r$, an equality that also holds for symmetric systems.

4.3 Specification of EKS and its application to MM

The essence of MM methods is to iteratively compute a projection subspace, and then project the original system into this subspace in order to obtain the ROM of (4.2). The dimension of the projection subspace is increased in every iteration, until an "a priori" selection of the moments is matched. More specifically, if r is the desired order for the reduced system and $k = \frac{r}{p}$ is the number of moments (where p denotes the total number of input/output ports), then $\mathbf{V} \in \mathbb{R}^{N\times r}$ is a projection matrix whose columns span the r-dimensional Krylov subspace:

$$\mathcal{K}_r(\mathbf{A}_E, \mathbf{B}_E) = span\{\mathbf{B}_E, \mathbf{A}_E\mathbf{B}_E, \mathbf{A}_E^2\mathbf{B}_E, \ldots, \mathbf{A}_E^{r-1}\mathbf{B}_E\} \tag{4.11}$$

where

$$\mathbf{A}_E \equiv \mathbf{G}^{-1}\mathbf{C}, \quad \mathbf{B}_E \equiv \mathbf{G}^{-1}\mathbf{B} \tag{4.12}$$

Then, the ROM is obtained through the following matrix transformations:

$$\tilde{\mathbf{C}} = \mathbf{V}^T\mathbf{C}\mathbf{V}, \quad \tilde{\mathbf{G}} = \mathbf{V}^T\mathbf{G}\mathbf{V}, \quad \tilde{\mathbf{B}} = \mathbf{V}^T\mathbf{B}, \quad \tilde{\mathbf{L}} = \mathbf{L}\mathbf{V} \tag{4.13}$$

with $\tilde{\mathbf{G}}, \tilde{\mathbf{C}} \in \mathbb{R}^{r\times r}$, $\tilde{\mathbf{B}} \in \mathbb{R}^{r\times p}$, $\tilde{\mathbf{L}} \in \mathbb{R}^{q\times r}$. Although efficient, this construction captures high-frequency dynamics, which is less effective in applications such as EM stress analysis, where long-term stress evolution is governed by low-frequency behavior.

The effectiveness of the projection process can be improved by expanding around more points than $s = 0$, leading to rational Krylov subspaces with targeted expansion points [40, 41]. However, the selection of expansion points is nontrivial and problem-dependent. To avoid this ambiguity, we consider the EKS, which combines both standard and inverse Krylov subspaces, thereby expanding the subspace around both $s = 0$ and $s = \infty$. Formally, the EKS is defined as:

$$\mathcal{K}_r^E(\mathbf{A}_E, \mathbf{B}_E) = \mathcal{K}_{r/2}(\mathbf{A}_E, \mathbf{B}_E) + \mathcal{K}_{r/2}(\mathbf{A}_E^{-1}, \mathbf{B}_E) =$$

$$span\{\mathbf{B}_E, \mathbf{A}_E^{-1}\mathbf{B}_E, \mathbf{A}_E\mathbf{B}_E, \mathbf{A}_E^{-2}\mathbf{B}_E, \mathbf{A}_E^{2}\mathbf{B}_E, \mathbf{A}_E^{-3}\mathbf{B}_E, \ldots,$$

$$\mathbf{A}_E^{(r/2)-1}\mathbf{B}_E, \mathbf{A}_E^{-r/2}\mathbf{B}_E\} \tag{4.14}$$

This construction achieves spectral enrichment across a broad frequency range without requiring the manual selection of expansion points. It has been successfully applied in matrix function approximation [44], Lyapunov and Sylvester equation solvers [45, 46], demonstrating significant improvements in the performance of Krylov-subspace methods. Unlike weighted approaches such as [47], EKS avoids ambiguity in the choice of expansion points. Also, an earlier version of this subspace was presented at [48].

In Chapter 3, we applied the EKS framework in the context of EM analysis to reduce the computational cost of matrix exponential evaluations during time-domain stress simulations. This earlier application demonstrated the capability of EKS to capture slow dynamics and long-term stress evolution with improved numerical stability. Nevertheless, the symmetric expansion of EKS requires both forward and inverse matrix operations at every iteration, which becomes computationally expensive in large-scale EM systems characterized by structurally unbalanced matrices (e.g., one sparse and one dense).

4.4 Proposed asymmetric Krylov-based method

To address the limitation of symmetric subspace construction in traditional EKS methods, we propose the AEKS as an efficient and scalable MOR strategy tailored for EM stress analysis in large-scale interconnect structures. Unlike EKS, which symmetrically alternates between forward and inverse matrix operations, AEKS introduces a sparsity-aware expansion strategy that prioritizes computational efficiency without compromising spectral enrichment. In practical implementations, the inputs to construct the EKS are not actually the matrices $\mathbf{A}_E = \mathbf{G}^{-1}\mathbf{C}$ and $\mathbf{B}_E = \mathbf{G}^{-1}\mathbf{B}$ but the original system matrices $\mathbf{G}$ and $\mathbf{C}$ which are very

sparse in typical EM problems. This is because the generally dense inverse matrices $\mathbf{G}^{-1}$ and $\mathbf{C}^{-1}$ are only needed for matrix-vector products during basis construction. These products can be implemented as sparse linear solves ($\mathbf{CY} = \mathbf{R}$ and $\mathbf{GY} = \mathbf{R}$) by employing any sparse direct [49] or iterative [50] algorithm. However, in typical EM problems that one of the matrices $\mathbf{G}$ or $\mathbf{C}$ is considerably sparser than the other. In that case, the solves with $\mathbf{C}$ are much more efficient than the solves with $\mathbf{G}$, and it can be very computationally beneficial to deviate from symmetry in the construction of the EKS (4.14).

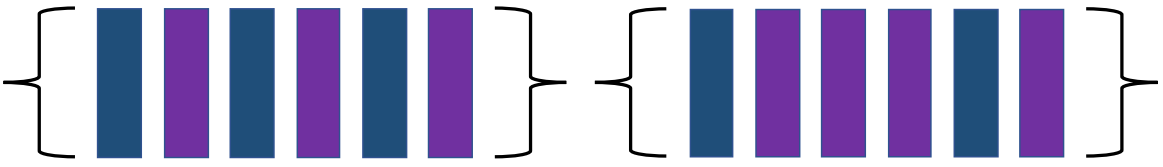
Following this principle, our method begins by computing the sparsity (i.e., number of nonzeros) of the matrices $\mathbf{G}$ and $\mathbf{C}$, expands predominantly in the direction ($\mathbf{A}_E$ or $\mathbf{A}_E^{-1}$) that will generate more sparse solves, by adding one moment block corresponding to the denser solve for every m moment blocks of the sparser solve. For example, in the usual case where $\mathbf{C}$ is sparser than $\mathbf{G}$, and for $m = 3$, the proposed AEKS method will generate one moment block of $\mathbf{A}_E = \mathbf{G}^{-1}\mathbf{C}$ after 3 moment blocks of $\mathbf{A}_E^{-1} = \mathbf{C}^{-1}\mathbf{G}$, and will create the following r-dimensional subspace:

$$\mathcal{K}_r^{AE}(\mathbf{A}_E, \mathbf{B}_E) = \mathcal{K}_{r/4}(\mathbf{A}_E, \mathbf{B}_E) + \mathcal{K}_{3r/4}(\mathbf{A}_E^{-1}, \mathbf{B}_E) =$$

$$span\{\mathbf{B}_E, \mathbf{A}_E^{-1}\mathbf{B}_E, \mathbf{A}_E^{-2}\mathbf{B}_E, \mathbf{A}_E^{-3}\mathbf{B}_E, \mathbf{A}_E\mathbf{B}_E, \mathbf{A}_E^{-4}\mathbf{B}_E, \ldots,$$

$$\mathbf{A}_E^{(r/4)-1}\mathbf{B}_E, \mathbf{A}_E^{-(3r/4-2)}\mathbf{B}_E, \mathbf{A}_E^{-(3r/4-1)}\mathbf{B}_E, \mathbf{A}_E^{-3r/4}\mathbf{B}_E\} \tag{4.15}$$

The AEKS procedure is shown visually in Fig. 4.1 (compared with the symmetric EKS), and its computation is given in Algorithm 6.



(a) (b)

Figure 4.1: Visual representation of (a) the EKS sequence, (b) the AEKS sequence. Blue and purple blocks correspond to powers of matrices $\mathbf{A}_E$ and $\mathbf{A}_E^{-1}$, respectively.

In steps 1–7, the algorithm begins by checking whether the number of non-zero entries in matrix $\mathbf{C}$ is smaller than that in matrix $\mathbf{G}$. Based on this, it constructs the initial orthonormal basis and sets the appropriate dense and sparse matrix operators accordingly. During each iteration (steps 9–19), the algorithm applies the appropriate operator (either `Dense_Op` or

Algorithm 6: AEKS construction method via MM

Input: $\mathbf{A}_E \equiv \mathbf{G}^{-1}\mathbf{C}, \mathbf{B}_E \equiv \mathbf{G}^{-1}\mathbf{B}$, desired order r, #ports p, modulo m

Output: Projection matrix $\mathbf{V}$

if $nnz(\mathbf{C}) < nnz(\mathbf{G})$ **then**
  $\mathbf{V}^{(j)} \leftarrow \text{qr}([\mathbf{B}_E, \mathbf{A}_E^{-1}\mathbf{B}_E])$
  `Dense_Op` $\leftarrow \mathbf{A}_E^{-1}$; `Sparse_Op` $\leftarrow \mathbf{A}_E$
else
  $\mathbf{V}^{(j)} \leftarrow \text{qr}([\mathbf{A}_E^{-1}\mathbf{B}_E, \mathbf{B}_E])$
  `Dense_Op` $\leftarrow \mathbf{A}_E$; `Sparse_Op` $\leftarrow \mathbf{A}_E^{-1}$
end
$k \leftarrow \lceil r/((m+1)\cdot p) \rceil$
for $j = 1, \ldots, k$ **do**
  if $j \bmod m = 0$ **then**
    $\mathbf{V}_1 \leftarrow$ `Dense_Op` applied to the $(j-m)^{\text{th}}$ block from the end of $\mathbf{V}^{(j)}$
  else
    $\mathbf{V}_1 \leftarrow$ `Sparse_Op` applied to the last block of $\mathbf{V}^{(j)}$
  end
  $\mathbf{V}_2 = \texttt{orth}(\mathbf{V}_1, \mathbf{V}^{(j)}, p)$
  $\mathbf{V}_3 \leftarrow \text{qr}(\mathbf{V}_2)$
  $\mathbf{V}^{(j+1)} \leftarrow [\mathbf{V}^{(j)}, \mathbf{V}_3]$
  $j \leftarrow j + 1$
end
$\mathbf{V} \leftarrow \mathbf{V}^{(j)}(:, 1:r)$;

Algorithm 7: Orthogonalization w.r.t. another matrix

Input: $\mathbf{V}_1, \mathbf{V}^{(j)}$, #ports p

Output: $\mathbf{V}_2$

Function `orth` $(\mathbf{V}_1, \mathbf{V}^{(j)}, p)$ **:**
  for $k_1 = 1, \ldots, j$ **do**
    $k_2 = 2p(k_1 - 1), k_3 = 2pk_1$
    $\mathbf{V}_2 = \mathbf{V}_1 - \mathbf{V}^{(j)}(:, k_2+1:k_3)\mathbf{V}^{(j)T}(:, k_2+1:k_3)\mathbf{V}_1$
  end
  return $\mathbf{V}_2$
End Function

`Sparse_Op`) to compute a new candidate block vector V_1, orthogonalizes it against the existing basis vectors using Algorithm 7 (step 15) [51], normalizes it through QR factorization, and then appends the result to the evolving subspace (step 17). Finally, in step 20, the basis is truncated to the desired reduced order r.

4.5 Efficient computation of the reduced-order response and transfer function

To efficiently compute the transfer function and the output response of a multi-input multi-output (MIMO) descriptor model like (4.1), we can consider the following single-input multi-output (SIMO) subsystems:

$$\begin{aligned} \mathbf{C}\frac{d\sigma(t)}{dt} &= \mathbf{G}\sigma(t) + \mathbf{b}_i u_i(t), \\ \mathbf{y}_i(t) &= \mathbf{L}\sigma(t) \end{aligned} \tag{4.16}$$

where $\mathbf{b}_i$ is the i-th column of matrix $\mathbf{B}$, and $u_i(t)$ is the i-th input ($i = 1, \ldots, p$). From these SIMO subsystems, the output of the MIMO descriptor system is $\mathbf{y}(s) = \sum_{n=1}^{p} \mathbf{y}_i(s) = \sum_{n=1}^{p} \mathbf{h}_i(s)u_i(s)$, where

$$\mathbf{h}_i(s) = \mathbf{L}(s\mathbf{C} - \mathbf{G})^{-1}\mathbf{b}_i$$

This effectively represents the superposition property of linear and time-invariant (LTI) systems.

The above decomposition can be employed for the parallel computation of the reduced-order MIMO transfer function. In particular, for each SIMO subsystem of (4.16), a projection matrix $\mathbf{V}_i \in \mathbb{R}^{N\times r}$ can be computed, whose columns span the r-dimensional EKS (or AEKS):

$$\begin{aligned} \mathcal{K}_r^E(\mathbf{A}_E, \mathbf{b}_i^E) = \mathcal{K}_{r/2}(\mathbf{A}_E, \mathbf{b}_i^E) + \mathcal{K}_{r/2}(\mathbf{A}_E^{-1}, \mathbf{b}_i^E) = \\ span\{\mathbf{b}_i^E, \mathbf{A}_E^{-1}\mathbf{b}_i^E, \mathbf{A}_E\mathbf{b}_i^E, \mathbf{A}_E^{-2}\mathbf{b}_i^E, \mathbf{A}_E^2\mathbf{b}_i^E, \mathbf{A}_E^{-3}\mathbf{b}_i^E, \ldots, \\ \mathbf{A}_E^{(r/2)-1}\mathbf{b}_i^E, \mathbf{A}_E^{-r/2}\mathbf{b}_i^E\} \end{aligned} \tag{4.17}$$

where $\mathbf{b}_i^E \equiv \mathbf{A}^{-1}\mathbf{b}_i$. The computation of the projection matrices (by Algorithm 6) is independent from one another and can be performed in parallel. The reduced-order SISO subsystems can then be computed in parallel as:

$$\tilde{\mathbf{E}}_i = \mathbf{V}_i^T\mathbf{E}\mathbf{V}_i, \quad \tilde{\mathbf{A}}_i = \mathbf{V}_i^T\mathbf{A}\mathbf{V}_i, \quad \tilde{\mathbf{b}}_i = \mathbf{V}_i^T\mathbf{b}_i, \quad \tilde{\mathbf{L}}_i = \mathbf{L}\mathbf{V}_i \tag{4.18}$$

The i-th column of the MIMO reduced-order transfer function would then be:

$$\tilde{\mathbf{h}}_i(s) = \tilde{\mathbf{L}}_i(s\tilde{\mathbf{C}}_i - \tilde{\mathbf{G}}_i)^{-1}\tilde{\mathbf{b}}_i + \mathbf{d}_i \tag{4.19}$$

and the whole MIMO ROM transfer function can be derived as the concatenation:

$$\tilde{\mathbf{H}}(s) = [\tilde{\mathbf{h}}_1(s); \tilde{\mathbf{h}}_2(s); \ldots; \tilde{\mathbf{h}}_p(s)] \tag{4.20}$$

It must be noted that this decomposition it is better combined with direct solvers, since the computation of the Krylov subspace requires sparse solves with $\mathbf{G}$ and $\mathbf{C}$ as we mentioned previously. Using direct solvers, one can pre-compute the proper decomposition of the above matrices and then re-use them in each parallel computation.

4.6 Experimental results

In this section, we provide a detailed experimental evaluation of the proposed Asymmetric EKS-MM methodology. The experiments are organized into three parts. First, we investigate the numerical performance and quality of AEKS-MM against conventional Krylov subspace approaches, including MM and EKS-MM methods. Our evaluation focuses on large-scale industrial power grids, examining the accuracy, computational efficiency, and frequency domain behavior of the generated ROMs. Second, our approach is compared to COMSOL v5.5, a FEM-based solver, for an artificial multi-segment interconnect tree. Finally, we perform EM stress analysis on representative large-scale power grids to further evaluate the applicability of our proposed method. For time-domain simulations, an implicit Backward Euler (BE) method was employed for solving the ROMs derived from AEKS-MM. All power grid structures analyzed in this work are assumed to be made of Cu DD interconnects. This assumption allows each layer and interconnect structure to be analyzed independently under the local stress models. The proposed AEKS-MM methodology was developed using MATLAB R2021a, utilizing its built-in numerical toolset for matrix operations, linear solves, and sparse matrix handling. All experiments were conducted on a high-performance Windows system equipped with a 4.7 GHz Intel Core i9-9900k CPU, 32 GB RAM, and 16 threads, ensuring robust computational capacity for large-scale transient simulations.

Prior to the full experimental evaluation, we conducted a sensitivity study to determine the optimal choice of the modulo parameter m in Algorithm 6, balancing reduction time and accuracy. Four industrial benchmarks were selected, each featuring approximately 1.6

million discretization points and 900 interconnect segments on average, covering a wide range of sparsity ratios $\gamma = \text{nnz}(C)/\text{nnz}(G)$, with $\gamma \in [0.2, 0.6]$, representative of all IBM cases. Fig. 4.2 shows the impact of varying $m \in [1, 6]$ on the relative error of the transfer function and the corresponding reduction time across the four benchmarks. For low sparsity ($\gamma = 0.21$), the best trade-off is achieved with $m = 2$, while for moderate sparsity ($\gamma = 0.33, 0.42$), $m = 3$ performs best. In cases of higher sparsity ($\gamma = 0.56$), $m = 4$ provides improved accuracy at reasonable cost. These trends provide practical guidance for selecting the parameter m according to the sparsity pattern of the problem.

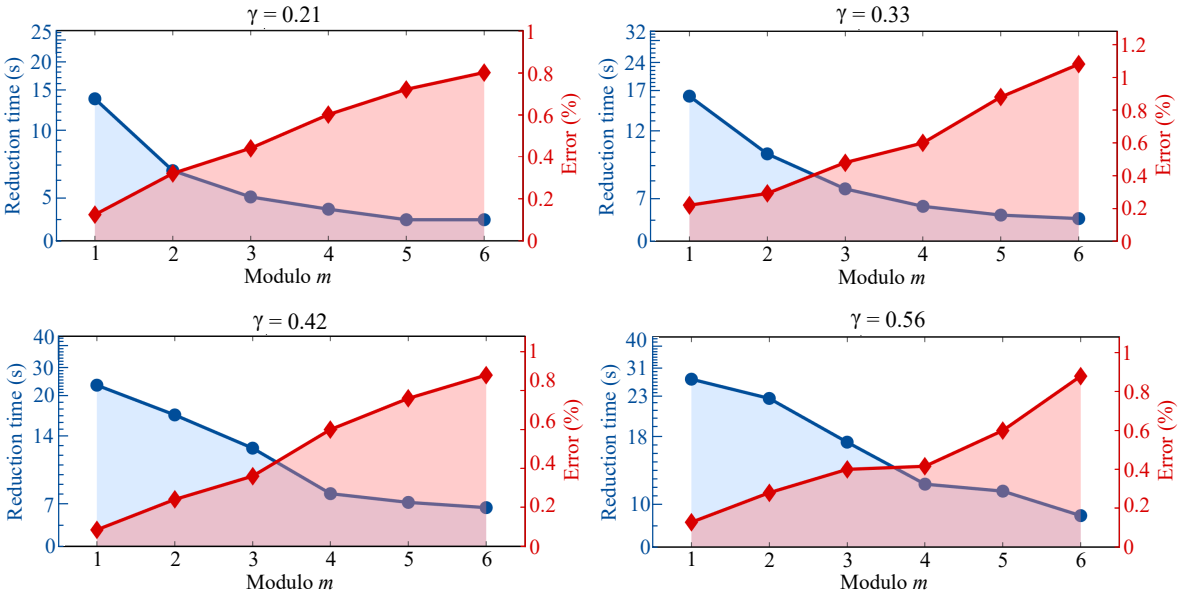


Figure 4.2: Modulo m parameter selection for optimal trade-off across four industrial benchmarks with varying sparsity ratios γ.

4.6.1 Accuracy and performance evaluation of ROMs

For the experimental evaluation of the proposed methodology, we used the available IBM power grid benchmarks [52]. Each power grid structure was processed using a BFS algorithm to extract representative multi-segment interconnect lines suitable for EM stress analysis. To compute the DC steady-state currents required for EM stress analysis, we performed DC simulations using the circuit simulator tool, Ngspice [53]. From each benchmark, we selected the interconnect line containing the highest number of discretization points, as these represent the most challenging cases for transient EM stress evolution. The corresponding ODE systems derived from the discretization were subsequently used to construct ROMs

based on the different krylov subspace methods evaluated. EKS-MM and AEKS-MM were implemented following the procedures described in Sections 4.3 and 4.5, respectively, and were compared against a standard MM method using the superposition property. For a fair comparison, an appropriate number of matching moments was selected so that the resulting ROM orders were identical across EKS-MM, AEKS-MM, and MM.

Table 4.1: Results of EKS-MM and AEKS-MM vs MM for industrial IBM power grids

Bench.	Order	#ports	ROM Order	MM		EKS-MM			**AEKS-MM**		
				Max Error	Time (s)	Max Error	Error Red. (%)	Time (s)	Max Error	Error Red. (%)	Time (s)
ibmpg1	52695	269	538	1.194	0.717	0.014	38.57	0.917	0.451	17.54	0.164
ibmpg2	115765	192	384	0.443	0.511	0.057	74.38	0.841	0.128	66.68	0.255
ibmpg3	381211	383	1532	0.276	4.759	0.161	36.98	6.492	0.162	24.83	1.254
ibmpg4	631361	487	1948	0.916	10.614	0.066	75.86	11.648	0.774	53.84	1.634
ibmpg5	866481	538	2152	1.026	14.223	0.149	80.12	16.721	0.563	62.14	2.264
ibmpg6	1694769	966	2898	1.182	20.958	0.726	68.46	27.608	0.976	43.18	4.643
ibmpg7	2260831	563	2815	1.747	37.488	0.363	54.01	40.965	0.775	41.85	6.190
ibmpg8	3229510	580	3480	0.464	59.590	0.087	40.16	66.272	0.146	19.64	10.593

Our results are reported in the remaining columns of Table 4.1. The characteristics of the selected lines are shown in the first two columns of table, where *Order* refers to the number of discretization nodes, and *#ports* indicates the total number of junctions and end-points present in the interconnect line. Also, *ROM Order* refers to the size of $\mathbf{A}$ and $\mathbf{E}$ ROM matrices, *Max Error* refers to the error between the infinity norms of the transfer functions, i.e., $||\tilde{\mathbf{H}}(s) - \mathbf{H}(s)||_\infty = \texttt{max}_{s\in[10^0,\,10^{12}]}|\widetilde{\mathbf{H}}(s) - \mathbf{H}(s)|$, *Time* refers to the computational time (in seconds) needed to generate each submatrix $\mathbf{h}_i(s)$ of (4.20), while *Error Red.* refers to the error reduction percentage achieved by EKS-MM and AEKS-MM over MM. It can be clearly verified that, compared to MM for similar ROM order, EKS-MM and AEKS-MM produce ROMs with significantly smaller error. As depicted in Table 4.1, the *Error Red.* ranges from 36.98% to 80.12% for EKS-MM, while for AEKS-MM ranges from 19.64% to 66.68%. The differences in error reduction percentages across benchmarks stem primarily from structural and topological variations among the selected interconnects, such as length, number of segments, and current densities. Additionally, the observed error reduction depends on the specific port locations used to define the transfer function, since the frequency

content and dynamic behavior of the response can vary significantly between ports. These combined effects explain the variations in error reduction percentages across benchmarks. The execution time of EKS-MM is negligibly larger than standard MM for each moment computation, due to the expansion in two points, however, the efficient implementation can effectively mask this overhead to a substantial extent and make the procedure applicable to large-scale interconnect lines. On the other hand, AEKS-MM leverages the sparse solve operation to dramatically reduce the overall runtime, while maintaining an acceptable error margin compared to EKS-MM, with a maximum error difference of only 0.4. More specifically, AEKS-MM achieves significant average runtime speedups of up to $7\times$ over EKS-MM and $6\times$ over MM.

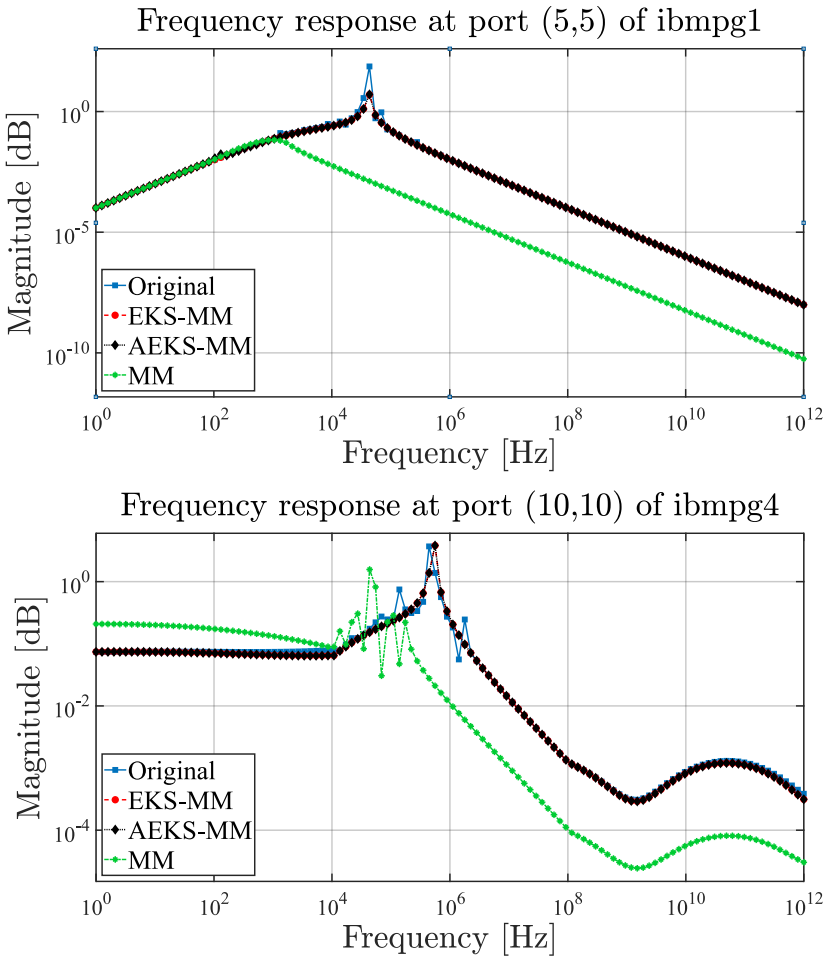


Figure 4.3: Comparison of transfer functions of ROMs obtained by EKS-MM, AEKS-MM, and MM in the frequency range $[10^0, 10^{12}]$ for ibmpg1 and ibmpg4 benchmarks at ports (5,5) and (10,10), respectively.

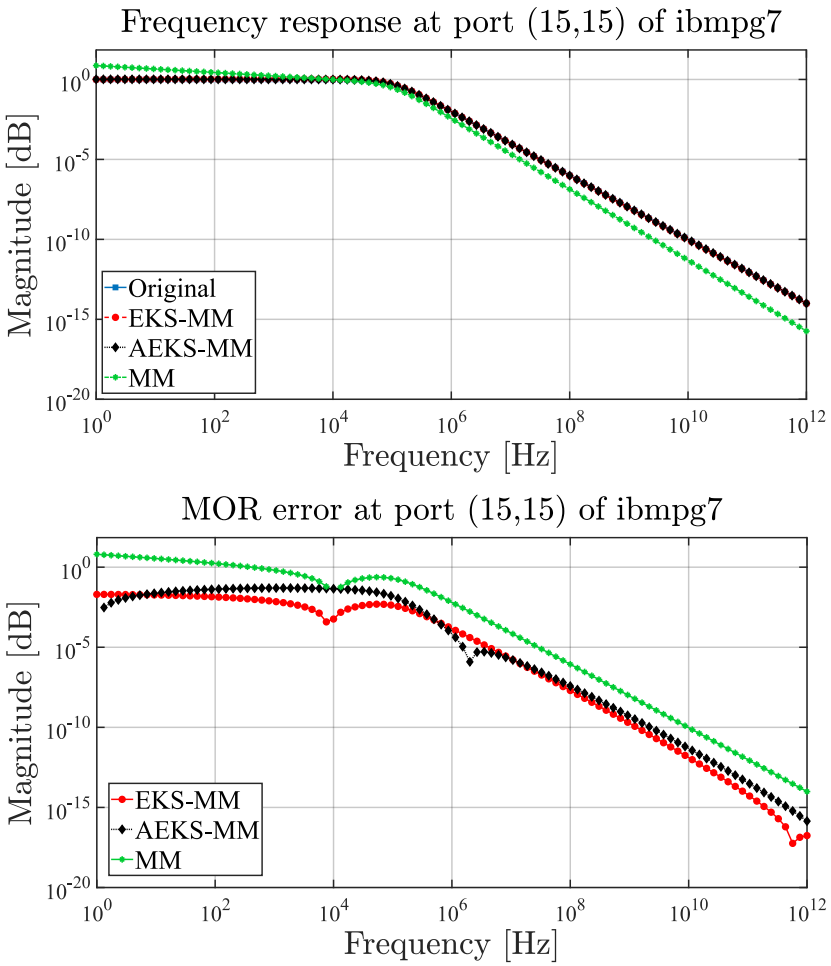


Figure 4.4: Comparison of transfer functions and absolute error magnitudes of ROMs obtained by EKS-MM, AEKS-MM, and MM in the frequency range $[10^0, 10^{12}]$ for ibmpg7 at port (15,15).

To demonstrate the accuracy of our method, we compare the transfer functions of the original model with those of the ROMs generated by EKS-MM, AEKS-MM, and MM. The corresponding transfer functions for the selected interconnect lines from the bmpg1 and ibmpg4 benchmarks, over the frequency band $[10^0, 10^{12}]$ Hz, are shown in Fig. 4.3. Additionally, Fig. 4.4 presents the transfer functions of the ROMs produced by EKS-MM, AEKS-MM, and MM, along with the corresponding absolute errors with respect to the original model, for the selected line from the ibmpg7 benchmark within the same frequency band.

As can be observed, the responses of the EKS-MM and AEKS-MM ROMs closely follow the original model across the entire frequency range, whereas the MM ROM exhibits noticeable deviations. In particular, the ROMs generated by MM fail to accurately capture dips and overshoots appearing at certain frequency bands, leading to significant mismatches with

the original response. This behavior highlights the advantage of using two-sided projection methods such as AEKS-MM for accurately capturing broadband dynamics.

4.6.2 EM stress evaluation on a seven-segment tree

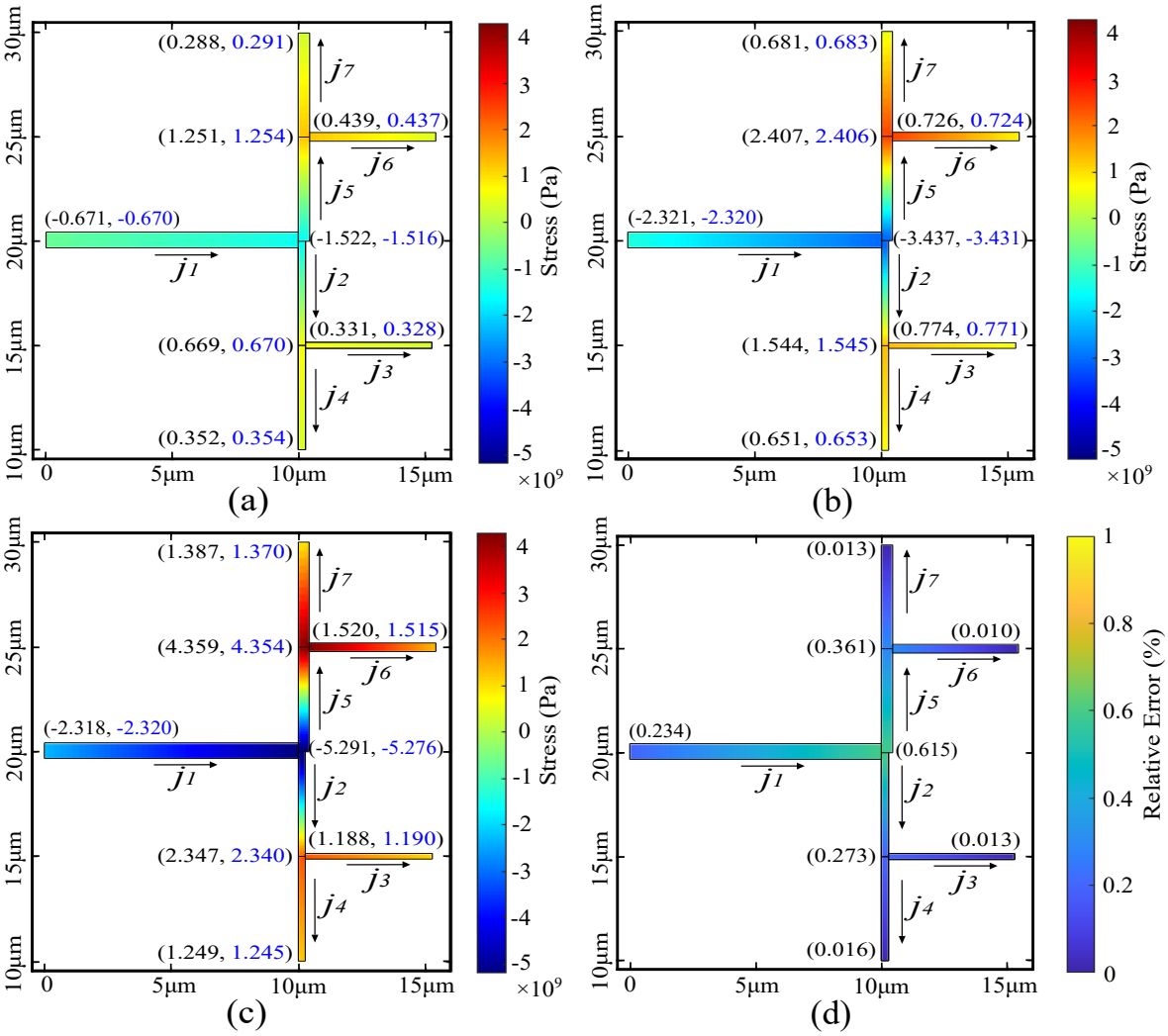


Figure 4.5: (a)-(c): Comparison of EM stress at $t = 5$, $t = 10$, and $t = 20$ years, respectively. The stress at each node is shown as a tuple, with our AEKS-MM solution in black and the COMSOL solution in blue text. (d): The relative error between our proposed solution and the COMSOL solution at $t = 20$ years.

To validate the accuracy of our approach on complex geometries, an artificial seven-segment interconnect tree with four T-junctions was constructed, where each segment was assigned a different width and current density. The segment widths are defined as follows: $w_1 = 0.6\ \mu m$, $w_2 = w_3 = w_4 = 0.25\ \mu m$, $w_5 = w_6 = w_7 = 0.4\ \mu m$, while the segment lengths are depicted in Fig. 4.5. The corresponding constant current densities are: $j_1 = -2 \times$

10^9 A/m^2, $j_2 = -3 \times 10^9 A/m^2$, $j_5 = 4 \times 10^9$ A/m^2, and $j_3 = j_4 = j_6 = j_7 = 1 \times 10^9$ A/m^2. Also, we performed transient simulation using the ROM from AEKS-MM at $t = 5$, $t = 10$, and $t = 20$ years, as shown in Figs. 4.5(a)-(c), with the colorbars depicting the spatial distribution of the stress build-up across the artificial trees. The tuples next to boundary or junction nodes are the values computed by our method and COMSOL. In Fig. 4.5(d), the relative error along the tree is found to be well below 0.7% with a reduced order $r = 4$ after applying a discretization step $Dx = 2.5$ μm. This stress distribution reveals compressive stress near anodes and tensile stress near cathodes, as expected from EM-driven atomic flux. In particular, junction and via junction points exhibit localized stress peaks, indicating potential EM hotspots where material failure is likely to occur. d stress values.

4.6.3 Transient EM analysis on IBM power grid benchmarks

For EM stress assessment on very large-scale power grids, we utilized the interconnect lines provided in Table 4.1 to evaluate the scalability and reliability of our proposed methodology. These benchmarks include up to 3.2 million degrees of freedom (DOFs), over 2300 interconnect segments, and as many as 966 ports, representing realistic and highly complex industrial designs. Specifically, the ROMs generated by AEKS-MM were used to perform transient EM analysis over a simulation window of 20 years, with a discretization step of $t = 0.05$ years using the BE method. The results for the selected interconnect lines from the IBM benchmarks are presented in Table 4.2, where we report the runtimes of the original model, the runtimes of the AEKS-MM simulation (including the ROM construction time as listed in Table 4.1), and the corresponding runtimes obtained from COMSOL simulation. Furthermore, the table includes the speedups achieved by our methodology with respect to both the original model and COMSOL, along with accuracy metrics, where the COMSOL results are used as the reference solution.

As shown, our methodology achieves an average speedup of $15\times$ compared to the original model, and an average speedup of $100\times$ relative to COMSOL simulations. It is also observed that the ROM construction phase accounts for about 85% of the total simulation time, indicating that the main computational overhead stems from the reduction procedure itself. Although the reduction is performed only once for each interconnect structure during EM analysis, in large-scale power grids containing tens of thousands of interconnects, this overhead could become a bottleneck. This observation highlights the critical importance of selecting an efficient

Krylov subspace generation method for MOR techniques applied to EM reliability analysis. Moreover, our methodology achieves a mean relative error of 0.4% compared to COMSOL, while maintaining an average deviation of only 0.12% to the original model. These gains are especially significant given the limitations of COMSOL in large-scale EM analysis. Although COMSOL provides a flexible environment for FEM-based PDE simulation, it solves the full-order system without inherent model reduction capabilities. As a result, it suffers from poor scalability and high computational cost when applied to large-scale interconnect structures, making it impractical for fast or repeated EM stress evaluations. Furthermore, COMSOL is constrained by an upper bound of approximately one million DOFs and demands substantial memory resources, often leading to excessive runtimes or simulation failures.

Table 4.2: Results between the AEKS-MM method and COMSOL for large-scale IBM power grids

Bench.	Transient analysis (seconds)			Speed-up (×)		Accuracy (%)	
	Original	**AEKS - MM**	COMSOL	Original	COMSOL	Original	**AEKS - MM**
ibmpg1	2.19	0.19	24.49	11.50×	128.58×	0.17%	0.51%
ibmpg2	2.69	0.31	79.57	8.78×	259.52×	0.04%	0.08%
ibmpg3	6.37	1.36	141.83	4.70×	104.58×	0.24%	0.83%
ibmpg4	10.97	1.85	176.92	5.92×	95.40×	0.14%	0.59%
ibmpg5	35.48	2.58	184.87	13.74×	71.57×	0.11%	0.44%
ibmpg6	121.82	5.35	257.48	22.77×	48.12×	0.06%	0.07%
ibmpg7	180.82	7.27	318.45	24.88×	43.81×	0.09%	0.10%
ibmpg8	281.79	11.90	522.83	23.67×	43.92×	0.08%	0.53%

Regarding the spatial accuracy of the EM stress distribution, Fig. 4.6 presents the hydrostatic stress along the first 27 segments (total length $2400\ \mu$m) of the selected interconnect line from ibmpg1 benchmark after 20 years of simulation. The gradual stress buildup and eventual saturation over time indicate that the system approaches a steady-state back-stress equilibrium, consistent with Korhonen's diffusion model. As can be observed, the stress profiles generated by AEKS-MM are in excellent agreement with the reference COMSOL solution along the entire length of the line. Finally, to assess the capability of our approach in handling time-dependent current density inputs, we applied a periodic piecewise current density input at the left boundary node of the previously selected interconnect line. The applied pro-

file starts from 0 and oscillates between 4×10^9 A/m^2 and -4×10^9 A/m^2. Fig. 4.7 shows both the applied current density input and the corresponding transient EM stress responses obtained by AEKS-MM and COMSOL at the left boundary node over a 20-year period. The results demonstrate that both methods achieve an excellent match throughout the entire transient simulation, even with time-variant input.

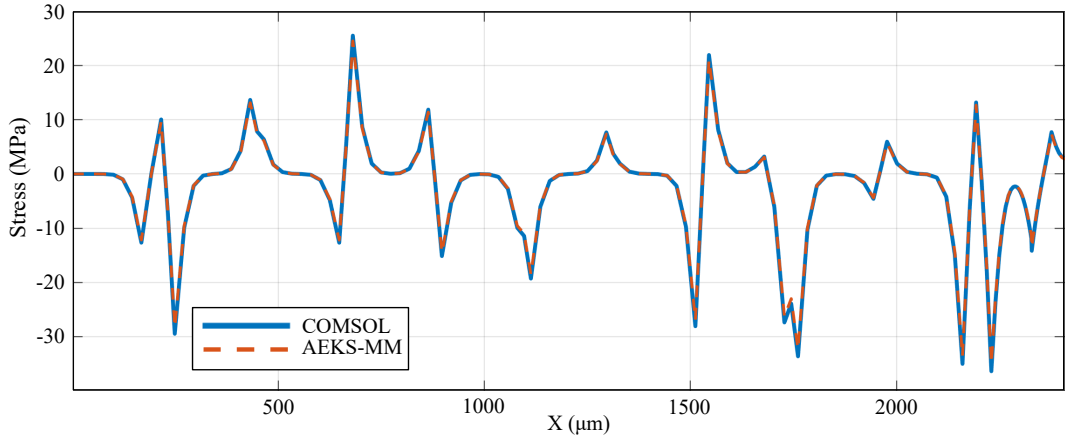


Figure 4.6: Stress profile comparison along the first 27 segments of the selected line from ibmpg1 benchmark at $t = 20$ years.

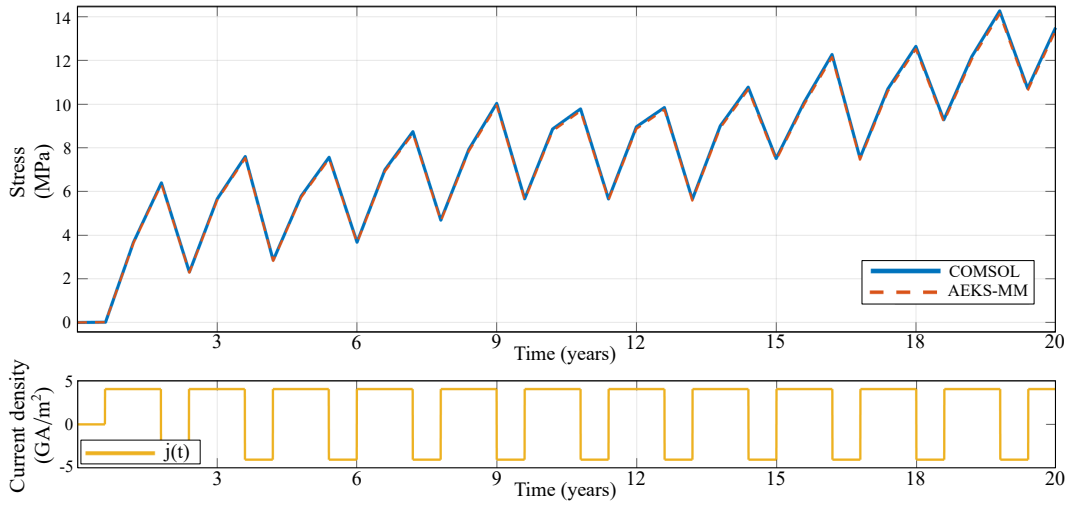


Figure 4.7: Transient EM stress response at the left boundary node under a periodic current density input, comparing AEKS-MM and COMSOL results over a 20-year simulation.

4.7 Summary

In this chapter, we proposed a fast numerical approach for transient analysis of EM-induced stress based on the MOR technique at discrete spatial points of general interconnect structures. By leveraging the flexibility of the AEKS-MM framework, the proposed methodology exploits sparse solve operations to dramatically reduce the overall reduction runtime, achieving up to a $7\times$ speedup compared to conventional numerical approaches such as MM and EKS-MM. At the same time, AEKS-MM maintains an acceptable error margin in the transfer function approximation relative to the original model, while significantly improving the accuracy over standard MM techniques. A key aspect of our methodology lies in the careful selection of the Krylov subspace used for model reduction. Since numerical MOR approaches for EM stress analysis critically depend on the underlying subspace construction, optimizing this step is essential for ensuring both high accuracy and computational efficiency. For the EM stress evaluation, the experimental results demonstrated that AEKS-MM ROMs achieve high accuracy compared to full-order simulations, maintaining a relative error of less than 0.5% with respect to COMSOL solutions. Moreover, the proposed approach significantly reduces simulation runtimes, achieving average speedups of $100\times$ relative to COMSOL and $15\times$ compared to full-order transient simulations. Furthermore, AEKS-MM exhibits strong robustness under time-dependent current density inputs, accurately tracking stress evolution even in dynamically changing scenarios. Although this work focused on planar copper-based 2D power grids, the AEKS-MM framework is fully extensible to more advanced interconnect technologies. In particular, it can be applied to multi-layer metal stacks and 3D-ICs with through-silicon vias (TSVs), as EM behavior is governed by similar PDE formulations. In such complex geometries, the use of efficient ROM techniques such as AEKS-MM becomes even more crucial for scalable and reliable EM analysis. Finally, our method is applicable not only to the nucleation phase but also to the growth phase, as the generated ROMs can be utilized to model the stress evolution throughout the entire EM process.

Chapter 5

Security closure approach for EM-based attacks

5.1 Introduction

Nowadays, the security and reliability of VLSI devices have become paramount concerns, as they are susceptible to malicious alterations like Hardware Trojans (HTs). More specifically, security issues are especially evident in fabless semiconductor industry, where the practice of outsourcing IC manufacturing to external foundries has raised concerns about the security of the produced ICs [54]. These problems are coupled with electromigration (EM) challenges since EM has become a significant reliability concern due to the increasing demand for performance in advanced technology nodes [4].

Consequently, attackers are progressively utilizing reliability-based HTs to deliberately induce long-term consequences on the stability and performance of the IC. These malicious components are designed with the specific target of accelerating several reliability issues, such as premature aging or EM in particular interconnect or power grid structures of the IC [55]. The power grid structures of the chip play a crucial role in maintaining reliable IC operation by distributing power to logic gates. To address the increased current and mitigate EM stress, multiple metal layers incorporate substantial reservoirs as passive wire segments, enhancing reliability robustness with minimal impact on performance and power consumption [56]. However, these reservoirs also present vulnerability to stealthy attacks aiming to reduce or remove them from the power grid network within the design.

As a result, a significant class of HTs has evolved into reliability-based Trojans [55],

capable of exploiting the aging effects of the targeted device. Most commonly, these HTs aggravate EM stress on power-hungry blocks and can be strategically placed in various parts of the IC, such as power grids [57] and high current density signal blocks like clock networks [58]. All of these components consist of large-scale, general multi-segment interconnects and can be compromised using a sink insertion attack. These sinks can drastically degrade the time-to-failure (TTF) while minimally impacting the voltage drop of the wire, as they are passive components.

Power grid structures play a critical role in the reliable operation of integrated circuits as they are responsible for distributing power to logic gates and maintaining overall functionality in VLSI designs [59]. To address the increased current within power grids and mitigate EM stress, substantial reservoirs are added across multiple metal layers. These reservoirs consist of passive wire segments designed to enhance reliability robustness by providing greater resistance, while minimizing impacts on performance and power consumption of the power grid structure [56]. While reservoirs are a crucial component of power grids, they are also susceptible to stealthy attacks that aim to reduce or remove the reservoirs from the power grid network of the design.

To this end, an efficient security closure methodology for the detection and mitigation of HTs, which can be easily integrated into VLSI design flows, has become a critical objective in ensuring the trustworthiness and reliability of electronic systems [56]. In this work, we presented a comprehensive security closure methodology for identifying potential vulnerable structures in both power grid lines and general interconnect trees within IC designs. For power grid lines, we adopt a semi-analytical approach based on the method proposed in [60], which computes the TTF for each power grid line independently. This method discretizes only the spatial domain while keeping the time domain continuous, and employs a binary search algorithm to ensure fast convergence. For interconnect trees, we propose a semi-analytical approach using the matrix exponential technique described in Chapter 3, where each tree is analyzed independently. This approach also discretizes the spatial domain while treating time continuously and uses a bisection root-finding method to determine the expected TTF with high accuracy and fast convergence. The main contributions of this chapter are summarized as follows. *Firstly*, our methodology enables the calculation of the TTF for any given multi-segment structure, whether it is an interconnect line or tree, by directly computing the analytical solution at each time point. For power grid lines, the TTF is determined using a

binary search algorithm, while for interconnect trees, a bisection root-finding algorithm is employed to ensure fast convergence. *Secondly*, the TTF of each line or tree is computed separately and in parallel, making the overall methodology highly efficient and scalable for large-scale designs. Finally, we demonstrate the effectiveness of our approach on IBM power grid benchmarks by detecting vulnerable lines and estimating their TTFs with and without reservoir components. We also evaluate our methodology on large-scale OpenROAD benchmarks by identifying susceptible interconnect trees and computing their TTFs both with and without the presence of sinks.

The rest of the chapter is organized as follows. Section 5.2 describes the EM background of power grid structures, as well as the creation of EM-based reliability Trojans through stealthy reservoir removal and passive sink insertion. Section 5.3 presents our main contribution on the security closure methodology for identifying susceptible power grid lines and interconnect trees, and computing their TTF with and without the presence of reservoirs or sinks. Section 5.4 demonstrates our experimental results on large-scale IBM and OpenROAD power grid benchmarks. Finally, conclusions are drawn in Section 5.5.

5.2 Review of EM-based trojan attacks

Reliability-based attacks often exploit vulnerabilities that exist across the design and fabrication stages of integrated circuits, as illustrated in Fig. 5.1. Typically, in-house design companies outsource the final stages of the physical design to third-party foundries. At this point, masks are generated using lithographic tools based on the submitted layout, and then the chip is fabricated. A third-party foundry could alter the mask without the knowledge of the original design house and still successfully deploy the compromised chip. The challenge in such attacks lies in designing an EM-based Trojan capable of degrading a wire or structure in a controlled way such that it fails at a specific target time, allowing malicious functionality to be triggered. Importantly, the Trojan must remain stealthy, avoiding any impact on the chip's performance, power consumption, or design rule constraints, thereby evading traditional verification and testing. In the following section, we outline two main EM-based attack strategies capable of achieving these goals while remaining undetected throughout the design and fabrication flow.

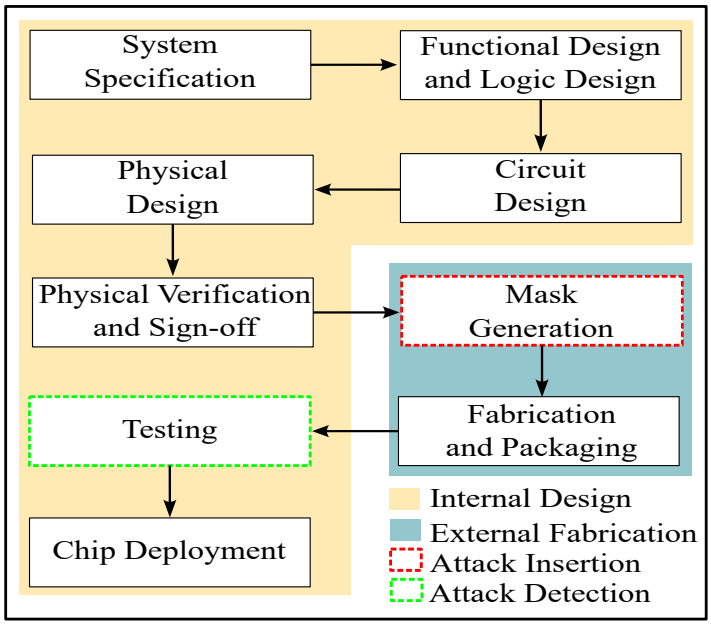


Figure 5.1: Overview of the IC design and fabrication process, showing potential attack and detection points.

5.2.1 Reservoir removal in interconnect lines

EM-based HTs are typically formed by incorporating supplementary resistive elements, such as narrow wires, into the interconnect sections of integrated circuits. The inclusion of these resistive elements induces a localized rise in current density, resulting in accelerated EM stress and eventual interconnect failure [56]. Attackers can strategically position these resistive elements within crucial circuit paths, such as clock tree networks, to create HTs that trigger specific system failures.

Besides attacks that can be possibly detected through side-channel analysis methods, there is another option that remains completely stealthy as it does not introduce any additional gates or elements, instead it directly targets the physical design of the IC. One of the possible approaches to accomplish this is by removing or modifying the reservoir structures, which are passive interconnect components, within the power grid. These reservoirs are typically positioned at the cathode terminal of lines, as seen in Fig. 5.2, that are more prone to EM failures. More specifically reservoir enforce the steady-state stress to remain below the critical stress, in order to make the power grid structure immortal to EM failures. By removing the reservoir, the EM stress on the line accelerates, leading to a stealthy degradation of the TTF well below the desired level.

By removing these reservoirs, attackers can silently accelerate EM degradation, effec-



Figure 5.2: EM-based Trojan for reservoir removal attacks.

tively compromising the power grid's functionality without causing noticeable anomalies in the IC's performance, power consumption, or IR drop. This characteristic poses a significant challenge in distinguishing the attacked circuit from legitimate circuit behavior. Furthermore, in advanced technology nodes where the margins for EM safe design are narrower, the threat posed by these Trojans becomes even more concerning, as they can remain undetected by various side-channel analysis methods. All of the above have made security closure methodologies a critical aspect of the physical design methodologies.

5.2.2 Sink insertion in interconnect trees

Another prominent EM-based Trojan strategy involves the insertion of resistive components or small metal wires into specific parts of the circuit, such as signal nets and clock trees. These narrow wires can be placed in several parts of the interconnect structures, that are empty or contain dummy fillers, while carrying high average currents. These EM-based HTs can accelerate the EM stress of the interconnects, leading to failures well before the targeted lifetime of the circuit [56]. In order to accomplish these type of attacks, sinks can be positioned to the anode of an interconnect segment in order to attack its cathode as shown in Fig. 5.3. More specifically, the sink that is inserted intensifies the EM stress to the anode, causing a stealthy decrease of the TTF well below the expected lifetime.

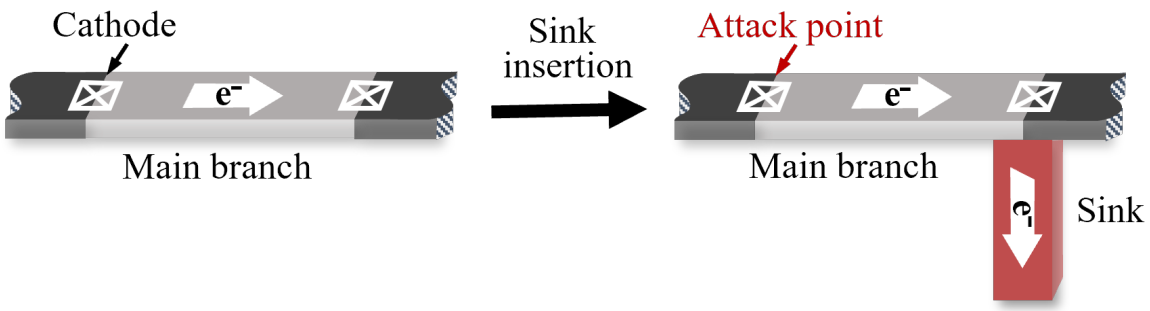


Figure 5.3: EM-based Trojan for sink insertion attacks.

An important aspect of these types of attacks is their minimal impact on the IR drop and power consumption, as the HT is utterly a passive metal added to the interconnect structure. As a result, identifying the affected circuit from ordinary circuit behavior is significantly challenging due to this characteristic. This stealthy nature makes detection extremely difficult, particularly in advanced process nodes where EM margins are minimal. As with reservoir removal, these attacks emphasize the need for EM-aware and security-driven design methodologies during the physical implementation phase.

5.3 Proposed security closure framework

This section introduces our security closure methodology for identifying EM-susceptible structures in power grids. We address two categories of EM-based Trojan attacks, involving reservoir removal in power grid lines and sink insertion in interconnect trees. For each case, we present a specialized TTF estimation approach based on semi-analytical models.

5.3.1 Methodology for reservoir-based attack mitigation

Detecting and mitigating EM-based Trojans that exploit reservoir removal in power grid structures is a complex task, primarily due to their stealthy nature and the high density of metal lines in modern ICs. These attacks do not introduce observable side-channel effects, making traditional detection methods ineffective. To address this challenge, we propose a targeted security closure methodology that enables the per-line analysis of power grid segments, aiming to identify the specific lines that would become vulnerable under a potential reservoir removal scenario. In particular, we extract the power grid line separately and apply the FDM discretization on each line, as described in [61]. By discretizing each line using FDM, we can construct the systems of equations like Eq. 3.6. This parallel approach allows us to effectively model and analyze the behavior of the power grid, enabling accurate assessment and evaluation of its reliability.

Once the equation systems are formulated, we employ an efficient semi-analytical solver, which was proposed in [60], specifically designed for systems resulting from FDM spatial discretization on power grid line structures. This approach leverages the unique tri-diagonal structure of the resulting system matrix $\mathbf{G}$ which easily tracks Fast Poisson solvers [62] and leads to the following closed-form matrix equation:

$$\boldsymbol{\sigma}(t) = \mathbf{V}\mathbf{L}(t)\mathbf{V}^T\mathbf{B}\mathbf{j} \tag{5.1}$$

where:

$$\mathbf{L}(t) = \begin{bmatrix} t & & & \\ & \frac{e^{\lambda_2 t}-1}{\lambda_2} & & \\ & & \ddots & \\ & & & \frac{e^{\lambda_n t}-1}{\lambda_n} \end{bmatrix} \tag{5.2}$$

with $\mathbf{V} \in \mathbb{R}^{n\times n}$ is the matrix containing the eigenvectors of matrix $\mathbf{A}$ and λ_i with $i \in [1, n]$ are the corresponding eigenvalues. The fundamental advantage of these method is that once the Eq. 5.1 is constructed, then the stress can be easily computed by substituting the desired time stamp t into the equation.

An important aspect of these method is that utilizes the unique tri-diagonal structure of matrix $\mathbf{G}$ to take advantage of fast Poisson solvers, enabling the determination of eigenvalues and eigenvectors in advance. Specifically, the operations of multiplying matrices $\mathbf{V}^T$ and $\mathbf{V}$ with vector $\mathbf{r}$, denoted as $\mathbf{V}^T\mathbf{r}$ and $\mathbf{V}\mathbf{r}$, respectively, perform a Discrete Cosine Transform of type-II (DCT-II) and an Inverse DCT of type-II (IDCT-II). By employing these transformations, the computational complexity of matrix multiplication is reduced from $\mathcal{O}(n^2)$ to $\mathcal{O}(n \log n)$. This solution offers a straightforward and easily parallelizable closed-form equation that can be independently applied to each different power grid line, efficiently computing the EM transient stress for a given time t in near-linear time.

Another important part of the proposed is the calculation of the expected TTF. While the solution methodology is capable of independently computing the EM stress at each time stamp, it cannot determine the TTF beforehand. To determine the TTF, the methodology requires the specification of a time interval denoted as $[t_{min}, t_{max}]$. This interval serves as a reference for identifying the specific time stamp at which the power grid reaches the critical stress level $\sigma_{critical}$, thereby indicating the TTF. Following the determination of the time interval, a rightmost binary search approach is employed within this interval. This involves repeatedly calculating the EM stress at selected time stamps such as:

$$t_{mid} = \textit{floor}((t_{left} + t_{right})/2)$$

until convergence is achieved. Convergence is considered to occur when the calculated stress matches the critical stress value of the technology. This iterative process ensures the accurate

estimation of the expected TTF for the power grid structure. The complexity of the binary search algorithm is $\mathcal{O}(\log t)$, where t represents the length of the time interval. However, it is worth noting that the time intervals involved in power grid analysis are typically tight and rarely exceed 100 years. Therefore, the overall computational complexity remains manageable and still can be performed independently for each power grid line.

After computing the TTF for each power grid line, our methodology identifies the susceptible lines. These susceptible lines are the ones that would become vulnerable and fail in the event of a potential EM-based Trojan attack that involves reservoir removal. By detecting these susceptible lines, our methodology provides valuable insights into the critical points within the power grid structure that are prone to such attacks. Furthermore, the proposed method reports the TTF with and without the presence of reservoirs, which helps in understanding the impact of reservoir removal on the reliability of the IC. This information enables proactive measures to enhance the security and reliability of the IC, allowing for the implementation of targeted countermeasures to protect against EM-based Trojan attacks.

Since our methodology performs exhaustive simulations on the power grid lines that are more susceptible to the creation of EM hotspots, the power grid network can be considered EM-safe if the reservoir removal attack does not result in the failure of these lines. The important steps of our method are summarized in the Alg. 8, while the calculation of the TTF is shown in Alg. 9.

Algorithm 8: Security Closure Methodology for Reservoir Removal Attacks.

1 Extract the power grid network from the design.
2 Construct the corresponding discretized system of Eq. 3.6.
3 Set the analysis interval $[t_{min}, t_{max}]$ to perform the TTF calculation of each line.
4 For all the lines in parallel perform binary search of Alg. 9,
$TTF =$ `bs_right_most`(t_{min}, t_{max})
5 Determine the susceptible lines of the power grid design.
6 Report all the corresponding TTFs with and without reservoirs of the susceptible lines.

Algorithm 9: Calculation of TTF based on the rightmost binary search.

Input: t_{min}, t_{max}

Output: time to fail TTF

$t_{left} = t_{min}$
$t_{right} = t_{max}$
while $t_{left} < t_{right}$ **do**
    Set the new time stamp $t_{mid} = floor((t_{left} + t_{right})/2)$
    Calculate the EM stress at t_{mid} by employing the analytical method of [60].
    if $\sigma(t_{mid}) > \sigma_{critical}$ **then**
        $t_{right} = t_{mid}$
    else
        $t_{left} = t_{mid} + 1_{year}$
    end
    $TTF = t_{right}$
end

5.3.2 Methodology for sink-based attack mitigation

In addition to reservoir removal attacks, sink-insertion attacks exploit EM vulnerabilities within interconnect trees while maintaining stealthy characteristics. These attacks can accelerate EM degradation without altering the circuit's functional behavior or side-channel profile. However, as with power grid structures, the increasing complexity and scale of modern interconnect networks significantly complicate the task of comprehensive EM analysis. To overcome this, we propose an efficient security closure methodology that enables the concurrent analysis of each interconnect tree. This involves the individual extraction of distinct multi-segment interconnects, followed by the application of FDM discretization to each extracted segment. Finally, and due to the diffusion barrier between the different metal layers, we can construct independent ODE systems of Eq. 3.6 for each interconnect tree. This strategy allows the proposed methodology to efficiently simulate all the different systems in parallel.

After formulating the equation systems, we utilize a highly efficient semi-analytical solver, as proposed in Chapter 3, which is based on the matrix exponential. More specifically, considering that the EM stress is known at $t = 0$, and defining $\mathbf{A} = \mathbf{C}^{-1}\mathbf{G}$ and $\mathbf{b} = \mathbf{C}^{-1}\mathbf{B}\mathbf{j}(t)$,

the solution of Eq. (3.6) for every time step is given by the following integral:

$$\sigma(t) = e^{t\mathbf{A}}\sigma(0) + \int_0^t e^{(t-\tau)\mathbf{A}}\mathbf{b}\, d\tau \tag{5.3}$$

Moreover, leveraging the assumption that each segment in an interconnect structure is carries a constant current, then we can derive the following equation:

$$\sigma(t) = e^{t\mathbf{A}}\left(\sigma(0) + \mathbf{A}^{-1}\mathbf{b}\right) - \mathbf{A}^{-1}\mathbf{b} \tag{5.4}$$

which can be solved analytically through the approximation of the matrix exponential and independently for every time stamp.

Another crucial part of our methodology involves the efficient estimation of the expected TTF. Although the analytical solution approach can compute the EM stress at each time stamp independently, it cannot predict the TTF in advance. In particular, to calculate the TTF, our methodology requires the definition of a time interval as $[t_{\text{min}}, t_{\text{max}}]$. This interval acts as a reference for locating the exact time point when the interconnect reaches the critical stress level, σ_{crit}. Once the time interval is determined, we employ the root-finding bisection method. Although conceptually similar to Algorithm 9, the bisection method is more appropriate here due to the continuous nature of the stress function resulting from the matrix exponential formulation. This approach is continuously decreasing the interval, by computing the EM stress at the selected time points, until the final convergence is achieved. Convergence is attained when the calculated stress matches the critical stress value of the technology. This iterative process guarantees the precise and efficient estimation of the expected TTF for all the interconnect trees.

After calculating the TTF for multi-segment interconnects, our approach identifies all the vulnerable trees. These susceptible trees are the ones prone to failure in case of a potential EM-based Trojan attack involving sink insertion. By detecting these vulnerable trees, our method offers valuable insights into the critical points within the interconnect structures susceptible to such attacks. Additionally, the proposed technique provides TTF values with and without sinks, aiding in understanding the impact of sink insertion on IC reliability. This information facilitates proactive measures to improve IC security and reliability, allowing for targeted countermeasure implementation against EM-based Trojan attacks.

All the steps of our security closure methodology are summarized in the Alg. 10, while the calculation of the TTF is shown in Alg. 11.

Algorithm 10: Security Closure Methodology for Sink Insertion Attacks

1 Extract multi-segment trees from the design
2 Define the interval $[t_{\text{min}}, t_{\text{max}}]$ for TTF calculation of each tree
3 **for** *each tree* **do**
4 Perform the bisection method (Alg. 11) to compute TTF
5 **end**
6 Identify susceptible trees within the design
7 Report the TTFs for susceptible trees, with and without sinks

Algorithm 11: Calculation of TTF using the Bisection Method

Input: t_{min}, t_{max}, threshold ϵ

Output: time to fail TTF

1 $t_{left} \leftarrow t_{min}$
2 $t_{right} \leftarrow t_{max}$
3 **while** $t_{left} - t_{right} < \epsilon$ **do**
4 $t_{mid} \leftarrow (t_{left} + t_{right})/2$ `// Set the new time stamp`
5 **if** $func(t_{mid}) == 0$ **then**
6 **break** `// Exit loop if function value is zero`
7 **else if** $func(t_{left}) * func(t_{mid}) < 0$ **then**
8 $t_{right} \leftarrow t_{mid}$
9 **else**
10 $t_{left} \leftarrow t_{mid}$
11 **end**
12 **end**
13 $TTF \leftarrow floor(t_{mid}/1_{year})$ `// Compute the TTF in years`
14 **Def** `func(`t`)`**:**
15 Compute the EM stress $\sigma(t)$ by employing [61]
16 **return** $\sigma(t) - \sigma_{crit}$;
17 **end**

5.4 Experimental results

In this section, we present the experimental evaluation of the proposed methodologies for assessing EM-induced degradation in large-scale IC designs. Our framework is applied to two representative benchmark sets: the IBM Power Grid (IBMPG) benchmarks [52], targeting the

analysis of power grid lines under potential reservoir-removal attacks, and the OpenROAD power grid benchmarks[1], focusing on sink-insertion attacks in interconnect trees. In both cases, each multi-segment interconnect line or tree is analyzed independently using a spatially discretized model, and the expected TTF is estimated using the appropriate root-finding method, with the critical stress level set to 50MPa [1]. Additionally, the TTF threshold for identifying susceptible lines or trees was set to 20 years, which is a typical target lifespan in processor design. All algorithms were implemented in Python using the scientific computing libraries SciPy and NumPy. The experiments were conducted on a Windows workstation equipped with an Intel Core i9-9900K processor of 16 threads and 32GB of RAM memory.

5.4.1 Evaluation on IBM power grid lines

For the reservoir-removal attack scenario, we validate the efficiency and accuracy of our methodology using several large-scale power grid benchmarks from the IBMPG set. The analysis was used to identify power grid lines that become vulnerable when reservoirs are removed, by calculating their TTF degradation under increased EM stress. The experimental results for each OpenROAD benchmark are presented in the columns of Table 5.1. The *#Lines* reports the number of extracted lines for each benchmark, while the *Dscr. step* indicates the discretization step of the spatial coordinate. The *Avg. #Discr. points* refers to the average number of discretization points used in constructing the ODE system. Column *#Susceptible lines* displays the total number of lines with a TTF less than the expected 20-year lifetime after removing the reservoir. The average reduction percentage of TTF for susceptible lines is presented in column *Avg. Diff.TTF (%)*. Additionally, the table includes the minimum TTFs with and without the reservoirs. Lastly, we provide the total number of segments for the largest susceptible line of each benchmark, along with the corresponding execution runtime.

As demonstrated in Table 5.1, our method effectively identifies the susceptible lines, which are considerably fewer in number compared to the total lines of each benchmark. This presents a significant challenge for any side-channel analysis techniques aiming to detect HTs. Furthermore, it is worth noting that the TTF of the lines has been significantly reduced by up to 65%, with a minimum expected lifetime of 8 years. Additionally, our methodology can be executed entirely in parallel for different lines as mentioned in Section 5.3.1, with the overall execution time typically dominated by the most vulnerable and structurally complex

[1]Github repository: `https://github.com/The-OpenROAD-Project`

line. In this context, the reported runtimes for the largest susceptible lines demonstrate the robustness and scalability of our approach, even under worst-case EM stress conditions.

Table 5.1: Experimental results of our security closure methodology for large-scale IBMPG benchmarks

Design	#Lines	Avg. Discr. step (μm)	Avg. #Discr. Points	#Susceptible lines	Avg. Diff. TTF (%)	Min. TTF (yrs)		Largest susceptible line	
						With Res.	No Res.	#Segm	Time(s)
ibmpg1	1162	3.38E-02	4569.02	19	64.95	45	12	946	15.32
ibmpg2	1163	6.31E-03	6007.28	25	52.54	38	15	153	0.30
ibmpg3	15276	2.27E+01	8886.88	27	37.63	42	10	464	5.44
ibmpg4	20959	5.23E-03	2957.34	13	38.78	55	13	389	8.51
ibmpg5	3065	1.35E-03	31131.13	47	61.44	59	14	1257	23.91
ibmpg6	21293	7.44E-01	5616.07	20	52.39	31	8	772	15.65
ibmpg7	38271	1.13E+01	3596.69	25	49.06	39	12	464	4.44
ibmpg8	38385	1.13E+01	3610.76	18	55.04	47	16	522	17.03

Finally, Fig. 5.4 and Fig. 5.5 demonstrate the stress build-up for a 57-segment line from the ibmpg6 benchmark, with and without the presence of a reservoir. In particular, Fig. 5.4 depicts the overall stress accumulation at $t = 20$ years, while Fig. 5.5 specifically focuses on the stress waveforms at the attack point of the line. As can be seen the attack point surpasses the critical stress level earlier, resulting in a reduced TTF of the line to 50%. These figures visually demonstrate the impact of reservoir removal Trojan attacks on the stress distribution and highlight the importance of reservoirs in maintaining the desired TTF of the power grid line.

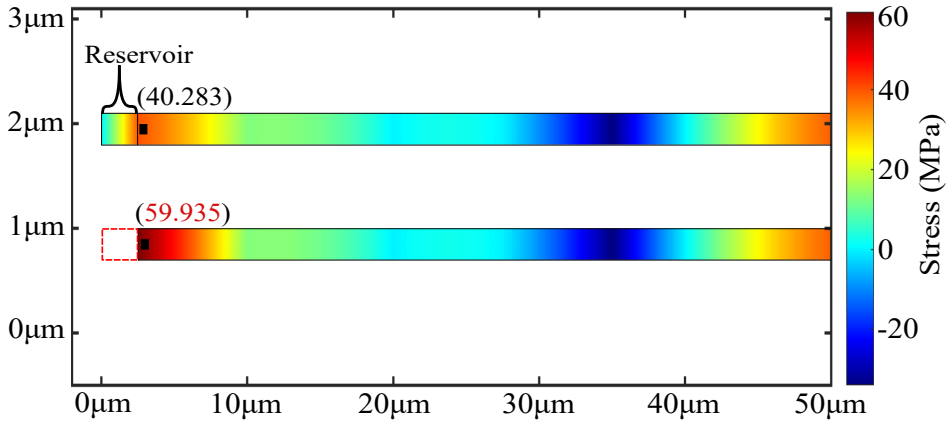


Figure 5.4: EM stress build-up at t = 20 years a 57-segment line from the ibmpg6 benchmark.

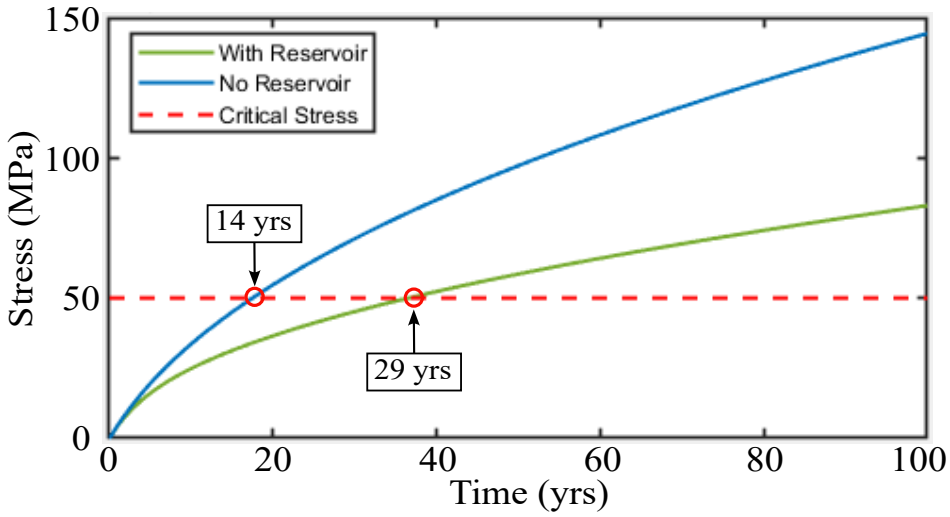


Figure 5.5: Transient simulation of the attack point for a 57-segment line from the ibmpg6 benchmark.

5.4.2 Evaluation on OpenROAD interconnect trees

For the sink-insertion attack, we evaluate the reliability and applicability of our methodology by applying it to interconnect trees extracted from OpenROAD benchmarks. These designs are implemented using various technology nodes, including commercial 12nm FinFET, 28nm FDSOI, and Nangate 45nm library. The selected benchmarks are characterized by large-scale structures and high current densities, both of which are representative of advanced technology nodes. Our method was used to detect interconnect trees susceptible to accelerated failure due to passive sink insertion. In Table 5.2, we present the experimental results for each OpenROAD benchmark. These include the number of extracted trees (*#Trees*), the discretization step of the spatial coordinate (*Dscr. step*), and the average number of discretization points employed in constructing the ODE system (*#Discr. points*). We also provide the overall count of trees with a TTF less than the expected 20-year lifespan after the sink insertion (*#Susceptible trees*), along with the average reduction percentage of TTF for these susceptible trees (*Avg. Diff.TTF (%)*). Moreover, the table reports the minimum TTF values both with and without the sink. Finally, we demonstrate the total number of segments for the largest susceptible trees of each benchmark, as well as the execution runtime.

Analyzing Table 5.2, we observe that our method successfully identifies the susceptible trees, which are notably fewer in number compared to the total trees of each benchmark. Moreover, by applying the sink insertion technique to those trees, a significant reduction in TTF has been achieved by up to 82.67%, with a minimum lifetime extending to 6 years. As

outlined in Section 5.3.2, our approach can be executed concurrently for different trees, with the execution time mainly dominated by the largest ones. Thus, the table demonstrates the excellent efficiency of our method, even for significantly large-scale benchmarks, as revealed by the short execution times of the largest susceptible trees.

Table 5.2: Experimental results of our security closure approach on the large-scale OpenROAD interconnect trees

Tech	**Design**	**#Trees**	**Avg. Discr. step (μm)**	**Avg. #Discr. points**	**#Susceptible trees**	**Avg. Diff. TTF (%)**	**Min. TTF (yrs)**		**Largest susceptible tree**	
							No Sink	**With Sink**	**#Segm**	**Time (s)**
45 nm	dyn_node	697	0.96	615.89	15	67.16	33	10	252	7.45
	ibex	1182	0.87	654.64	31	72.15	41	11	369	5.99
	aes	1402	0.72	572.11	16	70.32	37	10	206	2.13
	jpeg	3505	0.72	674.84	39	71.73	37	9	632	1.67
	swerv	5413	0.65	693.12	56	75.75	38	8	620	8.34
28 nm	gcd	46	0.37	3941.09	9	58.61	33	13	138	5.87
	aes	191	0.35	1831.37	12	70.89	35	9	527	6.37
	jpeg	406	0.35	4682.85	18	80.26	39	6	1050	10.23
12 nm	gcd	2375	0.26	2756.54	22	67.90	33	10	211	2.68
	ibex	12472	0.16	2858.57	33	75.28	40	9	585	6.06
	jpeg	47603	0.13	3662.28	33	71.46	36	8	1097	6.10
	dyn_node	86024	0.12	12933.38	50	75.28	39	9	1355	14.56
	aes	110549	0.12	12974.93	88	82.67	58	10	1184	12.73

Finally, we applied our method to an artificial 22-segment tree as shown in Fig. 5.6 and Fig. 5.7. Specifically, Fig. 5.6 illustrates the EM diffusion across the segments of the tree at $t = 20$ years, while Fig. 5.7 shows the EM evolution at the attack point before and after the sink insertion. From the first, it is evident that the attack point has a significantly higher stress level than the critical stress, while the second demonstrates that the expected lifetime of the tree has been reduced to 75%. In this regard, we can comprehend the substantial influence on the tree's expected lifetime after the application of the sink insertion technique.

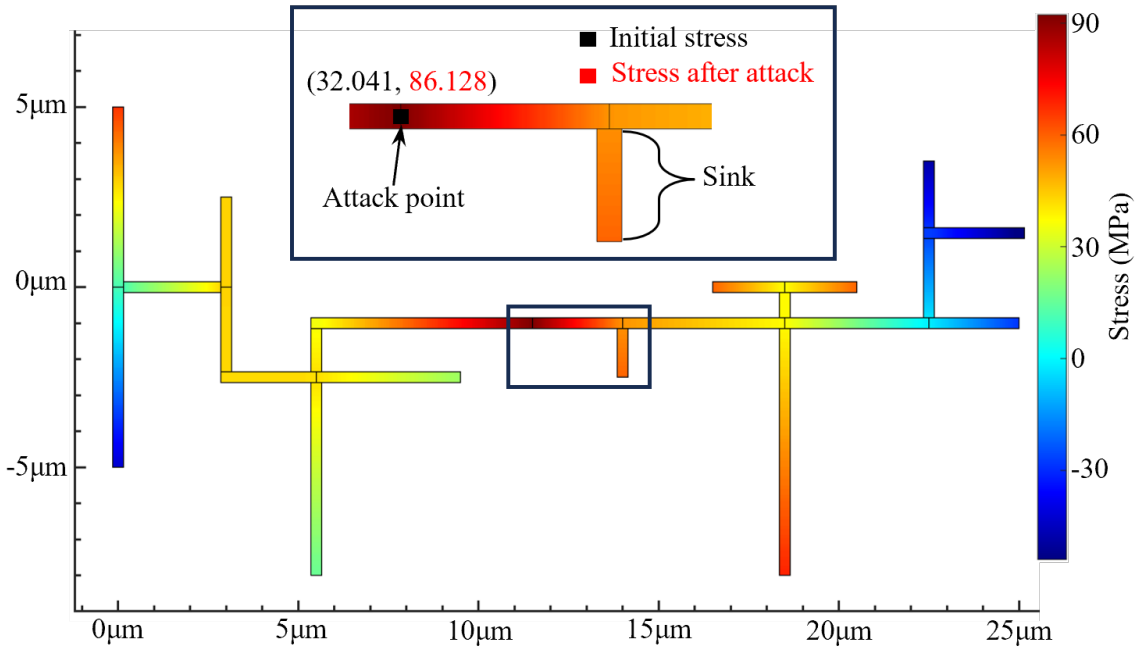


Figure 5.6: EM stress build-up at t = 20 years across an artificial 22-segment tree.

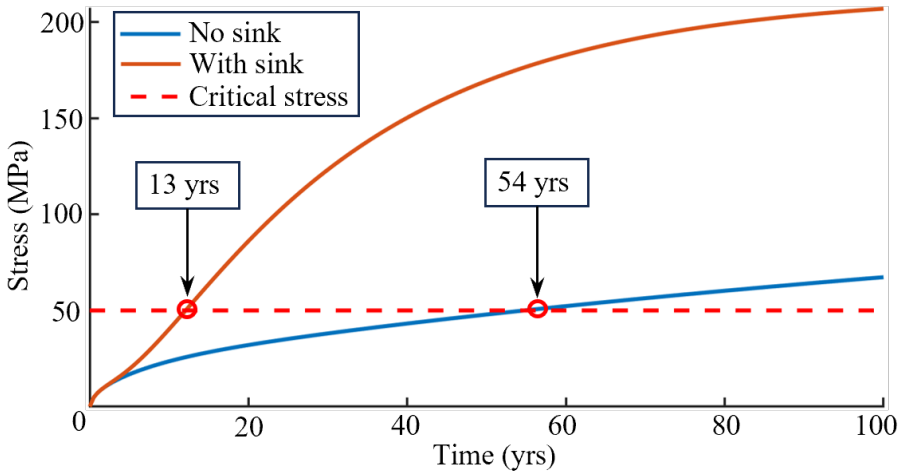


Figure 5.7: Transient simulation of the attack point from an artificial 22-segment tree.

5.5 Summary

In this work, we presented a unified security closure methodology for identifying potential vulnerable structures in both power grid lines and general interconnect trees within large-scale IC power grids. The proposed approach accurately computes the expected TTF for each multi-segment structure, both in the presence and absence of critical components such as reservoirs and sinks. Our methodology is fully parallelizable, enabling independent analysis of each line or tree, with total execution time primarily determined by the largest and most complex susceptible structure in the design. Experimental results on publicly used benchmarks demonstrate the scalability and efficiency of our approach, requiring less than 24 seconds for analyzing a power grid line with 1257 segments, and under 15 seconds for an interconnect tree with 1355 segments. These findings highlight that the proposed framework not only scales to industrial-size structures but also enables reliable security closure within realistic design-time budgets, making it suitable for integration into modern EDA flows.

Chapter 6

Conclusions and future directions

The concluding chapter summarizes the main contributions of this dissertation in the field of EM reliability and security for VLSI interconnects. It also discusses the broader significance of these findings in the context of modern IC design and outlines directions for future research.

6.1 Conclusions

This research tackled the long-term reliability challenges posed by EM in advanced semiconductor technologies by developing accurate and scalable methodologies for both EM analysis and enhancement of hardware-level security.

To this end, a complete and scalable framework for EM stress analysis was proposed, addressing both the pre-void and post-void phases of interconnect degradation. The methodology was built upon Korhonen's physics-based model and introduced a semi-analytical formulation, enabling time-continuous stress evaluation in complex geometries under realistic operating conditions. To further enhance computational efficiency, the framework integrated matrix exponential technique with Krylov subspace methods (EKS and RKS), enabling fast and accurate evaluation of stress evolution. Structural changes due to void formation were effectively handled through a dynamic tree-splitting mechanism, while void nucleation time and location were accurately predicted using a Newton-Raphson-based estimator. Together, these components formed a unified EM analysis framework that achieved substantial accuracy and runtime improvements over state-of-the-art numerical solvers on large-scale industrial benchmarks.

In addition to the core framework, a reduced-order modeling methodology was developed to further improve the scalability and efficiency of EM analysis. By exploiting the sparsity and structure of the EM system matrices, the proposed approach applied asymmetric projections based on the EKS, achieving compact and accurate approximations of the original system response. This allowed fast and scalable EM analysis in complex interconnect structures, significantly reducing computational cost without compromising accuracy. The method was validated across large industrial designs, demonstrating its suitability for integration into modern VLSI reliability workflows.

Furthermore, the security implications of EM phenomena were also addressed through the development of a dedicated security closure methodology, including both lines and trees. EM-based Trojan attacks were investigated, and a systematic mitigation framework was introduced to detect and suppress such threats. By combining physical modeling of EM effects with design-level countermeasures, we developed security-aware strategies that neutralize malicious modifications, such as reservoir removals and sink insertions. This work demonstrated the dual role of EM: not only as a reliability issue but also as a potential vector for hardware-level security attacks. The proposed security-aware techniques provided a foundation for building robust ICs that are resilient to both EM failure and hardware-level exploitation.

Taken together, the contributions presented in this dissertation offer a comprehensive response to the challenges posed by EM in advanced VLSI interconnects. By combining accurate modeling, computationally efficient techniques, and security design principles, this work advances the development of robust stress prediction solvers and security-aware mitigation strategies. These developments address fundamental and practical aspects of long-term reliability and hardware security, providing scalable solutions aligned with the demands of future IC design challenges.

6.2 Future directions

Extending the foundations established in this dissertation, the following research directions are proposed to further enhance the EM-based reliability in VLSI structures. These directions include, but are not limited to, the following key areas:

- Modern data-driven approaches can significantly accelerate EM stress analysis by learning the underlying physical behavior across large-scale interconnect trees. Recent advances have introduced GNNs and PINNs for fast and scalable EM prediction, capturing structural dependencies in interconnect layouts and incorporating Korhonen-based EM physics, respectively. Such models can serve as lightweight predictors or uncertainty estimators within the EM solver pipeline. In particular, combining these approaches with the proposed framework could enable real-time EM-aware reliability analysis during early design stages or Trojan detection through anomaly stress profiling.

- Although the proposed methods utilize FDM to model EM stress evolution, future work will explore the adoption of FEM to improve accuracy, especially in capturing complex geometries, localized stress effects, and void growth near 3D features such as vias. FEM's flexibility in meshing and boundary condition handling makes it particularly suitable for detailed post-void modeling and multiscale EM analysis. A promising direction is to develop a hybrid pipeline that couples the proposed modeling for global or pre-void stages with FEM-based modules for localized or post-void regions. This integration could leverage domain decomposition and multiscale modeling techniques.

- EM-induced degradation is strongly affected by localized Joule heating and thermal gradients, which can significantly accelerate atomic diffusion and lead to underestimation of failure risk if neglected. Future work will focus on incorporating thermal-aware EM modeling by extending the Korhonen-based PDE to include thermomigration effects. Moreover, resistance variation during void growth should be captured via dynamic updates to the system matrices, enabling more realistic simulation of circuit-level behavior degradation over time. By modeling these mechanisms, the proposed methods can better approximate real-world EM behavior and provide more accurate predictions under realistic scenarios.

- For hardware security, a future objective is to integrate the aforementioned directions into the proposed security framework. In particular, using ML models to identify non-physical stress patterns, along with thermal-aware modeling to uncover stealthy EM-triggered attacks hidden under localized heating, can significantly enhance Trojan detection. Leveraging these techniques, EM-aware design strategies can be explored to harden interconnect structures against Trojan injection. Such techniques may involve strategic reservoir placement, stress balancing, or routing constraints to reduce vulnerability to EM-based failures.

Publications

[1] **Pavlos Stoikos**, George Floros, Dimitrios Garyfallou, Nestor Evmorfopoulos, and George Stamoulis. A fast semi-analytical approach for transient electromigration analysis of interconnect trees using matrix exponential. In *Proceedings of the 28th Asia and South Pacific Design Automation Conference (ASP-DAC)*, page 1–6, 2023.

[2] **Pavlos Stoikos**, George Floros, Dimitrios Garyfallou, Nestor Evmorfopoulos, and George Stamoulis. Electromigration stress analysis with rational krylov-based approximation of matrix exponential. In *2023 19th International Conference on Synthesis, Modeling, Analysis and Simulation Methods and Applications to Circuit Design (SMACD)*, pages 1–4, 2023.

[3] Alexandra Takou*, **Pavlos Stoikos***, Moysis Moysis, George Floros, Nestor Evmorfopoulos, and George Stamoulis. An efficient security closure methodology for em-based attacks on power grid structures. In *2023 IEEE International Symposium on Defect and Fault Tolerance in VLSI and Nanotechnology Systems (DFT)*, pages 1–4, 2023.

[4] **Pavlos Stoikos**, George Floros, Nestor Evmorfopoulos, and George Stamoulis. A fast security closure approach for em-based attacks on general multi-segment interconnects. In *2024 20th International Conference on Synthesis, Modeling, Analysis and Simulation Methods and Applications to Circuit Design (SMACD)*, pages 1–4, 2024.

[5] **Pavlos Stoikos**, Dimitrios Garyfallou, George Floros, Nestor Evmorfopoulos, and George Stamoulis. Fast electromigration analysis via asymmetric krylov-based model reduction. *Electronics*, 14(14), 2025.

[6] **Pavlos Stoikos**, Dimitrios Garyfallou, George Floros, Nestor Evmorfopoulos, and George Stamoulis. A semi-analytical framework for pre- and post-void electromigration analysis in interconnect trees using matrix exponential. In *IEEE Transactions on Computer-Aided Design of Integrated Circuits and Systems*, 2025. [**Submitted**].

* Indicates equal contribution.

Bibliography

[1] Mohammad Abdullah Al Shohel, Vidya A. Chhabria, Nestor Evmorfopoulos, and Sachin S. Sapatnekar. Analytical modeling of transient electromigration stress based on boundary reflections. In *Procs. of the IEEE/ACM International Conference On Computer Aided Design*, pages 1–8, 2021.

[2] Awad H. Al-Mohy and Nicholas J. Higham. Computing the action of the matrix exponential, with an application to exponential integrators. *SIAM Journal on Scientific Computing*, 33(2):488–511, 2011.

[3] Roger B. Sidje. Expokit: a software package for computing matrix exponentials. *ACM Trans. Math. Softw.*, 24(1):130–156, 1998.

[4] C.-C. Yang et al. Microstructure modulation for resistance reduction in copper interconnects. In *Proceedings of the IEEE International Interconnect Technology Conference (IITC)*, pages 1–3, 2017.

[5] Jens Lienig and Matthias Thiele. *Fundamentals of electromigration-aware integrated circuit design*. Springer International Publishing, 2018.

[6] I. A. Blech. Electromigration in thin aluminum films on titanium nitride. *Journal of Applied Physics*, 47(4):1203–1208, 1976.

[7] J.R. Black. Electromigration—a brief survey and some recent results. *IEEE Transactions on Electron Devices*, 16(4):338–347, 1969.

[8] Sachin S. Sapatnekar. Electromigration-aware interconnect design. In *Proceedings of the 2019 International Symposium on Physical Design (ISPD)*, pages 83–90, 2019.

[9] J.R. Lloyd. New models for interconnect failure in advanced ic technology. In *2008 15th International Symposium on the Physical and Failure Analysis of Integrated Circuits*, pages 1–7, 2008.

[10] C. L. Gan, C. V. Thompson, K. L. Pey, and W. K. Choi. Experimental characterization and modeling of the reliability of three-terminal dual-damascene cu interconnect trees. *Journal of Applied Physics*, 94(2):1222–1228, 2003.

[11] M. A. Korhonen, P. Borgesen, King-Ning Tu, and Che Yu Li. Stress evolution due to electromigration in confined metal lines. *Journal of Applied Physics*, 73(8):3790–3799, 1993.

[12] Hai-Bao Chen, Sheldon X.-D. Tan, Xin Huang, Taeyoung Kim, and Valeriy Sukharev. Analytical modeling and characterization of electromigration effects for multibranch interconnect trees. *IEEE Transactions on Computer-Aided Design of Integrated Circuits and Systems*, 35(11):1811–1824, 2016.

[13] S.M. Alam, C.L. Gan, F.L. Wei, C.V. Thompson, and D.E. Troxel. Circuit-level reliability requirements for cu metallization. *IEEE Transactions on Device and Materials Reliability*, 5(3):522–531, 2005.

[14] J.J. Clement, S.P. Riege, R. Cvijetic, and C.V. Thompson. Methodology for electromigration critical threshold design rule evaluation. *IEEE Transactions on Computer-Aided Design of Integrated Circuits and Systems*, 18(5):576–581, 1999.

[15] Mohammad Abdullah Al Shohel, Vidya A. Chhabria, and Sachin S. Sapatnekar. A new, computationally efficient "blech criterion" for immortality in general interconnects. In *2021 58th ACM/IEEE Design Automation Conference (DAC)*, pages 913–918, 2021.

[16] L. Zhang et al. Cap layer and grain size effects on electromigration reliability in cu/low-k interconnects. In *Procs. of the IEEE International Interconnect Technology Conference (IITC)*, pages 1–3, 2010.

[17] Wen-Hsiang Chang, Mango C.-T Chao, and Shi-Hao Chen. Practical routability-driven design flow for multilayer power networks using aluminum-pad layer. *IEEE Transactions on Very Large Scale Integration (VLSI) Systems*, 22(5):1069–1081, 2014.

[18] Sandeep Chatterjee, Valeriy Sukharev, and Farid Najm. Fast physics-based electromigration checking for on-die power grids. In *Procs. of the IEEE International Conference on Computer-Aided Design*, pages 1–8, 2016.

[19] Valeriy Sukharev, Armen Kteyan, and Xin Huang. Postvoiding stress evolution in confined metal lines. *IEEE Transactions on Device and Materials Reliability*, 16(1):50–60, 2016.

[20] Chase Cook, Zeyu Sun, Ertugrul Demircan, Mehul D. Shroff, and Sheldon X.-D. Tan. Fast electromigration stress evolution analysis for interconnect trees using krylov subspace method. *IEEE Transactions on Very Large Scale Integration (VLSI) Systems*, 26(5):969–980, 2018.

[21] Olympia Axelou, George Floros, Nestor Evmorfopoulos, and George Stamoulis. Accelerating electromigration stress analysis using low-rank balanced truncation. In *Proceedings of the 18th International Conference on Synthesis, Modeling, Analysis and Simulation Methods and Applications to Circuit Design (SMACD)*, pages 1–4, 2022.

[22] COMSOL Multiphysics®.

[23] Hai-Bao Chen, Sheldon X.-D. Tan, Jiangtao Peng, Taeyoung Kim, and Jie Chen. Analytical modeling of electromigration failure for vlsi interconnect tree considering temperature and segment length effects. *IEEE Transactions on Device and Materials Reliability*, 17(4):653–666, 2017.

[24] Olympia Axelou, Nestor Evmorfopoulos, George Floros, George Stamoulis, and Sachin S. Sapatnekar. A novel semi-analytical approach for fast electromigration stress analysis in multi-segment interconnects. In *Proceedings of the 41st IEEE/ACM International Conference on Computer-Aided Design*, 2022.

[25] Liang Chen, Sheldon X.-D. Tan, Zeyu Sun, Shaoyi Peng, Min Tang, and Junfa Mao. A fast semi-analytic approach for combined electromigration and thermomigration analysis for general multisegment interconnects. *IEEE Transactions on Computer-Aided Design of Integrated Circuits and Systems*, 40(2):350–363, 2021.

[26] Wentian Jin, Liang Chen, Sheriff Sadiqbatcha, Shaoyi Peng, and Sheldon X.-D. Tan. Emgraph: Fast learning-based electromigration analysis for multi-segment interconnect

using graph convolution networks. In *2021 58th ACM/IEEE Design Automation Conference (DAC)*, pages 919–924, 2021.

[27] Yunfan Zuo, Yuyang Ye, Hongchao Zhang, Tinghuan Chen, Hao Yan, and Longxing Shi. A graph-learning-driven prediction method for combined electromigration and thermomigration stress on multi-segment interconnects. In *2024 Design, Automation & Test in Europe Conference & Exhibition (DATE)*, pages 1–6, 2024.

[28] Wentian Jin, Liang Chen, Subed Lamichhane, Mohammadamir Kavousi, and Sheldon X.-D. Tan. Hierpinn-em: Fast learning-based electromigration analysis for multi-segment interconnects using hierarchical physics-informed neural network. In *2022 IEEE/ACM International Conference On Computer Aided Design (ICCAD)*, pages 1–9, 2022.

[29] Hengyang Zhao and Sheldon Tan. Multi-physics-based fem analysis for post-voiding analysis of electromigration failure effects. In *2018 IEEE/ACM International Conference on Computer-Aided Design (ICCAD)*, pages 1–8, 2018.

[30] Subed Lamichhane, Wentian Jin, Liang Chen, Mohammadamir Kavousi, and Sheldon X.-D. Tan. Postpinn-em: Fast post-voiding electromigration analysis using two-stage physics-informed neural networks. In *2023 IEEE/ACM International Conference on Computer Aided Design (ICCAD)*, pages 1–9, 2023.

[31] Farid N. Najm. Equivalent circuits for electromigration. *Microelectronics Reliability*, 123:114200, 2021.

[32] Leon O Chua and P. Lin. *Computer-Aided Analysis of Electronic Circuits: Algorithms and Computational Techniques*. Prentice Hall Professional Technical Reference, 1975.

[33] Chrysostomos Chatzigeorgiou, Dimitrios Garyfallou, George Floros, Nestor Evmorfopoulos, and George Stamoulis. Exploiting Extended Krylov Subspace for the Reduction of Regular and Singular Circuit Models. In *Proceedings of the 26th Asia South Pacific Design Automation Conference (ASP-DAC)*, pages 773–778, 2021.

[34] Vladimir Druskin and Valeria Simoncini. Adaptive rational krylov subspaces for large-scale dynamical systems. *Systems & Control Letters*, 60:546–560, 2011.

[35] S.M. Alam, C.L. Gan, F.L. Wei, C.V. Thompson, and D.E. Troxel. Circuit-level reliability requirements for cu metallization. *IEEE Transactions on Device and Materials Reliability*, 5(3):522–531, 2005.

[36] Vidya A. Chhabria, Andrew B. Kahng, Minsoo Kim, Uday Mallappa, Sachin S. Sapatnekar, and Bangqi Xu. Template-based pdn synthesis in floorplan and placement using classifier and cnn techniques. In *2020 25th Asia and South Pacific Design Automation Conference (ASP-DAC)*, pages 44–49, 2020.

[37] PDNSim. `https://github.com/The-OpenROAD-Project/OpenROAD/tree/master/src/PDNSim`.

[38] J. Phillips, L. Daniel, and L. Miguel Silveira. Guaranteed passive balancing transformations for model order reduction. In *Design Automation Conference*, pages 52–57, 2002.

[39] A. Odabasioglu, M. Celik, and L.T. Pileggi. Prima: passive reduced-order interconnect macromodeling algorithm. *IEEE Transactions on Computer-Aided Design of Integrated Circuits and Systems*, 17(8):645–654, 1998.

[40] S. Mei and Y. I. Ismail. Stable parallelizable model order reduction for circuits with frequency-dependent elements. *IEEE Transactions on Circuits and Systems I: Regular Papers*, 56(6):1214–1220, 2009.

[41] W. Zhao et al. Automatic adaptive multi-point moment matching for descriptor system model order reduction. In *International Symposium on VLSI Design, Automation, and Test*, pages 1–4, 2013.

[42] N. Banagaaya, G. Alì, W. H. A. Schilders, and C. Tischendorf. Implicit index-aware model order reduction for rlc/rc networks. In *Design, Automation & Test in Europe Conference & Exhibition*, pages 1–6, 2014.

[43] K. Gröchenig. Foundations of time-frequency analysis. In *Applied and Numerical Harmonic Analysis*, 2001.

[44] L. Knizhnerman and V. Simoncini. A new investigation of the extended krylov subspace method for matrix function evaluations. *Numerical Linear Algebra with Applications*, 17(4):615–638, 2010.

[45] V. Simoncini. A new iterative method for solving large-scale lyapunov matrix equations. *SIAM Journal on Scientific Computing*, 29(3):1268–1288, 2007.

[46] G. Floros et al. Frequency-limited reduction of regular and singular circuit models via extended krylov subspace method. *IEEE Transactions on Very Large Scale Integration (VLSI) Systems*, 28(7):1610–1620, 2020.

[47] J. M. Wang and T. V. Nguyen. Extended krylov subspace method for reduced order analysis of linear circuits with multiple sources. In *Design Automation Conference*, page 247–252, 2000.

[48] C. Chatzigeorgiou et al. Exploiting extended krylov subspace for the reduction of regular and singular circuit models. In *Asia and South Pacific Design Automation Conference*, pages 773–778, 2021.

[49] T. A. Davis and E. P. Natarajan. Algorithm 907: Klu, a direct sparse solver for circuit simulation problems. *ACM Trans. Math. Softw.*, 37(3), 2010.

[50] D .and others Garyfallou. A combinatorial multigrid preconditioned iterative method for large scale circuit simulation on gpu s. In *International Conference on Synthesis, Modeling, Analysis, and Simulation Methods and Applications to Circuit Design*, pages 209–212, 2018.

[51] G. Golub and C. F. Van Loan. Matrix computations. In *Johns Hopkins University Press*, 1996.

[52] S. R. Nassif. Power grid analysis benchmarks. In *Asia and South Pacific Design Automation Conference*, pages 376–381, 2008.

[53] Paolo Nenzi and Holger Vogt. *Ngspice User's Manual Version 23*, 2011. Available at `https://ngspice.sourceforge.io/docs/ngspice-manual.pdf`.

[54] Mohammad Tehranipoor, Hassan Salmani, Xuehui Zhang, Michel Wang, Ramesh Karri, Jeyavijayan Rajendran, and Kurt Rosenfeld. Trustworthy hardware: Trojan detection and design-for-trust challenges. *Computer*, 44(7):66–74, 2011.

[55] Chase Cook, Sheriff Sadiqbatcha, Zeyu Sun, and Sheldon X.-D. Tan. Reliability based hardware trojan design using physics-based electromigration models. *Integration*, 66:9–15, 2019.

[56] Jens Lienig, Susann Rothe, Matthias Thiele, Nikhil Rangarajan, Mohammed Ashraf, Mohammed Nabeel, Hussam Amrouch, Ozgur Sinanoglu, and Johann Knechtel. Toward security closure in the face of reliability effects iccad special session paper. In *2021 IEEE/ACM International Conference On Computer Aided Design (ICCAD)*, pages 1–9, Nov 2021.

[57] Alexandra Takou, Pavlos Stoikos, Moysis Moysis, George Floros, Nestor Evmorfopoulos, and George Stamoulis. An efficient security closure methodology for em-based attacks on power grid structures. In *2023 IEEE International Symposium on Defect and Fault Tolerance in VLSI and Nanotechnology Systems (DFT)*, pages 1–4, 2023.

[58] Alexandra Takou, Olympia Axelou, George Floros, Nestor Evmorfopoulos, and George Stamoulis. An optimal methodology for em-based hardware trojan placement on clock tree networks. In *2023 IEEE 66th International Midwest Symposium on Circuits and Systems (MWSCAS)*, pages 25–29, 2023.

[59] J.N. Kozhaya, S.R. Nassif, and F.N. Najm. A multigrid-like technique for power grid analysis. *IEEE Transactions on Computer-Aided Design of Integrated Circuits and Systems*, 21(10):1148–1160, 2002.

[60] Olympia Axelou, Nestor Evmorfopoulos, George Floros, George Stamoulis, and Sachin S. Sapatnekar. A novel semi-analytical approach for fast electromigration stress analysis in multi-segment interconnects. In *2022 IEEE/ACM International Conference On Computer Aided Design (ICCAD)*, pages 1–7, 2022.

[61] Pavlos Stoikos, George Floros, Dimitrios Garyfallou, Nestor Evmorfopoulos, and George Stamoulis. A fast semi-analytical approach for transient electromigration analysis of interconnect trees using matrix exponential. In *Proceedings of the 28th Asia and South Pacific Design Automation Conference*, ASPDAC '23, page 1–6, 2023.

[62] Haifeng Qian and Sachin S. Sapatnekar. Fast poisson solvers for thermal analysis. In *2010 IEEE/ACM International Conference on Computer-Aided Design (ICCAD)*, pages 698–702, 2010.

APPENDICES

Appendix A

Matrix exponential solution

In this appendix, we derive a closed-form solution for stress evolution in a linear system using the matrix exponential operator. Assuming a piecewise linear input over each time interval, we obtain an explicit expression for the stress over a single time step.

The discrete-time update of the state vector σ using the matrix exponential is given by:

$$\sigma(t+h) = e^{h\mathbf{A}}\sigma(t) + \int_0^h e^{(h-\tau)\mathbf{A}}\mathbf{b}(t+\tau)\,d\tau \tag{A.1}$$

where

$$\mathbf{A} = \mathbf{C}^{-1}\mathbf{G}, \quad \mathbf{b}(t) = \mathbf{C}^{-1}\mathbf{B}\mathbf{j}(t)$$

Assuming the input $\mathbf{j}(t)$ is piecewise linear (PWL) over $[t, t+\tau]$ and $\tau \in [0, h]$, we approximate $\mathbf{b}(t+h)$:

$$\begin{aligned} \frac{\mathbf{b}(t+\tau)-\mathbf{b}(t)}{h} &= \frac{\mathbf{b}(t+h)-\mathbf{b}(t)}{h} \Rightarrow \\ \mathbf{b}(t+\tau) &= \frac{\mathbf{b}(t+h)-\mathbf{b}(t)}{h}\tau + \mathbf{b}(t) \Rightarrow \\ \mathbf{b}(t+\tau) &= \alpha\,\tau + \beta \end{aligned} \tag{A.2}$$

Substituting Eq. (A.2) into Eq. (A.1), the integral term becomes:

$$\begin{aligned} &\int_0^h e^{(h-\tau)\mathbf{A}}(\alpha\,\tau+\beta)\,d\tau \\ &= \alpha\int_0^h e^{(h-\tau)\mathbf{A}}\tau\,d\tau + \beta\int_0^h e^{(h-\tau)\mathbf{A}}\,d\tau \end{aligned} \tag{A.3}$$

The first term of Eq. (A.3) can be integrated as follows:

$$\begin{aligned} \alpha\int_0^h e^{(h-\tau)\mathbf{A}}\tau\,d\tau &= \alpha\Big[-\mathbf{A}^{-1}e^{(h-\tau)\mathbf{A}}\tau - \mathbf{A}^{-2}e^{(h-\tau)\mathbf{A}}\Big]_0^h \\ &= \alpha(-\mathbf{A}^{-1}h - \mathbf{A}^{-2} + \mathbf{A}^{-2}e^{h\mathbf{A}}) = \alpha\mathbf{A}^{-2}(e^{h\mathbf{A}} - \mathbf{A}h - \mathbf{I}) \end{aligned} \tag{A.4}$$

The second term of Eq. (A.3) can be integrated as:

$$\begin{aligned} \beta \int_0^h e^{(h-\tau)\mathbf{A}}\, d\tau = \beta \Big[-\mathbf{A}^{-1} e^{(h-\tau)\mathbf{A}} \Big]_0^h \\ = \beta(-\mathbf{A}^{-1} - (-\mathbf{A}^{-1} e^{h\mathbf{A}}) = \beta \mathbf{A}^{-1}(e^{h\mathbf{A}} - \mathbf{I}) \end{aligned} \tag{A.5}$$

Combining the results of Eq. (A.2), (A.4), and (A.5), Eq. (A.1) becomes:

$$\begin{aligned} \sigma(t+h) = e^{h\mathbf{A}}\sigma(t) + \alpha\mathbf{A}^{-2}(e^{h\mathbf{A}} - \mathbf{A}h - \mathbf{I}) + \beta\mathbf{A}^{-1}(e^{h\mathbf{A}} - \mathbf{I}) \Rightarrow \\ \sigma(t+h) = e^{h\mathbf{A}}(\sigma(t) + \alpha\mathbf{A}^{-2} + \beta\mathbf{A}^{-1}) - (\alpha\mathbf{A}^{-1}h + \alpha\mathbf{A}^{-2} + \beta\mathbf{A}^{-1}) \end{aligned} \tag{A.6}$$

Substituting back the expressions for α and β, we obtain:

$$\begin{aligned} \sigma(t+h) = e^{h\mathbf{A}} \left(\sigma(t) + \mathbf{A}^{-1}\mathbf{b}(t) + \mathbf{A}^{-2}\frac{\mathbf{b}(t+h) - \mathbf{b}(t)}{h} \right) \\ - \left(\mathbf{A}^{-1}\mathbf{b}(t+h) + \mathbf{A}^{-2}\frac{\mathbf{b}(t+h) - \mathbf{b}(t)}{h} \right) \end{aligned} \tag{A.7}$$

For a constant input $\mathbf{j}(t)$, where $\mathbf{b}(t+h) = \mathbf{b}(t)$, and evaluating at $t = 0$, the expression simplifies to:

$$\sigma(h) = e^{h\mathbf{A}} \big(\sigma(0) + \mathbf{A}^{-1}\mathbf{b}(h)\big) - \mathbf{A}^{-1}\mathbf{b}(h) \tag{A.8}$$

Finally, replacing h with t, the solution takes the form:

$$\begin{aligned} \sigma(t) = e^{t\mathbf{A}} \big(\sigma(0) + \mathbf{F}(t)\big) - \mathbf{F}(t), \\ \mathbf{F}(t) = \mathbf{A}^{-1}\mathbf{b}(t) \end{aligned} \tag{A.9}$$